HYDROGEN AND RELATED DEFECTS IN OXIDE SEMICONDUCTORS

By

MARIANNE CUREG TARUN

A dissertation submitted in partial fulfillment of
the requirements for the degree of

DOCTOR OF PHILOSOPHY

WASHINGTON STATE UNIVERSITY
Materials Science and Engineering Program

MAY 2012

To the Faculty of Washington State University:

The members of the Committee appointed to examine the dissertation of MARIANNE CUREG TARUN find it satisfactory and recommend that it be accepted.

Matthew D. McCluskey, Ph.D., Chair

Kelvin G. Lynn, Ph.D.

Ursula M. Mazur, Ph.D.

ACKNOWLEDGEMENTS

First and foremost, I thank my advisor, Prof. Matthew McCluskey, for all the ways that he has supported me and guided me with my research. His no-nonsense approach, direction and admirable editing skills have remarkably shaped my research experience. My gratitude also extends to Prof. Kerry Hipps for bestowing confidence upon me when I applied as a prospective doctoral student for the Materials Science Program.

My thanks to Prof. Ursula Mazur whose presence during my seminar talks has always encouraged me and helped me believe in myself. I also thank Prof. Kelvin Lynn for his kindness to collaborate in some areas of my research. Their presence on my committee is truly a pleasure and an honor.

I also thank our current chair of the Materials Science and Engineering Program (MSEP) Prof. Indranath Dutta and our current as well as former academic coordinators Cyndi Whitmore and Lori Bruce, respectively, for their kind support. And my warm thanks are also due to the Department of Physics and Astronomy for being my wonderful “home” department.

I thank Dr. Marc Weber, Dr. Farida Selim, Dr. Leah Bergman (UI) and Dr. Evan Glaser (NRL) for valuable collaborations and discussions.

I am indebted to the two wonderful former graduate students of Prof. McCluskey: Dr. Slade Jokela, for passing the baton of knowledge in crystal growth and whose prior work has laid the foundation for my research in ZnO; and Dr. Win Maw Oo for his helpful assistance in introducing me to the various instruments in the lab.

I thank my fellow graduate students Sam Teklemichael, Narendra Parmar, and Enam Khan with whom a scientific discourse on ZnO has always been a delight. Special thanks to my best friend, Shiva Ramini, who has always been there to help and encourage me in so many wonderful ways. I have not known a more caring, smart and funny friend to discuss science and research with. I cherish his kindness and friendship.

I thank my Filipino friends in Pullman who served as my family away from home. Special thanks to John and Janet Matanguihan and kids for their love and prayers.

My heartfelt thanks to my relatives in Seattle: Auntie Del, Christine, Dexter, Sherlee and Gabbi. Their nearness is my good; they have been my constant refuge!

My deepest gratitude to my parents, my brothers Carleo and TJ, and my sisters Maricar and Maripol, whose constant support, prayers and unconditional love have anchored me and sustained me to a strong finish.

And to my God, whose *grace* is more than sufficient to cover my insufficiency, to Him I give the highest glory and praise!

DEFECTS IN OXIDE SEMICONDUCTORS

ABSTRACT

By Marianne C. Tarun, Ph.D.,
Washington State University
May 2012

Chair: Matthew D. McCluskey

Oxide semiconductors are an interesting class of materials which occur in a variety of crystal structures and exhibit diverse electronic and optical properties. This thesis is primarily focused on investigating defects in **zinc oxide (ZnO)** and **strontium titanate ($SrTiO_3$)**, two important wide-bandgap oxide semiconductors.

While zinc oxide is a promising material for blue and UV solid-state lighting devices, the lack of *p*-type doping has precluded ZnO from becoming a dominant material for optoelectronic applications. Over the past decade, numerous reports have claimed that nitrogen is a feasible *p*-type dopant in ZnO. In this work, nitrogen-doped bulk, single crystal ZnO grown by chemical vapor transport is investigated. Photoluminescence (PL) measurements show broad red luminescence band at ~1.7 eV, with an excitation threshold of ~2.2 eV. This result is in agreement with the calculated configuration-coordinate diagram for nitrogen *deep* acceptor [Appl. Phys. Lett. **95**, 252105 (2009)] that shows an acceptor level of 1.3 eV above the valence band maximum. Comparing the PL spectra for the undoped and N-doped samples confirms the

red PL band is correlated with nitrogen acceptors. The intensity of this band increases with the concentration of activated nitrogen acceptors. The deep-acceptor behavior of nitrogen can be explained by the low position of the ZnO valence band maximum relative to vacuum.

Hydrogen is a ubiquitous impurity in oxide semiconductors and a potential source of *n*-type conductivity. Despite its prevalence, little is known about its behavior in oxides such as $SrTiO_3$. Infrared (IR) absorption spectroscopy shows a hydrogen-related defect in $SrTiO_3$ with local vibrational modes (LVMs) at 3355 and 3384 cm^{-1} at liquid-helium temperatures. Isotope substitution experiments reveal that the defect consists of two hydrogen atoms bound to host oxygen atoms. From the temperature dependence of the LVMs, the complex is ascribed to a strontium vacancy passivated by two hydrogen atoms. The thermal stability of the defect is determined through a series of isochronal annealing experiments on the hydrogenated $SrTiO_3$ sample. These measurements provide evidence of “hidden hydrogen,” possibly H_2 molecules, in the crystal. Remarkably, in ZnO, a much less ionic crystal, hydrogen also passivates zinc vacancies [Phys. Rev. B **66**, 165205 (2002)] and form H_2 molecules [Appl. Phys. Lett. **85**, 5601 (2004)]. It is therefore suggested that a “universal behavior” of hydrogen exists across a diverse range of oxides.

TABLE OF CONTENTS

LIST OF FIGURES

LIST OF TABLES

To my loving parents, Leopoldo and Carmen.

CHAPTER 1 INTRODUCTION

Semiconductors are at the heart of almost every modern electronic device, from television and computers to smartphones. For example, while I was searching for a particular smartphone recently, I examined the different types and quality of the display. My attention was drawn to a particular model that employs a display technology that features low power consumption, notwithstanding the superior display quality: the AMOLED or active-matrix organic light-emitting diode (Ashtiani and Nathan, 2009). AMOLED is a type of OLED that utilizes silicon-based thin-film transistor (TFT) technology for its backplane driving electronics. The display industry is now exploring to replace the conventional Si with *oxide* semiconductors, such as indium gallium zinc oxide (IGZO), which are reported to have the advantages that would enable large size, high quality, and low-cost AMOLED displays (Jeong, 2011). This is just one example that illustrates the emerging role of oxides as semiconductor materials in the current trend in developing more efficient devices and cheaper alternatives to existing technologies.

Oxides are adding new capabilities to electronic devices due to their unique functional properties. They are potential semiconductor materials for use in more efficient and less expensive solid state lighting devices (Look et al., 2004). Just as transistors (Bardeen and Brattain, 1948; Shockley and Pearson, 1948) replaced vacuum tubes over a half century ago and flat panel displays are replacing cathode ray tubes today, solid-state lighting is primed to take the place of incandescent and fluorescent lamps for general illumination systems. With oxides, we may have a *brighter* future in solid-state lighting.

My research is primarily focused on investigating defects in ***zinc oxide*** **(*ZnO*)** and ***strontium titanate*** **($SrTiO_3$)**, two technologically important oxide semiconductors. It is essential to understand and control defects as they affect the electrical and optical properties of semiconductors.

This thesis is organized as follows. Chapter 1 consists of sections that deal with the fundamentals of semiconductors, the features of oxides as semiconductors and the properties of ZnO and $SrTiO_3$. In Chapter 2, theoretical background is presented pertaining to vibrational modes of impurities in semiconductors. Chapter 3 discusses the experimental techniques that were applied to obtain the results discussed in this work. In Chapter 4, I discuss the results of my experimental investigation of nitrogen-doped ZnO. Chapter 5 presents the results of my work on hydrogen-related defects in $SrTiO_3$. In Chapter 6, I reexamine my initial work on hydrogen defects in ZnO. In Chapter 7, I summarize the main results and conclusions of my research. A short chapter (Chapter 8) with future work recommendations concludes this thesis.

1.1 Semiconductor basics

A semiconductor crystal is composed of atoms which are arranged in a highly ordered structure called a *lattice*, with covalent bonds between neighboring atoms. Electrons are confined to a number of possible energy states arranged in *bands*, and are forbidden in other regions. In an intrinsic semiconductor at absolute zero temperature, the band structure consists of completely filled bands and completely empty bands. The filled bands are those that are occupied by the ground state electrons, and the highest range of electron energies is called the *valence band*. Of the unoccupied bands, the lowest energy band is the *conduction band*. The difference in energy between the conduction band edge and the valance band edge is the forbidden energy gap called the *band gap* (Fig. 1.1). In order for an electron to jump from the valence band to the conduction band, it requires specific minimum amount of energy for the transition. Once the electron is in the conduction band, it can move freely and carry current. The "missing electron" in the valence band leaves a "hole" which carries a positive charge and can be filled by a valence electron from a neighboring atom. Thus, the hole drifts between atoms behaving as a positive charge carrier, analogous to an electron in the conduction band behaving as a negative charge carrier. An electron has an increasing probability of occupying the conduction band at higher temperatures.

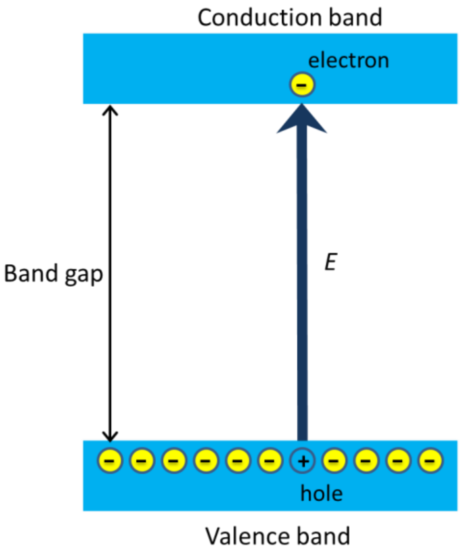

Figure 1.1 Schematic diagram of the band structure showing an electron excited across the band gap into the conduction band.

The band gap of an intrinsic semiconductor may be determined from the temperature dependence of the carrier concentration. The band gap energy is obtained from an Arrhenius plot of the logarithm of the carrier concentration versus inverse of temperature. Another method of measuring band gap is by optical absorption, in which a photon excites an electron into the conduction band. For a semiconductor with a "direct" band gap, the threshold of the optical absorption at frequency ω_g measures the band gap $E_g = \hbar\omega_g$ (Fig. 1.2a). A photon is absorbed with the creation of an electron and a hole. The momentum of electrons and holes is the same in both the conduction band and valence band; hence a direct optical transition is drawn vertically with no significant change of wavevector **k** (Fig. 1.3a). In an “indirect”-band gap semiconductor, the optical absorption is weaker near the threshold (Fig. 1.2b). Because the conduction-band minimum and the valence-band maximum are widely separated in **k** space (Fig. 1.3b), indirect transition involves both a photon and a *phonon* to conserve momentum. A phonon is one quantum of a lattice vibration. The phonon energy $\hbar\Omega$ is characteristically much smaller than the band gap (~10 to 30 meV). Thus, phonons produce approximately horizontal transitions (Fig. 1.3b). The absorption threshold for the indirect transition between the band edges is at $\hbar\omega = E_g + \hbar\Omega$, where Ω is the frequency of an emitted phonon, corresponding to creation of a phonon. At higher temperatures, where the necessary phonon is already thermally excited in the crystal, the phonon can be absorbed along with the photon. The threshold energy is $\hbar\omega = E_g - \hbar\Omega$, corresponding to destruction of a phonon.

Whether a material is a direct-gap or indirect gap material is of great importance in the development of optical semiconductor devices that work on the basis of radiative recombination. In an indirect semiconductor, the recombination of an electron and a hole requires the assistance of a phonon to satisfy momentum conservation. This is a three-particle interaction between an electron, a photon, and a phonon, which is much less likely than a two-particle interaction. Thus, indirect-gap semiconductors like silicon and germanium have low emission efficiencies and are not favorable materials for optoelectronic applications. Direct-gap semiconductors like GaN are preferred materials for fabrication of light emitting sources. The direct band gap is most favorable for radiative recombination because no phonons are required to conserve momentum.

\

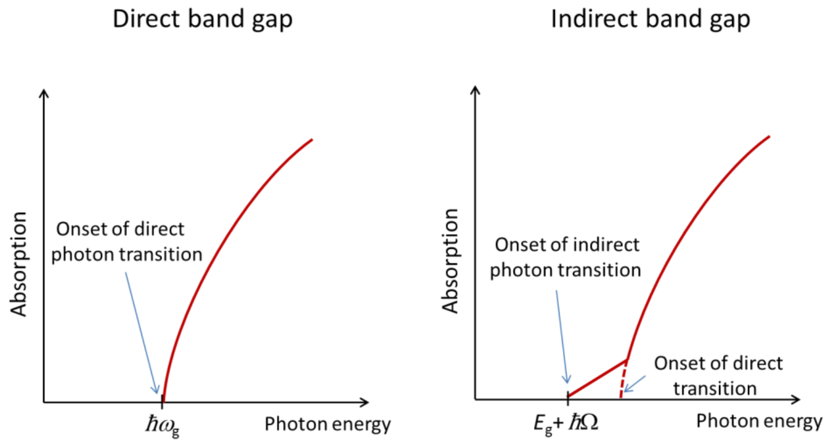

(a) (b)

Figure 1.2: Optical absorption in pure semiconductors at absolute zero.

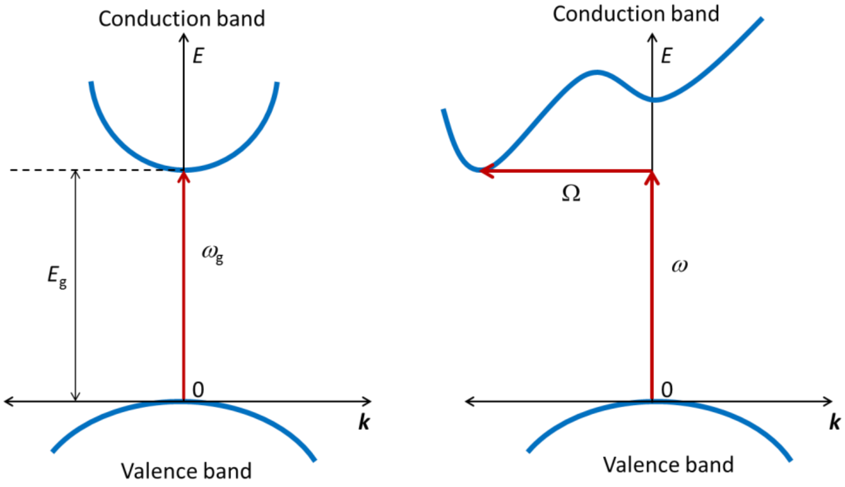

(a) (b)

Figure 1.3: (a) In a direct gap, the conduction-band minimum occurs at the same value of k as the valence-band maximum (k = 0). (b) In an indirect gap, the conduction-band minimum occurs at nonzero k value. A phonon is needed to conserve momentum since photons carry essentially no momentum.

When an impurity is added to a semiconductor, whether unintentionally or by design, energy levels are usually introduced within the band gap. An impurity or dopant atom can act as a shallow *donor* if the extra energy level is near the conduction band to where the donor electrons can be easily excited. It is a shallow *acceptor* if the energy level is close to the valence band where electrons can be easily excited to the acceptor level, leaving mobile holes in the valence band. A donor level is said to be neutral when it is occupied with an electron and positive when the electron is liberated. An acceptor level is negative when occupied with an electron and neutral when it is unoccupied.

In an intrinsic semiconductor, the number of excited electrons and the number of holes are equal. In doped or extrinsic semiconductors, however, there is an excess of free electrons or holes. *N*-type (*p*-type) semiconductors are those with electrons (holes) as majority charge carriers and are obtained by doping with donor (acceptor) impurities. Consider silicon as a specific example. *N*-type silicon can be obtained by doping with pentavalent impurities, typically phosphorus, which has one more valence electron than the silicon atom that it substitutes. This extra electron is bound to the positively charged phosphorus ion, forming a system that behaves like a hydrogen atom, with a binding energy of 45 meV (Kittel, 2005). With this shallow binding energy almost all the electrons are ionized into the conduction band at room temperature. *P*-type doping in silicon can be produced by trivalent impurities like boron, aluminum or gallium, which have one less valence electron than silicon. An electron is taken from the valence band, creating a hole. Considering the case of the boron acceptor in silicon, the hole is bound to the negatively charged boron ion with a binding energy of 45 meV (Kittel, 2005) and thus can be excited into the valence band.

The binding energy can be approximated using the Bohr model of the atom. In the case of the donor impurity atom, we may visualize a hydrogenic system consisting of the donor electron bound to the positively charged donor ion by Coulomb attraction. Taking into account the relative dielectric constant ε of the semiconductor material and the effective mass $m*$ of an electron in the periodic potential of the crystal, the binding energy for the electron is

$$E = \frac{13.6\ \mathrm{eV}}{\varepsilon^2}\frac{m^*}{m_e}, \tag{1.1}$$

where m_e is the mass of a free electron. Similarly, the Bohr radius is given by

$$a_0 = 0.5\ \text{Å}\ \frac{\varepsilon m_e}{m^*}. \tag{1.2}$$

The introduction of defect impurities into the crystal also affects the vibrational properties of the lattice (Barker and Sievers, 1975). Considering the regular lattice of atoms tied together in bonds, their vibrations take the form of collective modes which propagate through the crystal. As with quantum harmonic oscillators, such propagating lattice vibrations can accept energies only in discrete amounts, and these quanta of energies are referred to as *phonons*. Phonons in a perfect lattice have a well-defined wavevector ***K***. The relationship between the frequencies ω (or energies) of the phonons and their wavevector ***K*** can be solved by a quantum-mechanical approach and semiclassical treatment of lattice vibrations (Chapter 2). When an impurity atom is added in the crystal, the translational symmetry of the lattice is broken. Moreover one or more new vibrational modes, localized in both real space and frequency space, are created. These are referred to as *local vibrational modes* (LVMs). When a light atom like hydrogen is introduced in the crystal and bonds with one of the host atoms, LVMs arise with frequencies higher than the maximum phonon frequency and with narrow infrared (IR) absorption peaks.

The energy states produced by impurities or lattice defects in the crystal are also usually manifested in the luminescent properties of the semiconductor. When incident light is directed onto the surface of the material, it is partially reflected, absorbed, and transmitted by the material. The absorbed photons create electron-hole pairs as electrons are excited to the conduction band, or to the energy states within the gap. When the electron-hole pairs recombine, photons are emitted. The resulting photon emission gives the photoluminescence (PL) spectrum of the material and as a result provides information concerning the point defects in the material.

1.2 Oxide semiconductors

Oxide semiconductors are an interesting class of materials which occur in a variety of crystal structures and exhibit diverse electronic and optical properties. They also exhibit many of the advantages of conventional semiconductors and hold even greater potential for new and innovative uses. Oxide insulators already play a vital role in semiconductor electronics, and future applications may exploit their wide-ranging functionality and the richness of their intrinsic properties. Oxides are generally low cost and typically quite stable. The availability of bulk single-crystal substrates gives oxides an edge over nitride semiconductors. The crystal structures of the key structural families of complex oxides (Ramesh and Schlom, 2008) are shown in Figure 1.4.

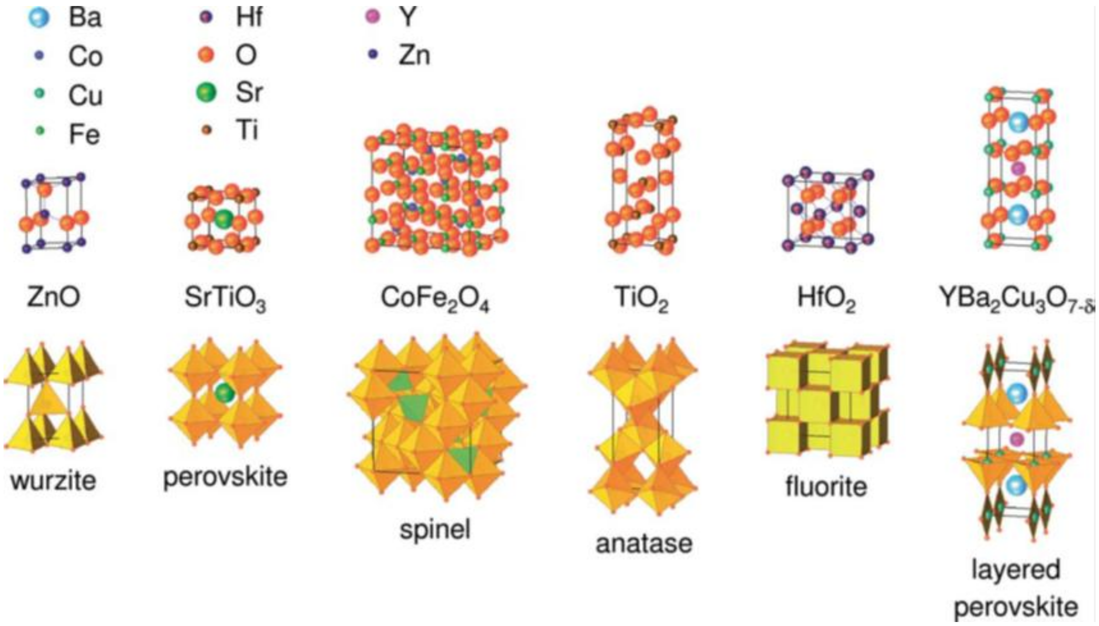

Figure 1.4: Crystal structures of some key oxides, represented by the atomic positions (top) and corresponding coordination polyhedral (bottom). TiO_2 also occurs in rutile phase. From *Whither Oxide Electronics?* by Ramamoorthy Ramesh and Darrell G. Schlom, MRS Bulletin, Volume 33 (November 2008), pp. 1006-1014. Copyright © 2008 Materials Research Society. Reprinted with the permission of Cambridge University Press.

Metal oxides have gained significant interest in electronic applications due to their transparency in the visible to near UV and considerably low resistivity, features that generally do not co-exist in conventional materials. The chemical properties of oxides in general are more complex, since they show a tendency to form native point defects. Hence, in spite of their wide bandgap (generally above 3 eV), sub-bandgap energy levels occur due to the oxygen vacancy and cation interstitial, which form donors and may contribute to *n*-type conductivity of the oxide. This intrinsic *n*-type conduction provides an advantage for the development of transparent conducting oxide (TCO) semiconductors which are key components for transparent electrodes in devices that are designed for emitting or absorbing light, such as light-emitting diodes, active matrix liquid-crystal displays, or solar cells.

Zinc oxide (ZnO), tin oxide (SnO_2), and indium oxide (In_2O_3) are among the TCO semiconductors that have been developed for thin-film transparent electrodes (Minami, 2005). Thus far, SnO_2 is used to the largest extent and is perhaps the material of greatest economic importance. Although several oxides exhibit sensitivity towards oxidizing and reducing gases by a change in their electrical properties, SnO_2 was one of the first considered, and still the most widely used material for gas sensing applications (Batzill and Diebold, 2005). One of the major advantages of SnO_2 is its low cost both in terms of raw materials and processing. In addition, it has excellent thermal stability and high mechanical and chemical durability compared to other TCOs (Gordon, 2011). While SnO_2 is transparent in the visible range, it is highly reflective for infrared light, a property that is responsible for its extensive use today as a coating for energy-conserving glass windows (Lewis and Paine, 2000). Recent theoretical work (Singh et al., 2008) shows excellent prospects for *p*-type doping in SnO_2, suggesting a promising alternative material for light emitters and other optoelectronic devices. SnO_2 has a direct band gap of 3.6 eV (Batzill and Diebold, 2005).

While native defects play a significant role in oxide semiconductors, they may not be the predominant cause of the inherent *n*-type conductivity. First-principles calculations, based on density functional theory by Van de Walle (2001), showed that the oxygen vacancy in ZnO is a deep donor. The zinc interstitial was also found to be unlikely to occur because it has high formation energies under *n*-type condition (Thomas, 1957; Janotti and Van de Walle, 2007b). Similarly, in SnO_2, the oxygen vacancy is a deep donor and Sn interstitial is very unstable with very high formation energy (Singh et al., 2008; Janotti and Van de Walle, 2011). If native point defects are not the predominant sources of *n*-type conductivity in these oxide semiconductors, then an extrinsic source, an impurity that is unintentionally incorporated, could be a possible cause. Hydrogen has been proposed to be an excellent candidate for such an impurity (Van de Walle, 2000). It is highly plausible that hydrogen can be incorporated unintentionally during crystal or epitaxial growths. Source gases often contain hydrogen and H_2 is used as a carrier gas in some cases. In molecular beam epitaxy hydrogen is a prevailing background impurity (Eaglesham et al., 1993). Furthermore, the incorporation of hydrogen into the oxide lattice is propelled by the strong bond between hydrogen and oxygen. In TiO_2, hydrogen is also likely to contribute to *n*-type conductivity (Janotti and Van de Walle, 2011), although the oxygen vacancy has been considered to be a source of conductivity due to its variation with oxygen partial pressure (Linsebigler et al., 1995). In ZnO the study of hydrogen defects is not a new one. In the 1950s Mollwo (1954) and Thomas and Lander (1956) investigated the diffusion of hydrogen in ZnO. Both studies found that annealing ZnO crystals in a hydrogen ambient affected their electrical conductivity. Thomas and Lander concluded that hydrogen was directly responsible for producing donors in ZnO. Theoretical calculations by Van de Walle (2000) showed that hydrogen is a shallow donor in ZnO.

Hydrogen plays an important role in improving the electrical and optical properties of crystalline semiconductors (Pearton et al., 1992). Its incorporation into perovskite oxides (ABO_3) such as $SrCeO_3$ and $BaTiO_3$ can remarkably influence their properties utilized for solid state proton conduction, an important issue in fuel cells (Norby, 2009). Hydrogen defects also play a central role in $LiNbO_3$ for fabrication of optical waveguides produced by proton exchange (Cabrera et al., 1996).

Oxygen plays a considerable role on the rich spectrum of phenomena found in oxides (Heber, 2009). Because oxygen tends to pull electrons away from other atoms in the compound, strong electric fields at the interatomic scale are produced. These fields can provide significant correlations in behavior between electrons of one atom and those of its neighbors. The correlations in turn can lead to effects such as *ferromagnetism*, wherein the electron spins of a material spontaneously align and produce a magnetic field (Solymar and Walsh, 2004).

The seminal contribution of Bednorz and Müller (1986) in the area of high-temperature superconductivity spurred a world-wide focus on oxides that led to other discoveries. For instance, Jin et al. (1994) reported *colossal magnetoresistance*, an effect in which a small external magnetic field causes certain oxides to undergo an orders-of-magnitude increase in electrical resistance. Furthermore, surprising properties of oxides continue to emerge, such as when different oxides are stacked up into *heterostructures* – like a layered cake in which each layer is an ultra-thin film only a few atoms thick. As an example, when Ohmoto and Hwang (2004) were studying the interface between lanthanum aluminate ($LaAlO_3$) and $SrTiO_3$, they discovered a two-dimensional electron gas which shows an extremely high mobility, an effect that is particularly unusual because the two oxides involved are electrical insulators. This 2D electron gas has been explored for use in a new type of fast transistor (Heber, 2009). The thin-film interface is also exploited for potential applications by stacking a ferromagnetic oxide onto an insulating oxide that is not ferromagnetic. When an external magnetic field is applied, it produces electrical polarization at the interface, and simultaneously shifts the number of electrons in the ferromagnetic oxide, which changes the magnetic field. Therefore, electrical polarization and magnetism are cross-linked as they are both controlled by the same electric field - a coupling of properties that characterizes *multiferroic* materials (Ramesh and Spaldin, 2007).

Multiferroics are of great interest as magnetic field sensors and as memory devices. The perspective, status and future directions with regards multiferroics are discussed in several focused review articles (Wang et al., 2009; Nan et al., 2008; Spalding and Fiebig, 2005).

1.3 Zinc oxide

1.3.1 Background

Zinc oxide is like a “jack of all trades” because it has been used for almost everything from a food additive to a sunscreen component. Thousands of tons are produced all over the world every year to provide for a wide range of uses. As a semiconductor, ZnO belongs to the II-VI compound semiconductor family. It has a direct gap of 3.4 eV at room temperature (Chen et al., 1998) and emits light in the blue and near-UV spectral region. The long-awaited breakthrough in the field of optoelectronics may come when controlled doping of ZnO becomes possible.

ZnO naturally occurs as a mineral called *zincite*, and is yellowish to reddish in color due to trace quantities of Mn and other elements. Bulk single-crystal ZnO samples are commonly synthesized by methods such as melt growth (Nause, 1999), vapor phase growth (Matsumoto and Noda, 1990; Look, 1998), and hydrothermal growth (Ohshima et al., 2004; Maeda et al., 2005). Cermet, Inc. uses pressurized melt growth while Eagle-Picher, when they used to grow ZnO single crystals, employed seeded chemical vapor transport. Due to its large bandgap, pure ZnO is colorless and transparent.

The growth of ZnO thin films has been probed for acoustical and optical devices because of their excellent piezoelectric properties (Özgür et al., 2005). They tend to grow with strong

(0001) preferential orientation on various substrates, including glass, sapphire, and diamond. Good epitaxial layers have been grown by all of the common techniques like RF magnetron sputtering (Kim et al., 2000); molecular beam epitaxy (MBE) (Chen et al., 1998; Fons et al., 1999); pulsed laser deposition (PLD) (Vispute et al., 1998); metal-organic chemical vapor deposition (MOCVD) (Liu et al., 2000); and hydride or chloride vapor phase deposition (HVPE) (Kasuga and Ogawa, 1983; Takahashi et al., 1999).

Although research in ZnO goes back many decades, resurgent interest is fueled by the availability of high-quality bulk single crystals and the prospects in numerous applications, including:

- a material for blue/UV optoelectronics, including light emitting and laser diodes, which may provide a cheaper alternative to GaN (Look, 2001).
- transparent conducting oxide material, when doped with Al, Ga, In, etc., providing an inexpensive replacement for indium-tin-oxide (ITO) (Minami, 2005).
- a ferromagnetic material, when doped with transition metals such as Co, Mn, and Fe, for semiconductor spintronics. Curie temperatures above 425 K in Mn-doped ZnO bulk ceramics have been observed (Sharma, et al., 2003).
- a radiation-hard material for electronic devices in harsh environments.

ZnO is currently used as a transparent conductor in solar cells (Nuruddin and Abelson, 2001) and it is also an active material in varistors (Clarke, 1999). While most of the material development has been focused on GaN (bandgap ~ 3.5 eV) and ZnSe (~2.9 eV), as they are known to be bright emitting sources, substantial interest in ZnO has emerged. This is mainly because excess electrons and holes in ZnO form tightly-bound *excitons* with a relatively large binding energy of 60 meV, leading to highly efficient near-bandgap recombination at room temperature and even higher. This is compared with the exciton binding energies of 26 meV for GaN and 20 meV for ZnSe. ZnO is, therefore, the brightest emitter among them.

While ZnO holds many inherent advantages, the lack of stable and reproducible *p*-type doping presents a major roadblock to the realization of practical devices. Reports of *p*-type ZnO are controversial (Section 1.3.3). Thus, the search for appropriate *p*-type dopant continues to be an active subject of ZnO semiconductor research.

1.3.2 Crystal structure of ZnO

ZnO crystallizes preferentially in the hexagonal wurtzite structure (Fig. 1.5) with lattice parameters $a \approx 3.249$ Å and $c \approx 5.206$ Å at room temperature (Klingshirn, 2007). The ratio, $c/a = 1.602$, deviates slightly from the ideal (close-packed) wurtzite lattice value $c/a = \sqrt{8/3} = 1.633$ (Özgür, 2005).

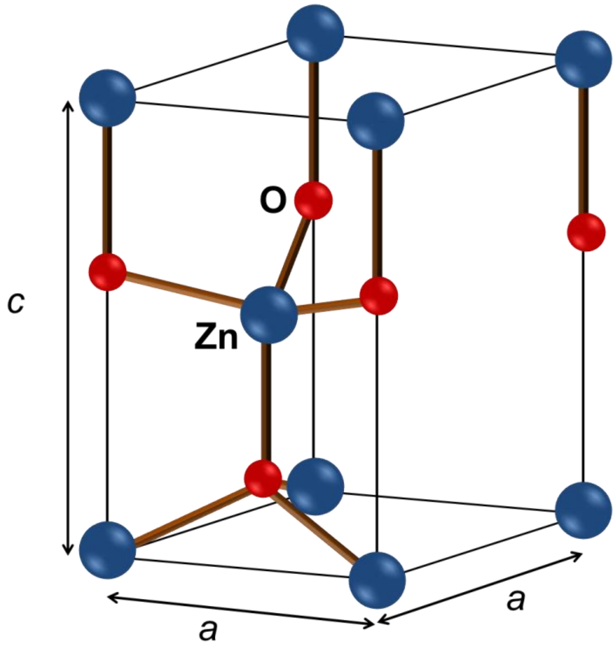

Figure 1.5: Unit cell of the wurtzite ZnO.

1.3.3 Acceptors in ZnO

Possible acceptor impurities in ZnO include group-I elements on the Zn site and group-V elements on the O site, many of which lead to deep levels and do not contribute significantly to *p*-type conduction. Reported acceptors from group-I column include Li (Schirmer, 1968; Valentin et al., 1991), Na (Zwingel and Gärtner, 1974), Cu (Kanai, 1991a), and Ag (Kanai, 1991b). First-principles calculations suggested that Li and Na form shallow acceptor levels (Park et al., 2002). However, due in part to their small size, they tend to occupy the interstitial sites rather than substitutional sites, therefore, act mainly as donors instead (Meyer et al., 2005; Lee and Chang, 2004; Wardle et al., 2005b). In order to achieve *p*-type conductivity these compensating defects would need to be eliminated. Copper is a deep acceptor with calculated acceptor level at 1.0 eV above the valence band maximum (Wardle et al., 2005a). A deep acceptor level was also identified in ZnO due to Ag doping (Chai et al., 2010).

As for the group-V elements Sb, As, and P, first principles calculations predict that they are deep acceptors due to their large ionic radii as compared to O (Park et al., 2002; Lee et al., 2006). Thus far, N seemed to be the most promising acceptor. A hole binding energy of ~200 meV based on PL experiments has been attributed to N acceptor in ZnO (Thonke et al., 2001; Meyer et al., 2004; Zeuner et al., 2002; Wang and Giles, 2004). A review of studies on N doping of ZnO is presented in the following section (1.3.4).

1.3.4 Nitrogen acceptors

Among the group-V elements, N is the acceptor in ZnO that is nearest to O in terms of size and electronic structure (Koboyashi et al., 1983). Following the reports of *p*-type ZnO by Minigeshi et al. (1997) using NH_3 in chemical vapor deposition and by Look et al. (2002) using an atomic N source in MBE, there was an upsurge of articles concerning various methods and processes to achieve *p*-type conductivity. The number of citations garnered by these experimental papers, obtained from ISI Web of Science as of January 1, 2012, is given below:

- Look et al. 2004. Characterization of homoepitaxial *p*-type ZnO grown by molecular beam epitaxy. *Appl. Phys. Lett.* 81: 1830 – 1832. ------------------------------- *782 citations*

- Minegishi et al. 1997. Growth of *p*-type zinc oxide films by chemical vapor deposition. *Jpn. J. Appl. Phys.* 36: L1453 – L1455. -- *395 citations*

Nitrogen seemed apt to lead to *p*-type conductivity in ZnO, as demonstrated by its success in *p*-type doping of another II-VI semiconductor, namely, ZnSe (Park et al., 1990; Mensz et al., 1993; Van de Walle et al., 1993). Not surprisingly, it has been the most explored acceptor dopant in ZnO. Nitrogen acceptors in ZnO were identified by electron paramagnetic resonance (EPR) studies (Carlos et al., 2001; Garces et al., 2003). By x-ray absorption spectroscopy, the N was verified to occupy the O substitutional site (Fons et al., 2006). Due to compensating donors such as group-III impurities (Garces et al., 2003), the nitrogen acceptors are negatively ionized. Furthermore, compensation may also occur through the formation of defects such as O vacancies, complexes with Zn interstitials, or N_2 molecules (Park et al., 2002; Lee et al., 2001; Limpijumnong et al., 2005). ZnO:N films grown by reactive sputtering were probed with x-ray and ultraviolet photoelectron spectroscopy (XPS and UPS), which reveal two chemical states of N, the N acceptors and the N_2 molecules on the O site [$(N_2)_O$] (Perkins et al., 2005). An XPS study on ZnO:N films prepared by MBE also reveals the main compensation source is $(N_2)_O$ donors (Li et al., 2008). First-principles calculations (Park et al., 2002; Lee et al., 2001;

Limpijumnong et al., 2005) show that $(N_2)_O$ are compensating double donors, in agreement with the experimental observations. These N_2 molecules may be removed from ZnO by thermal annealing (Yao et al., 2006). Singly-ionized N_2 acceptors (N_2^-) were observed in EPR experiments (Garces et al., 2003).

To get around the compensating donors, the introduction of acceptors requires a strategic doping method. Using NO or NO_2 gas as a possible mechanism to incorporate the necessary concentrations of N acceptors to achieve *p*-type conductivity was investigated experimentally (Yan et al., 2001) and theoretically (Matsui et al., 2004). The doping methods employed include MOCVD using NH_3 as N doping source (Wang JZ et al., 2003), plasma-assisted MBE with a NO source (Liang et al., 2005), oxidation of sputtered Zn_3N_2 thin films (Wang C et al., 2003) and N implantation of sputtered ZnO thin films (Lin et al., 2004). A high N concentration of 1 x 10^{19} cm^{-3} by gas source MBE using O_2 and N_2 was reported; however, conversion from *n*-type to *p*-type conductivity did not occur (Iwata et al., 2000). Thus far, the evidence for *p*-type conductivity in ZnO remains inconclusive, as discussed in the following section (1.3.5).

1.3.5 Issues with *p*-type conductivity

Minegishi et al. (1997) reported a hole concentration of 1.5 x 10^{16} cm^{-3} and mobility of 12 cm^2/Vs based on Hall measurements. Thonke et al. (2001) investigated the PL spectra of bulk ZnO single crystals. They observed a peak at ~3.22 eV at low temperatures and attribute this to a donor-acceptor transition with acceptor ionization energy of 195 meV. The acceptor was proposed to be nitrogen. Similarly, PL studies on epitaxial ZnO (Zeuner et al., 2002) and on bulk ZnO (Wang and Giles, 2004) have attributed a hole ionization energy of ~200 meV to a nitrogen acceptor, implying a shallow level. Hall measurements on N-doped films grown by MBE on ZnO single-crystal substrates (Look et al., 2002) were reported to produce a hole concentration of 9.6 x 10^{16} cm^{-3} and a carrier mobility of 2 cm^2/Vs. Furthermore, a PL line at 3.238 eV was assigned to a donor-acceptor transition, which resulted in estimated acceptor binding energy of 170-200 meV.

Initial theoretical studies based on tight-binding calculations (Koboyashi et al., 1983) proposed that N would act as a shallow acceptor in ZnO. Succeeding calculations based on density functional theory (DFT) within the local density approximation (LDA) (Lee et al., 2001; Park et al., 2002) or generalized gradient approximation (GGA) (Duan et al., 2010) have resulted in an acceptor level roughly 0.3 to 0.5 eV above the valence-band maximum. But we cannot completely rely on these calculations as they poorly underestimate band gaps, resulting in large uncertainties in the position of energy levels in wide-band-gap semiconductors.

While the theoretical and experimental work seemed initially promising, evidence for *p*-type ZnO remains ambiguous due to the lack of follow-up reports and actual device demonstrations. Clearly there has been a problem with reliability, stability and reproducibility. *N*-doped ZnO thin films grown by plasma-assisted CVD exhibited *p*-type conductivity but reverted to *n*-type after several days, accompanied by simultaneous relaxation of the lattice constant to its undoped value (Barnes et al., 2005). ZnO:N film deposited on glass substrate by r-f magnetron sputtering also demonstrated *p*-type instability but went back to *n*-type after repeated measurements in the dark, then transformed to *p*-type again after exposure to sunlight (Yao et al., 2006). In some experiments, the apparent *p*-type conductivity obtained may be due to interface and near-surface states (Mosbacker et al., 2005).

The difficulties of establishing conductivity type in inhomogeneous samples have also been noted (Krtschil et al., 2006), further raising doubts on published reports on hole conductivity. In performing Hall effect measurements, injudicious placement of the contact probes can give the incorrect carrier type if a sample is inhomogeneous (Bierwagen et al., 2008). As for the PL line at ~3.22 eV initially attributed to nitrogen by Thonke et al. (2001) and other groups, evidence has been provided that this line is a phonon replica of a peak that was actually related to basal-plane stacking faults (Thonke et al., 2009).

Recently, Lyons, Van de Walle, and Janotti (2009) calculated the properties of nitrogen in ZnO. They performed their calculations using DFT with hybrid functionals, which reproduce the band gap of ZnO quite accurately at 3.35 eV. Their calculations show that N_O is a deep acceptor, with the acceptor level 1.3 eV above the valence band maximum. Optical absorption and emission energies of 2.4 eV and 1.7 eV, respectively, were estimated from a configuration-coordinate diagram analysis. Stokes shift of 2.4 – 1.7 = 0.7 eV is due to large lattice relaxation of the deep acceptor. In addition, Lany and Zunger (2010) have also obtained a deep level for N_O using generalized Koopmans DFT. These recent theoretical results and the ambiguous experimental reports provided the motivation to experimentally examine nitrogen acceptors in ZnO. In Chapter 5, I will present our experimental investigation of the properties of N-doped ZnO, with the goal of providing an experimental evidence of the nature of nitrogen acceptors, and ultimately addressing the issue of the experimental difficulty in obtaining *p*-type ZnO with nitrogen.

1.4 Strontium titanate

1.4.1 Background

$SrTiO_3$ is a perovskite oxide with unique structural and dielectric properties. It has an indirect and direct bandgap of 3.25 eV and 3.7 eV, respectively (van Benthem, et al., 2010). Its natural counterpart is *tausonite*, which is an extremely rare mineral in nature. Single-crystal substrates are readily available and are typically grown by Verneuil process which involves melting the finely powdered material using an oxygen-hydrogen flame, and crystallizing the melted droplets into a boule (Jarzębski, 1973). Epitaxial $SrTiO_3$ thin films are conventionally grown by the pulsed laser deposition technique (Yu et al., 1999). Thin films with very high structural quality can be grown by MBE (Eckstein and Bozovic, 1995; Jalan, et al., 2009).

The primary interest in $SrTiO_3$, from historical point of view in terms of applications and basic research, is derived from its unique dielectric properties. The dielectric constant is strongly temperature and electric field dependent, increasing from a few hundred at room temperature to tens of thousands at low temperatures (Barrett, 1952; Müller and Burkard, 1979; Hemberger, et al., 1995).

In recent years, there has been an emergent interest in the use of $SrTiO_3$ in thin films and heterostructures. This is motivated in some measure by its potential application as a dielectric layer in data storage devices (Christen et al., 1994; Hwang et al., 1995; Gopalan et al., 1999; Morito et al., 2000) or as a component in superconductor-based microwave devices (Fuchs et al., 1999). The growing basic interest in complex oxide heterostructures (Ramesh and Schlom, 2008; Heber, 2009) has also driven this increasing interest.

Due to its commercial availability, controllable surface termination (Mukunoki et al., 1994; Koster et al., 1998; Kawasaki et al., 2005) and close lattice match to several complex oxide materials (Ramesh and Schlom, 2008; Heber, 2009), $SrTiO_3$ is widely used as a single-crystal substrate for epitaxial growth of many functional oxide thin films, including superconducting, magnetic, ferroelectric, pyroelectric, and piezoelectric oxides. It has also been used as an active component in oxide heterostructures and thin films, such as its use as an insulating barrier layer in manganite-based magnetic tunnel junctions (Bowen et al., 2005), as a dielectric layer in field-effect devices for tuning the carrier density of materials like manganites and cuprates (Ahn et al., 2003; Eblen-Zayas et al., 2005), and in systems like $SrTiO_3/LaAlO_3$ superlattices that exhibit high mobility (Ohtomo and Hwang, 2004; Siemons et al., 2007).

$SrTiO_3$ can be doped *n*-type or *p*-type. *N*-type conductivity has been most commonly obtained by doping with donor impurities like La and Nb, which substitute on the Sr and Ti sites, respectively, or by electron-doping with oxygen vacancies (Frederikse et al., 1967; Tufte and Chapman, 1967; Ohta et al., 2005). Recently epitaxial La-doped $SrTiO_3$ films grown by MBE have demonstrated excellent electron mobilities (Jalan, et al., 2009). For *p*-type doping, acceptor dopants include trivalent metals such as In, Al, and Fe substituting for Ti (Eror and Balachandran, 1982; Ferreira et al., 2000; Fagg et al, 2001; Shin et al., 2007; Fix et al., 2008). The fascinating electronic transport properties demonstrated by $SrTiO_3$ (Spinelli et al., 2010; Son, et al., 2010) may lead to potential device applications.

Hydrogen is a ubiquitous impurity and a potential source of *n*-type conductivity in $SrTiO_3$ and in most oxides (Van de Walle, 2000; Minami, 2000; Jalan et al., 2008). Despite the prevalence of hydrogen, very little is known about its interaction with native defects such as vacancies, which are known to be the dominant point defects in perovskite oxides (Mackie et al., 2009). As an impurity in the crystal being lighter than the host atoms, hydrogen can give rise to a local vibrational mode with a frequency that is higher than the vibrational frequencies of the host. The LVM can be probed by infrared (IR) absorption spectroscopy.

1.4.2 Crystal structure

$SrTiO_3$ crystallizes in the *cubic* structure at room temperature with a lattice parameter of 3.905 Å (Fig. 1.6). It undergoes a symmetry-lowering transition to *tetragonal* structure below

105 K (Weber et al., 1986) involving a rotation of the oxygen octahedron with respect to the strontium cage (Houde et al., 1987).

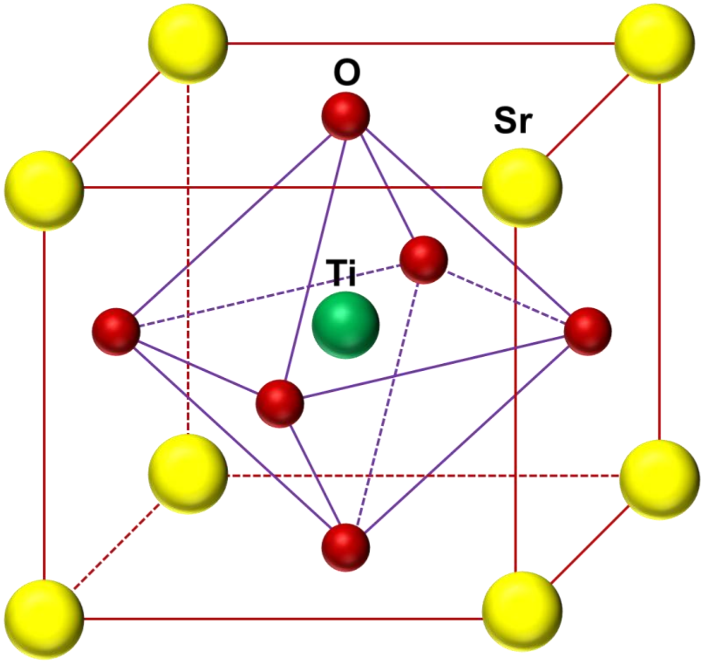

Figure 1.6: Cubic unit cell of $SrTiO_3$.

1.4.3 Hydrogen defects in strontium titanate

In most as-grown oxides, isolated hydrogen forms a bond with host oxygen, resulting in an IR absorption band in the 3200-3700 cm^{-1} region due to the O-H bond-stretching vibration (Wöhlecke and Kovács). In $SrTiO_3$ an IR absorption band near 3500 cm^{-1} was experimentally investigated (Wakim, 1968; Weber et al., 1986; Houde et al., 1987). At low temperatures (below $T_c \approx 105$ K), this O-H absorption line split into three components, reflecting the cubic to tetragonal phase transition. Two models were proposed to describe the position of the hydrogen atom in the lattice. Houde et al. (1987) assigned the position of the hydrogen atom on the faces of the cubic cell, between Sr and O atoms. Weber et al. (1986) proposed a model where the O-H vibrates along the line that connects oxygen neighbors. Similarly, based on their polarized Raman scattering study, Klauer and Wöhlecke (1992) suggested the octahedron model, i.e., H vibrates along the O – O bonds on the edges of the oxygen octahedron. A computational study based on the molecular orbital (MO) theory and a periodic supercell approach derived from the large-unit-cell model (Villamagua et al., 2007) supports the octahedron model.

In Chapter 5 I will present the results of my study of hydrogen-related defects in $SrTiO_3$, with the fundamental end of seeking a unifying, "universal trend" for the behavior of hydrogen in different oxides.

CHAPTER 2 THEORY OF VIBRATIONAL MODES

2.1 Introduction

My research is primarily focused on hydrogen in $SrTiO_3$ and nitrogen in ZnO. In both cases, hydrogen forms a bond with a native or impurity atom within the crystal lattice. In N-doped ZnO, for example, hydrogen forms N-H bonds during growth. It is therefore important to understand the effects of introducing a light impurity atom, such as hydrogen, into the crystal lattice. As it is lighter than the host atoms, hydrogen can give rise to a new vibrational mode with a frequency that is higher than the phonon modes of the host. This new mode is known as a local vibrational mode (LVM) and it interacts with IR light and the surrounding lattice, giving rise to well-defined peaks in the infrared spectrum.

2.2 The harmonic oscillator

The harmonic oscillator provides a useful model for our study of lattice vibrations in crystalline solids and the analysis of infrared spectra of diatomic molecules. In the following sections, I will discuss the classical mechanics of harmonic motion, followed by the quantum mechanical treatment of the harmonic oscillator.

2.2.1 Classical mechanics of harmonic motion

A standard classical harmonic oscillator is a mass *m* attached to a spring of force constant *k*. The system is governed by Hooke's Law:

$$F = -kx = m\frac{d^2x}{dt^2}. \tag{2.1}$$

The solution to this differential equation is

$$x(t) = A\cos(\omega t + \phi), \tag{2.2}$$

where A and ϕ are constants determined by the initial conditions ω is the frequency of oscillation given by

$$\omega \equiv \sqrt{\frac{k}{m}}\ . \tag{2.3}$$

The potential energy is

$$V(x) = \tfrac{1}{2}kx^2 \tag{2.4}$$

and its graph is a parabola. This makes a fine approximation if the displacements are small. We can see this by expanding the potential energy in a Taylor series about the local minimum x_o:

$$V(x) = V(x_0) + V'(x_0)(x - x_0) + \tfrac{1}{2}V''(x_0)(x - x_0)^2 + \ldots \tag{2.5}$$

We can drop $V(x_0)$ as it is constant and does not change the force, recognize that $V'(x_0) = 0$ since x_0 is a minimum, and ignore the higher order terms which are negligible as long as $(x - x_0)$ stays small. The potential becomes

$$V(x) \cong \frac{1}{2}V''(x_0)(x - x_0)^2 \tag{2.6}$$

which describes simple harmonic oscillator about point x_0, with an effective spring constant

$$k = V''(x_0). \tag{2.7}$$

The kinetic energy of the system is given by

$$T = \tfrac{1}{2}m\left(\tfrac{dx}{dt}\right)^2 = \tfrac{p^2}{2m} \tag{2.8}$$

where p is the momentum of the particle. We re-write the potential energy in Eq. (2.4) by substituting k with $m\omega^2$ from Eq. (2.3),

$$V = \tfrac{1}{2}m\omega^2x^2. \tag{2.9}$$

The total energy is of the system is given by

$$E = T + V = \frac{p^2}{2m} + \tfrac{1}{2}m\omega^2x^2 \tag{2.10}$$

and is constant, determined by the amplitude A of oscillation:

$$E = \tfrac{1}{2}m\omega^2A^2. \tag{2.11}$$

The simple harmonic oscillator is an important model and describes a wide range of vibrational systems. We see here that a classical harmonic oscillator can have any energy, which does not satisfy the quantized energy requirements that govern particles in the quantum domain, such as atoms in a crystal lattice. Hence a quantum mechanical treatment of harmonic oscillator is necessary.

2.2.2 The quantum mechanical harmonic oscillator

The quantum mechanical problem is to solve the Schrödinger equation for the potential given by Eq. (2.9). The Hamiltonian for the harmonic oscillator is expressed as

$$H = \frac{\hat{p}^2}{2m} + \frac{1}{2}m\omega^2\hat{x}^2 \tag{2.12}$$

where $\hat{p}$ and $\hat{x}$ are the momentum and position operators, respectively. Following the discussion by Gasiorowicz (1996), we use the fundamental commutator relation,

$$[\hat{p}, \hat{x}] = -i\hbar \tag{2.13}$$

where the commutator term is defined by [A,B] = AB – BA, and two new dimensionless operators:

$$a_+ = \sqrt{\frac{m\omega}{2\hbar}}\hat{x} - i\frac{\hat{p}}{\sqrt{2m\omega\hbar}} \tag{2.14}$$

$$a_- = \sqrt{\frac{m\omega}{2\hbar}}\hat{x} + i\frac{\hat{p}}{\sqrt{2m\omega\hbar}}\,. \tag{2.15}$$

such that the Hamiltonian can be written

$$H = \hbar\omega\left(\frac{1}{2} + a_+a_-\right). \tag{2.16}$$

Using these rules for commutators: [A+B,C] = [A,C] + [B,C] and [AB,C] = A[B,C] + [A,C]B, two commutation relations for a_+ and a_- with H can be derived:

$$[H, a_+] = \hbar\omega a_+ \tag{2.17}$$

$$[H, a_-] = -\hbar\omega a_-. \tag{2.18}$$

Now we write the Schrödinger equation:

$$H\Psi = E\Psi \tag{2.19}$$

where E is the energy eigenvalue and H is the Hamiltonian in Eq. (2.16). Taking Eq. (2.17) and having it act on a wavefunction Ψ, we get

$$Ha_+\Psi - a_+H\Psi = \hbar\omega a_+\Psi\ . \tag{2.20}$$

Inserting Eq. (2.19) this becomes

$$Ha_+\Psi = (E + \hbar\omega)a_+\Psi\ . \tag{2.21}$$

Likewise, when Eq. (2.18) acts on a wavefunction Ψ,

$$Ha_-\Psi = (E - \hbar\omega)a_-\Psi\ . \tag{2.22}$$

As we can see the operators a_+ and a_- allows us to climb up and down in energy and thus are appropriately called *ladder operators*. The application of a_+ to a wavefunction generates a state of higher energy by $\hbar\omega$; hence a_+ is called a *raising* operator. The application of a_- lowers the energy by $\hbar\omega$; hence a_- is referred to as a *lowering* operator. Figure 2.1 shows an illustration of this "ladder" of states.

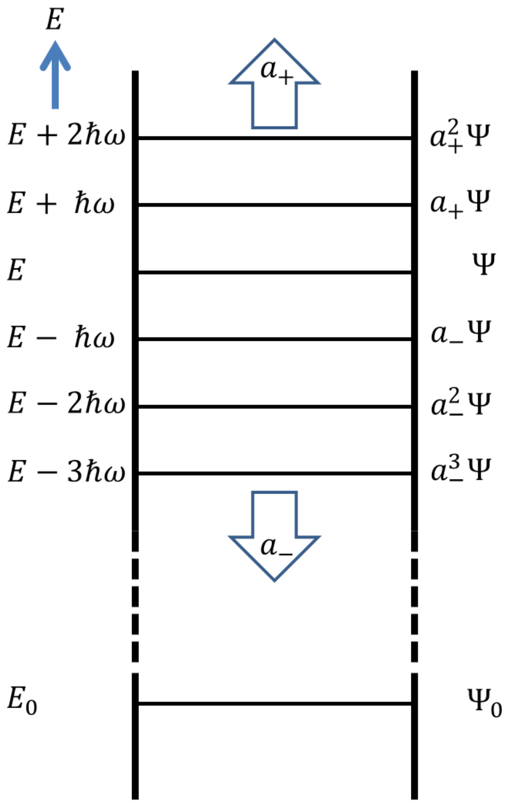

Figure 2.1: The "ladder" of stationary states for the simple harmonic oscillator.

Since the energy E must be positive, there is a limit to how many times the lowering operator can be applied. That is, there is a ground state beyond which lowering ends. At the ground state,

$$a_-\Psi_0 = 0, \tag{2.23}$$

and the energy is given by

$$H\Psi_0 = \left(\frac{1}{2}\hbar\omega + \hbar\omega a_+ a_-\right)\Psi_0 = \frac{1}{2}\hbar\omega\Psi_0 \tag{2.24}$$

Therefore,

$$E_0 = \frac{1}{2}\hbar\omega. \tag{2.25}$$

By simply applying the raising operator to generate the excited states, we obtain the energy eigenvalues of a simple harmonic oscillator:

$$E_n = \left(n + \tfrac{1}{2}\right)\hbar\omega. \tag{2.26}$$

Figure 2.2 shows a sketch of the eigenfunctions of Eq. (2.12) and the energy levels of Eq. (2.26) represented by the horizontal dashed lines. Each wavefunction is drawn using the energy line as the *x*-axis.

The ground state wavefunction can be determined by plugging in the lowering operator in Eq. (2.23):

$$\left(\sqrt{\frac{m\omega}{2\hbar}}\,\hat{x} + i\,\frac{\hat{p}}{\sqrt{2m\omega\hbar}}\right)\Psi_0 = 0 \tag{2.27}$$

so that the one-dimensional differential equation to solve is

$$\left(\frac{m\omega}{\hbar}x + \frac{d}{dx}\right)\Psi_0(x) = 0. \tag{2.28}$$

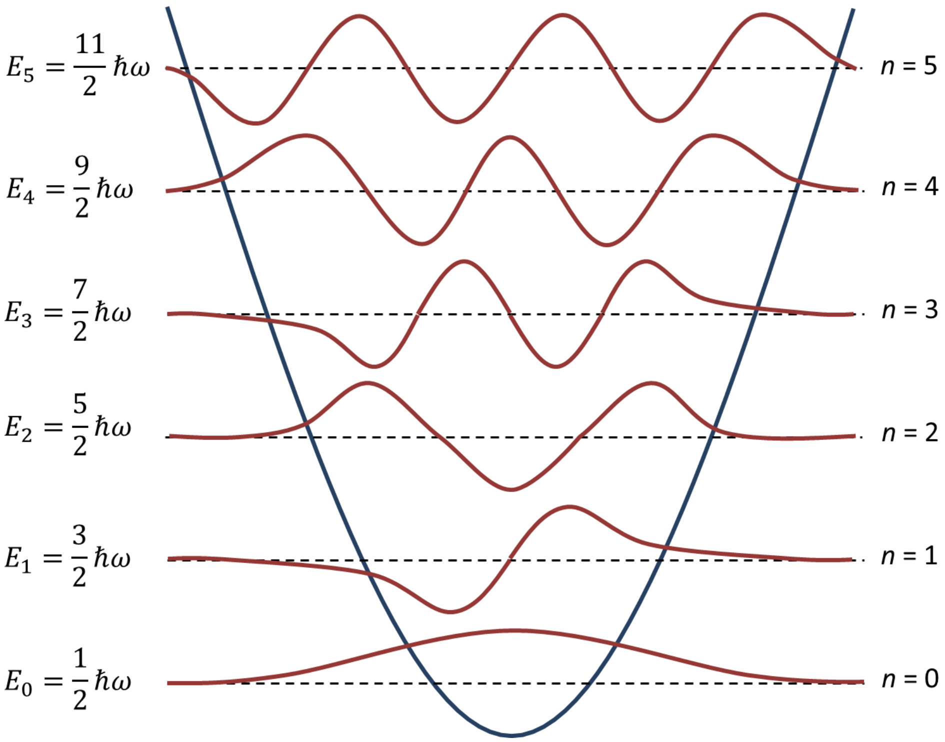

Figure 2.2: Eigenfunctions and energies of a quantum mechanical harmonic oscillator.

The solution to Eq. (2.28) is

$$\Psi_0(x) = c_0 e^{\frac{-m\omega}{2\hbar}x^2}. \tag{2.29}$$

From this bottom rung of the *ladder* we apply the raising operator so that the wavefunction for each state of the quantum harmonic oscillator is

$$\Psi_n(x) = c_n (a_+)^n e^{\frac{-m\omega}{2\hbar}x^2} \tag{2.30}$$

where c_n is the normalization constant which can be worked out and the result is

$$c_n = \left(\frac{m\omega}{\pi\hbar}\right)^{1/4} \frac{(-i)^n}{\sqrt{n!(\hbar\omega)^n}}. \tag{2.31}$$

The wavefunction in three dimensions is obtained by separating it into the three normal coordinates:

$$\Psi(x,y,z) = \Psi_x(x)\Psi_y(y)\Psi_z(z). \tag{2.32}$$

The Hamiltonian and the energy eigenvalues for the three-dimensional harmonic oscillator are

$$H = \frac{\hat{p}^2}{2m} + \frac{1}{2}m\left({\omega_x}^2\hat{x}^2 + {\omega_y}^2\hat{y}^2 + {\omega_z}^2\hat{z}^2\right) \tag{2.33}$$

and

$$E = E_x + E_y + E_z = \hbar\left[n_x\omega_x + n_y\omega_y + n_z\omega_z + \frac{1}{2}(\omega_x + \omega_y + \omega_z)\right]. \tag{2.34}$$

2.3 Lattice vibrations

Atoms in a crystal are not fixed at rigid sites on the lattice, but are vibrating about their equilibrium positions. In this section I will discuss the vibrations of the atoms in a crystalline solid. I will start with the vibrational properties of a linear chain of identical atoms, the monatomic linear chain, since many of the significant features of lattice vibrations can be understood on the basis of this simple one-dimensional model. Then I will delve into the diatomic linear chain as we have many important compound semiconductors consisting of two different atoms.

2.3.1 Monatomic linear chain of atoms

We will consider a linear chain of identical atoms of mass M which interact only through nearest-neighbor forces (Fig. 2.3). Following the treatment given by Kittel (2005), we assume that the net restoring force is proportional to the atom's displacement relative to its nearest neighbors. If we denote the displacement of atom n from its equilibrium position as r_n, the force on it caused by the displacement of the nearest-neighbor interactions is

$$F = k(r_{n+1} - r_n) + k(r_{n-1} - r_n) \tag{2.35}$$

where k is the force constant between the nearest-neighbor atoms.

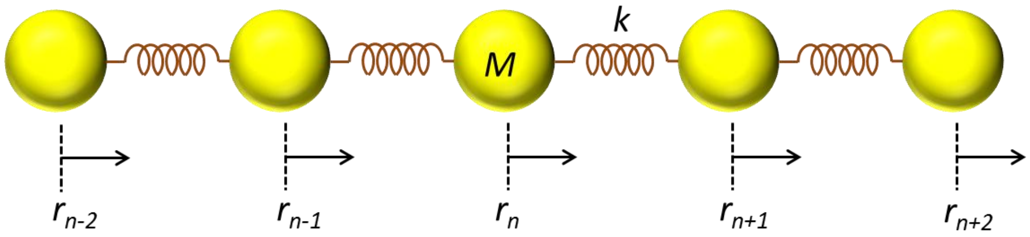

Figure 2.3: A monatomic linear chain of atoms with mass M.

The equation of motion of an atom n is given by

$$M\left(\frac{d^2 r_n}{dt^2}\right) = k(r_{n+1} + r_{n-1} - 2r_n). \tag{2.36}$$

Given the oscillatory motion of the atoms around their equilibrium positions, all displacements have the time-dependence $e^{-i\omega t}$ so $(d^2 r_n/dt^2) = -\omega^2 r_n$. Therefore Eq. (2.36) becomes

$$-M\omega^2 r_n = k(r_{n+1} + r_{n-1} - 2r_n) \tag{2.37}$$

with solutions in the form of propagating wave:

$$r_n = re^{inKa}, \tag{2.38}$$

where a is the interatomic spacing and K is the magnitude of the wavevector.

Using Eq. (2.38), we write Eq. (2.37) in the form

$$-\omega^2 M r e^{inKa} = kr[e^{i(n+1)Ka} + e^{i(n-1)Ka} - 2e^{inKa}], \tag{2.39}$$

and, after cancelling re^{inKa} on both sides, simplify to

$$-\omega^2 M = k(e^{iKa} + e^{-iKa} - 2) \tag{2.40}$$

Using the identity $2\cos(Ka) = e^{iKa} + e^{-iKa}$, we get the *dispersion relation* $\omega(\boldsymbol{K})$

$$\omega = \left[2\frac{k}{M}(1 - \cos Ka)\right]^{\frac{1}{2}}. \tag{2.41}$$

Using the trigonometric identity $1 - \cos Ka = 2\sin^2\frac{Ka}{2}$, the dispersion relation may also be written as

$$\omega = 2\sqrt{\frac{k}{M}}\left|\sin\frac{Ka}{2}\right|. \tag{2.42}$$

A plot of the dispersion relation ω vs $\boldsymbol{K}$ for a monatomic linear chain is shown in Fig. 2.4. As atoms occupy discrete positions in the lattice, a phonon of wavelength a is equivalent to $a/2$, $a/3$, etc. The range of wavevectors $\boldsymbol{K}$ that is physically significant to describe all the phonon modes is referred to as the *first Brillouin zone*. In Fig. 2.4, the first Brillouin zone is comprised of $-\pi/a < K \leq \pi/a$. Wavevectors outside the boundaries of Brillouin zone can be “folded” back into the first Brillouin zone.

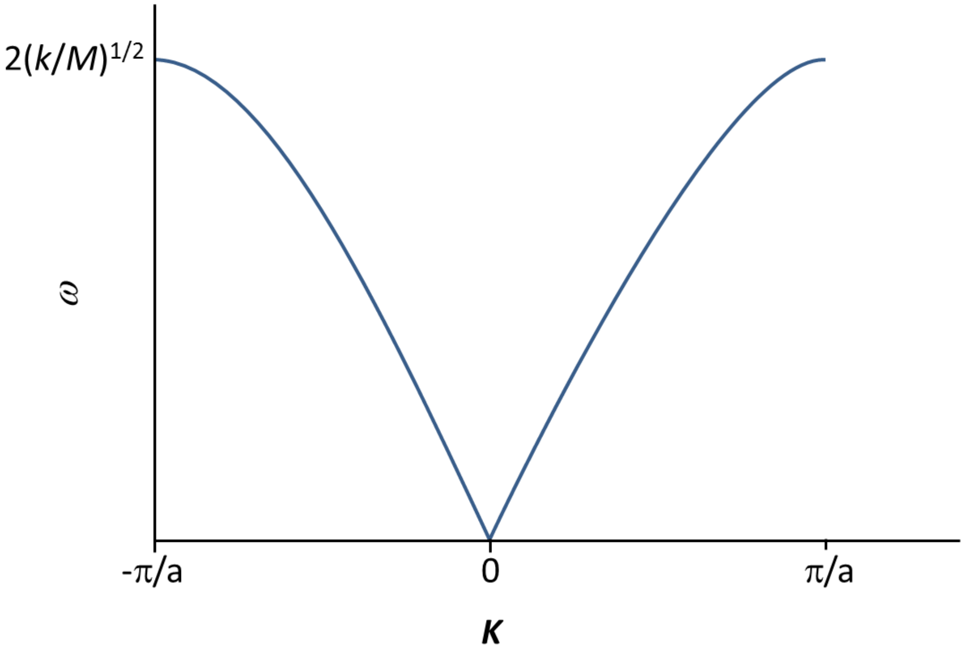

Figure 2.4: Dispersion relation in the first Brillouin zone for a monatomic linear chain.

2.3.2 Diatomic linear chain of atoms

Now let us consider a linear chain of atoms consisting of two different types arranged in an alternating pattern (Fig. 2.5). The atoms of mass M_1 and M_2 are located at positions r_n and s_n, respectively. As in the previous case, only nearest-neighbor interactions are considered and with the same force constant k between all pairs. The interatomic distance is $a/2$ and the lattice constant is a. Taking a similar flow of discussion as in Kittel (2005), we write the equations of motion of the two masses:

$$M_1\left(\frac{d^2r_n}{dt^2}\right) = k(s_n + s_{n-1} - 2r_n);$$
$$M_2\left(\frac{d^2s_n}{dt^2}\right) = k(r_{n+1} + r_n - 2s_n). \tag{2.43}$$

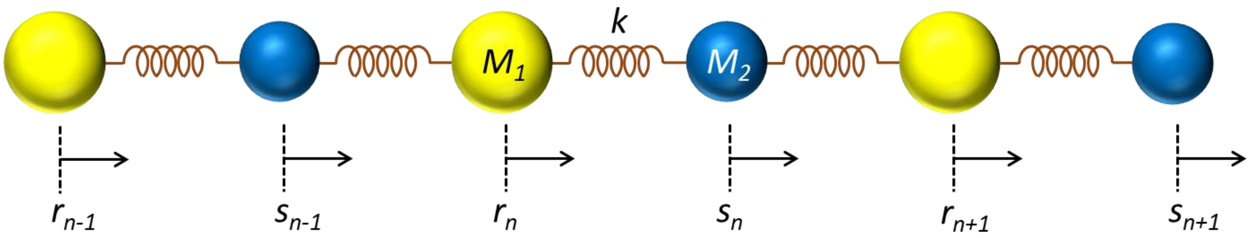

Figure 2.5: A diatomic linear chain of atoms with mass M_1 and M_2.

As in the monatomic linear chain, the solutions will take the form of a traveling wave, but now with different amplitudes, r and s, on alternating atomic planes:

$$r_n = re^{inKa}e^{-i\omega t};$$
$$s_n = se^{inKa}e^{-i\omega t}. \tag{2.44}$$

Substituting the solutions, given in Eq. (2.44), into Eq. (2.43), we have

$$-\omega^2 M_1 r = ks\left(1 + e^{-iKa}\right) - 2kr;$$
$$-\omega^2 M_2 s = kr\left(e^{iKa} + 1\right) - 2ks. \tag{2.45}$$

To solve the set of linear equations (2.45), we set the determinant of the matrix to zero:

$$\begin{vmatrix} 2k - M_1\omega^2 & -k\left(1 + e^{-iKa}\right) \\ -k\left(1 + e^{iKa}\right) & 2k - M_2\omega^2 \end{vmatrix} = 0 \tag{2.46}$$

or

$$M_1 M_2 \omega^4 - 2k(M_1 + M_2)\omega^2 + 2k^2(1 - \cos Ka) = 0 \tag{2.47}$$

Solving ω^2 from the resultant quadratic equation (2.47), we obtain

$$\omega^2 = k\left(\frac{1}{M_1} + \frac{1}{M_2}\right) \pm k\sqrt{\left(\frac{1}{M_1} + \frac{1}{M_2}\right)^2 - \frac{4}{M_1 M_2}\sin^2\left(\frac{Ka}{2}\right)}. \tag{2.48}$$

However it is simpler to examine the limiting cases $Ka \ll 1$ and $Ka = \pm\pi$ at the Brillouin zone boundary with Eq. (2.47). For small Ka we use the expansion $\cos Ka \cong 1 - \frac{1}{2}K^2a^2 + \cdots$, and the two roots are

$$\omega^2 \cong 2k\left(\frac{1}{M_1}+\frac{1}{M_2}\right) \tag{2.49}$$

$$\omega^2 \cong \frac{\frac{1}{2}k}{M_1+M_2}K^2a^2 \tag{2.50}$$

Equation (2.49) represents the dispersion relation for the optical phonon branch while Eq. (2.50) represents the acoustic phonon branch. For $K = \pm\frac{\pi}{a}$, we have the following roots:

$$\omega^2 = \frac{2k}{M_1}; \tag{2.51}$$

$$\omega^2 = \frac{2k}{M_2}. \tag{2.52}$$

The dispersion relation ω vs K for a diatomic linear chain is shown in Fig. 2.6. The upper branch is the optical branch, and at $K = 0$, we find the amplitude ratio by substituting Eq. (2.49) in Eq. (2.45):

$$\frac{r}{s} = -\frac{M_2}{M_1}. \tag{2.53}$$

This means that the atomic displacements are in opposite directions, but their center of mass is fixed. If the two atoms carry opposite charge, these modes may be excited by interaction with the electric field of a light wave, hence the branch is called the optical branch. The lower branch of the dispersion curve is the acoustic branch. At $K = 0$ limit of Eq. (2.50) and on substitution in Eq. (2.45), we obtain $r = s$, which corresponds to atomic displacements in the same direction, as in long wavelength acoustic vibrations, thus the acoustic branch is given its name.

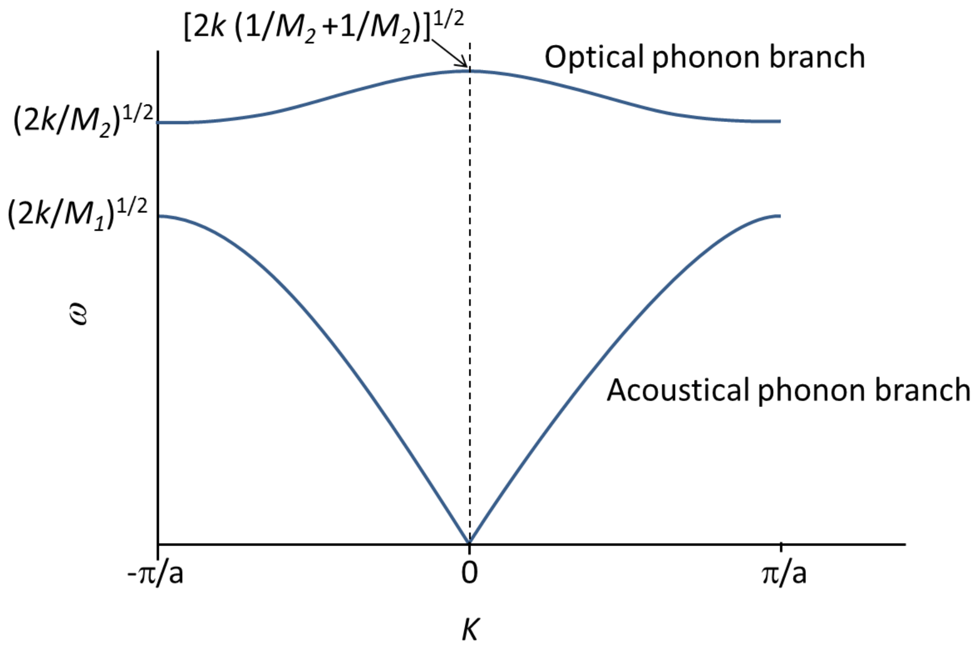

Figure 2.6: Dispersion relation in the first Brillouin zone for diatomic linear chain of atoms with $M_1 > M_2$.

2.4 Local vibrational modes (LVMs)

When an impurity is introduced into a crystal, the translational symmetry of the pure lattice is broken. Let us consider again the monatomic linear chain discussed in Section 2.1, but this time let us replace one lattice mass by a smaller mass *m*. Our goal is to show that one of the normal modes of the lattice will be localized around the smaller atom *m*. As in Sec. 2.1, we write the lattice equations of motion, and in this case, one equation for the lighter atom *m* and another for the host atom *M*, and we let atom *m* occupy the *n* = 0 position. Hence,

$$m\left(\frac{d^2r_0}{dt^2}\right) = k(r_1 + r_{-1} - 2r_0) \tag{2.54}$$

$$M\left(\frac{d^2r_1}{dt^2}\right) = k(r_2 + r_0 - 2r_1). \tag{2.55}$$

As shown in Sec. 2.1 the solution to the perfect lattice is given by Eq. (2.42): $\omega = 2\sqrt{\frac{k}{M}}\left|\sin\frac{Ka}{2}\right|$. Now if we look at an expression of sine function provided by Euler's formula, $\sin x = (e^{ix} - e^{-ix})/2i$, we let the wavenumber K be complex so that we obtain a normal mode with a frequency higher than the phonon frequencies:

$$K = K_{\mathbb{R}} + iK_{\mathbb{I}} \tag{2.56}$$

From Euler's formula, we generate the identity

$$\sin\left(\frac{Ka}{2}\right) = \frac{\left(e^{iK_{\mathbb{R}}a/2}e^{-K_{\mathbb{I}}a/2} - e^{-iK_{\mathbb{R}}a/2}e^{K_{\mathbb{I}}a/2}\right)}{2i}$$

$$= \sin\left(\frac{K_{\mathbb{R}}a}{2}\right)\cosh\left(\frac{K_{\mathbb{I}}a}{2}\right) - i\cos\left(\frac{K_{\mathbb{R}}a}{2}\right)\sinh\left(\frac{K_{\mathbb{I}}a}{2}\right) \tag{2.57}$$

For the frequency in Eq. (2.42) to be real, the imaginary component must equal zero. This suggests that $K_{\mathbb{R}} = \frac{\pi}{a}$. The displacement *r* of atom in position n is given by

$$r_n = r_0 e^{-i\pi n} e^{-K_{\mathbb{I}}a} e^{-i\omega t} = r_0(-1)^n e^{-K_{\mathbb{I}}a} e^{-i\omega t}. \tag{2.58}$$

As we can see from above equation (2.58), the amplitude undergoes exponential decay with distance from the impurity. Substituting it into Eqs. (2.54) and (2.55), respectively, we obtain

$$\omega^2 = \frac{k}{m}(2 + 2e^{K_{\mathbb{I}}a}) \tag{2.59}$$

$$\omega^2 = \frac{k}{M}(2 + e^{-K_{\mathbb{I}}a} + e^{K_{\mathbb{I}}a}) \tag{2.60}$$

Solving Eqs. (2.59) and (2.60) simultaneously, we have

$$e^{-i\omega t} = \frac{2M-m}{m} \tag{2.61}$$

and

$$\omega^2 = {\omega_{max}}^2 \frac{M^2}{2Mm-m^2} \tag{2.62}$$

where $\omega_{max} = \sqrt{\frac{4k}{M}}$ is the maximum frequency of the unperturbed linear chain. Now if $m \ll M$, we can express Eq. (2.62) approximately as

$$\omega^2 \approx {\omega_{max}}^2 \frac{M}{2m}, \tag{2.63}$$

which indicates that there exists an LVM frequency above the highest phonon frequency.

2.4.1 Isotopic shift

To identify a particular impurity producing a given LVM signature, an isotope is substituted in place of the impurity (Haller, 1995). The isotope will bond in the same manner as its counterpart, but the LVM frequency will be different. The shift in frequency is referred to as isotopic shift. If we model the impurity, with mass *m*, as attached to the lattice whose mass is represented by *M* by a spring of force constant *k* (Fig. 2.7), we can use the diatomic model to solve the vibrational frequency:

$$\omega = \sqrt{k\left(\frac{1}{M} + \frac{1}{m}\right)} \equiv \sqrt{\frac{k}{\mu}}, \tag{2.64}$$

where $\mu = \left(\frac{1}{M} + \frac{1}{m}\right)^{-1}$ is the reduced mass of the system. Suppose hydrogen ($m = 1$ amu) is suspected to be responsible for an observed LVM. This can be verified by replacing hydrogen by deuterium ($m = 2$ amu). The ratio between frequencies is given by

$$r = \frac{\omega_H}{\omega_D} = \sqrt{2\frac{M+1}{M+2}}, \tag{2.65}$$

where ω_H and ω_D are the LVM frequencies of the hydrogen and deuterium, respectively. The isotopic frequency ratio *r* is slightly less than $\sqrt{2}$ due to the finite lattice mass *M* and that the lattice is not perfectly rigid. Nonetheless, the diatomic model has proved to be a useful empirical model to determine the frequencies and isotope shifts of a numerous LVMs (Haller, 1995).

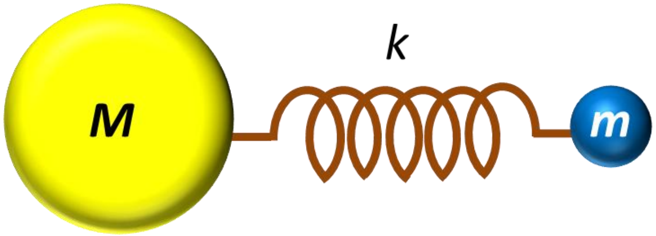

Figure 2.7: Diatomic model for LVM.

2.4.2 Anharmonicity

We have assumed a harmonic potential in the models discussed so far. However, real potentials are not perfectly parabolic; rather, they exhibit anharmonicity (Newman, 1990) as displacements become larger. The Morse potential (Morse, 1929) is a model that attempts to account for this effect, and is given by

$$V(x) = D_e\left(e^{-\beta x} - 1\right)^2, \tag{2.66}$$

where D_e is the binding energy. For small displacements x from equilibrium, the Morse potential (Fig. 2.8) approximates a harmonic potential, with a force constant $k = 2D_e\beta^2$.

Anharmonicity is one of the factors that reduces the isotopic frequency ratio derived in Sec. 2.3.1. This effect is demonstrated quantitatively by considering the energy eigenvalues of the Morse potential, which is given by

$$E_n = \tfrac{1}{2}\hbar\omega_e\left(n + \tfrac{1}{2}\right)\left[1 - x_e\left(n + \tfrac{1}{2}\right)\right], \tag{2.67}$$

where

$$\omega_e = \beta\left(\frac{2D_e}{\mu}\right)^{\frac{1}{2}}, \tag{2.68}$$

and

$$\omega_e x_e = \frac{\hbar\beta^2}{2\mu}. \tag{2.69}$$

The first excited state is given by

$$\Delta E = E_1 - E_0 = \hbar\omega_e - 2\hbar\omega_e x_e. \tag{2.70}$$

The anharmonic term $\omega_e x_e$ varies inversely with the reduced mass, as Eq. (2.69) shows. Thus, the anharmonic term is greater for hydrogen than for deuterium. Since hydrogen has larger amplitude of vibration than the deuterium, its wavefunction samples more of the anharmonicity. Therefore its frequency is reduced relative to the deuterium frequency, so that their frequency ratio $r = \omega_H/\omega_D$ is lowered.

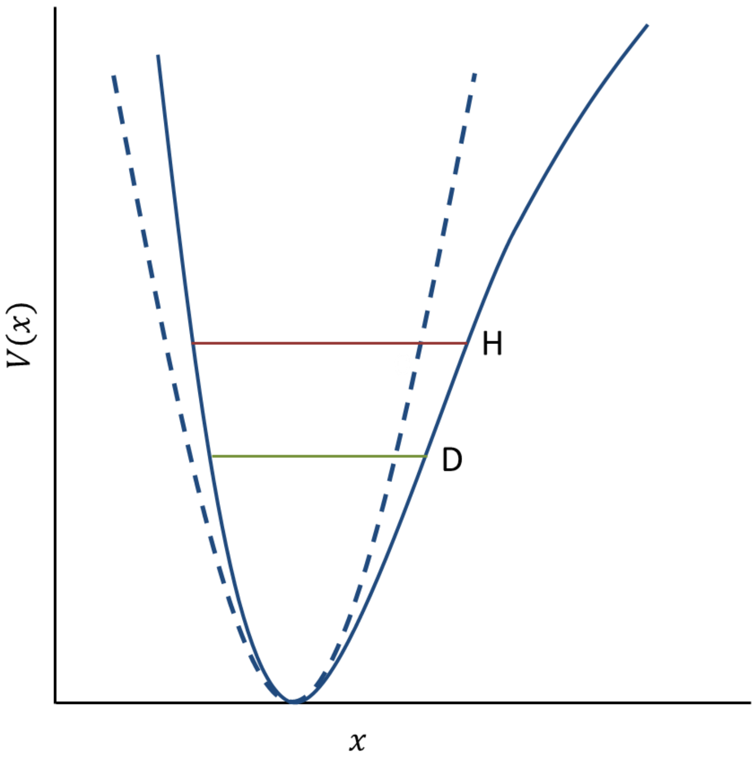

Figure 2.8: The Morse potential with the parabolic potential (dashed line) for comparison. Also shown are the hydrogen and deuterium ground states.

2.5 Infrared Absorption

To probe the vibrational spectrum of a defect, infrared (IR) radiation is passed through the sample. A photon can be absorbed by the defect and its energy transformed into vibrational excitation. The energy at which a peak in the IR absorption spectrum appears corresponds to the vibrational frequency related to the defect. Hence, IR absorption spectroscopy is an important and essential technique for materials analysis. I used this method to obtain most of the results presented in this thesis.

In this section, the derivation of the absorption cross section of an oscillating dipole using the classical approach is shown. As in the preceding sections, we will use the masses-spring system to model our oscillating dipole. Two masses M and m, each carrying an electric charge $+q$ and $-q$, respectively, are connected to each other by a spring with a force constant k. The equation of motion is given by

$$\mu \frac{d^2r}{dt^2} + \mu\gamma \frac{dr}{dt} + \mu{\omega_0}^2 r = -qE(t), \tag{2.71}$$

where γ is a damping constant, $\mu = \left(\frac{1}{M} + \frac{1}{m}\right)^{-1}$ is the reduced mass, $\omega_0 = \sqrt{k/\mu}$ is the natural angular frequency, and $E(t)$ is the electric field. The electric field is assumed to be monochromatic with a frequency ω, that is,

$$E(t) = E_0 e^{-i\omega t}. \tag{2.72}$$

The solution to Eq. (2.71) is given by

$$r(t) = r_0 e^{-i\omega t}, \tag{2.73}$$

which, when substituted into Eq. (2.71), gives

$$-\mu\omega^2 r_0 e^{-i\omega t} - i\mu\gamma\omega r_0 e^{-i\omega t} + \mu{\omega_0}^2 r_0 e^{-i\omega t} = -qE_0 e^{-i\omega t},$$

giving the amplitude r_0:

$$r_0 = \frac{qE_0/\mu}{{\omega_0}^2 - \omega^2 - i\gamma\omega}. \tag{2.73}$$

The polarization for N dipoles per unit volume is determined by

$$\begin{aligned} P &= Ner \\ &= \frac{Nq^2}{\mu} \frac{1}{{\omega_0}^2 - \omega^2 - i\gamma\omega} E(t). \end{aligned} \tag{2.74}$$

The dielectric constant $\varepsilon = 1 + \frac{4\pi P}{E}$ is given by

$$\varepsilon(\omega) = 1 + \frac{4\pi N q^2}{\mu} \frac{1}{{\omega_0}^2 - \omega^2 - i\gamma\omega}\,, \tag{2.75}$$

where the oscillator strength of this simple dipole is equal to unity. Oscillator strength gives a measure of the intensity of the transition that the dipole undergoes.

To solve the rate of absorption of energy of the oscillating dipole, we will first get the relative velocity of the two masses by taking the derivative of Eq. (2.73),

$$v(t) = i\omega r_0 e^{-i\omega t}. \tag{2.76}$$

Then we can calculate the power absorbed per unit volume by the dipole:

$$\mathcal{P}(t) = q\Re\mathrm{e}[E(t)]\Re\mathrm{e}[v(t)], \tag{2.77}$$

which gives

$$\begin{aligned} \mathcal{P}(t) &= \frac{q^2 {E_0}^2 \omega}{\mu} \cos\omega t \, \Re\mathrm{e}\left[\frac{({\omega_0}^2 - \omega^2) - i\gamma\omega}{({\omega_0}^2 - \omega^2)^2 + \gamma^2\omega^2} (i\cos\omega t - \sin\omega t)\right] \\ &= \frac{q^2 {E_0}^2 \omega}{\mu} \cos\omega t \frac{\gamma\omega\cos\omega t - ({\omega_0}^2 - \omega^2)\sin\omega t}{({\omega_0}^2 - \omega^2)^2 + \gamma^2\omega^2}, \end{aligned} \tag{2.78}$$

where we assumed E_0 to be real. Now, solving the time-averaged power $\langle\mathcal{P}\rangle$ absorbed by the dipole, we note the fact that $\langle\cos^2\omega t\rangle = \frac{1}{2}$ and$\langle\sin\omega t\cos\omega t\rangle = 0$, hence

$$\langle\mathcal{P}\rangle = \frac{q^2 {E_0}^2 \omega^2 \gamma / 2\mu}{({\omega_0}^2 - \omega^2)^2 + \gamma^2\omega^2}. \tag{2.79}$$

The *absorption cross-section* is given by the ration of the power dissipation to the intensity of the electromagnetic wave,

$$\sigma = \frac{\langle \mathcal{P} \rangle}{ncE_0{}^2/8\pi}$$

$$= \frac{4\pi q^2 \omega^2 \gamma}{n\mu c} \frac{1}{(\omega_0{}^2 - \omega^2)^2 + \gamma^2 \omega^2}\,, \tag{2.80}$$

where *n* is the index of refraction and *c* is the speed of light. The cross-section defines an effective area in which incident light is totally absorbed. It is expressed in units of cm^2. The damping factor is approximately the full width at half maximum (FWHM) of the absorption peak.

Consider an electromagnetic wave incident on a material with *N* dipoles per cm^3. Let I_0 be the intensity of the electromagnetic wave entering an infinitesimal slab of this material of area A and thickness *dz*, and *dI* be the intensity absorbed in the slab while I be the transmitted intensity. The fraction of photons absorbed per unit area will be $\frac{\sigma N A dz}{A} = \sigma N dz$. Thus

$$\frac{dI}{I} = -\sigma N dz. \tag{2.81}$$

The solution to this differential equation is obtained by integrating both sides and yields

$$I = I_0 e^{-\sigma N z} = I_0 e^{-\alpha z}, \tag{2.82}$$

where α is the *absorption coefficient* expressed in units of cm^{-1}.

The integrated absorption is defined as

$$\mathcal{A} = \int_0^\infty \alpha(\omega) d\omega = N \int_0^\infty \sigma(\omega) d\omega. \tag{2.83}$$

Inserting the absorption cross-section given by Eq. (2.80) in Eq. (2.83),

$$\mathcal{A} = \frac{4\pi N q^2 \gamma}{n\mu c} \int_0^\infty \omega^2 \frac{d\omega}{(\omega_0{}^2 - \omega^2)^2 + \gamma^2 \omega^2}. \tag{2.84}$$

In the limit $\gamma \ll \omega_0$, the integrand is nonzero only in a narrow range about ω_0. Hence we can write

$$\omega = \omega_0 + \delta\omega, \tag{2.85}$$

where $\delta\omega \ll \omega_0$. Substituting this into the integral in Eq. (2.84), and keeping the lowest order $\delta\omega$ and γ terms, we have

$$\mathcal{A} = \frac{4\pi N q^2 \gamma}{n\mu c} \int_0^\infty \frac{d(\delta\omega)}{4(\delta\omega)^2+\gamma^2}, \tag{2.86}$$

where the integrand is a Lorentzian function. By trigonometric substitution, the integral can be solved and Eq. (2.86) becomes

$$\mathcal{A} = N \frac{2\pi^2 q^2}{n\mu c}, \tag{2.87}$$

where the units are given in cm^{-1}rad/s. In practice, *wavenumbers* are often use in spectroscopy, defined as the reciprocal of the wavelength, $1/\lambda$. The conversion between wavenumber and angular frequency is $\frac{1}{\lambda} = \frac{\omega}{2\pi c}$, which yields

$$\mathcal{A} = N \frac{\pi^2 q^2}{n\mu c^2} \tag{2.88}$$

in the unit cm^{-2}. This result shows that integrated absorption is independent of the frequency ω_0 and the width γ of the peak. A quantum-mechanical approach, which applies Thomas-Reiche-Kuhn sum rule, yields similar result (McHale, 1999). The classical interpretation of the meaning of oscillator strength is consistent with the sum rule.

2.6 Temperature dependence

Increasing the temperature of a semiconductor results in lattice expansion and increase in thermal population of phonon modes. Two models describe the interaction between the LVM and the phonons (McCluskey and Haller, 1999; McCluskey, 2000). The first model assumes the LVM interacts with all the phonon modes (Eliot et al., 1965), suggesting that the LVM shift, $\delta(\nu)$, is proportional to the thermal lattice energy $U(T)$:

$$\delta(\nu) = \frac{\beta}{N_A} U(T), \tag{2.89}$$

$$U(T) = \frac{N}{2} k \sum_{\mathbf{q}} A_{\mathbf{q}}{}^2, \tag{2.90}$$

where $A_{\mathbf{q}}$ is the amplitude of vibration, N is the number of atoms, and k is the nearest-neighbor force constant. The broadening of the line-width is found to be proportional to the square of the absolute temperature (Elliot et al., 1965). This model was used to explain the temperature dependence of LVMs in GaP (McCluskey et al., 1995).

In the second model, the LVM is assumed to interact with a single phonon (McCluskey and Haller, 1999). The temperature-dependent energy shift is given by

$$\delta(\nu) = \frac{\delta\nu_0}{e^{h\nu_0/kT} - 1} \tag{2.91}$$

and the line-width broadening is given as

$$\delta\Gamma = \frac{2(\delta\nu_0)^2}{\eta} \frac{e^{h\nu_0/kT}}{\left(e^{h\nu_0/kT} - 1\right)^2}, \tag{2.92}$$

where $\delta\nu_0$, ν_0, and η are adjustable parameters. The temperature dependence of the LVMs in GaAs are well-described by this model (Vetterhöffer and Weber, 1996).

CHAPTER 3 EXPERIMENTAL TECHNIQUES

3.1 Fourier transform infrared (FTIR) spectroscopy

Fourier transform infrared (FTIR) spectroscopy is a preferred technique in infrared spectroscopy because it has the advantages of faster scanning process, higher sensitivity, and greater optical throughput than grating monochromators. We use FTIR spectroscopy to probe local vibrational modes and free carrier absorption in our samples. The main component of an FTIR spectrometer is a Michelson interferometer (Fig. 3.1). It has a beamsplitter which takes the parallel infrared beam from a broadband source and splits it into two optical beams. One beam is directed to a fixed mirror while the other beam is directed to a moving mirror. The two beams reflect off their respective mirrors and recombine at the beamsplitter. The beam that leaves the interferometer is a superposition of these beams. This beam enters the sample compartment where it is transmitted through or reflected off the sample (depending on the type of analysis being carried out). This is where specific frequencies of energy, characteristic of the sample or defects in the sample, are absorbed. The beam finally passes to the detector for final measurement. The resulting signal is called an *interferogram* and every data point is a function of the moving mirror position and has information about every infrared frequency that reaches the detector. As the interferogram is measured, all frequencies are being measured simultaneously, resulting to extremely fast measurements.

To make a meaningful interpretation of the interferogram, we need convert it into a plot of the spectrum in frequency space. This can be accomplished by applying a well-known mathematical algorithm called a Fourier transform, performed by the computer which then presents the desired frequency spectrum, that is, a plot of the intensity as a function of frequency.

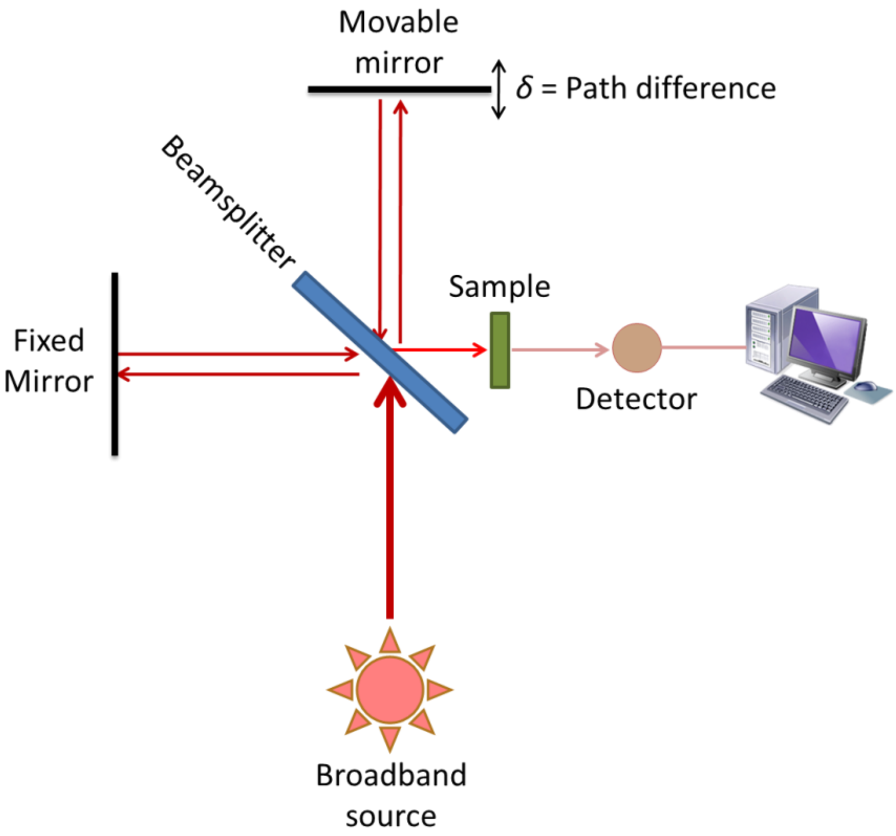

Figure 3.1: Michelson interferometer

3.1.1 Derivation of Fourier result

The spectral equation used in Fourier transform spectroscopy will be derived in this section, following the procedure given by Bell (1972). Consider an incident beam of light on the beamsplitter with an electric field given by

$$E(x,k) = E_0 e^{ikx-\omega t}, \tag{3.1}$$

where $k = \frac{2\pi}{\lambda}$ and x is the distance along the beam. After amplitude splitting, the two beams in the Michelson interferometer have traveled distances x_1 and x_2, respectively. They recombine to form a resultant electric field

$$E_R(x_1, x_2, k) = E_0(k)[e^{i(kx_1-\omega t)} + e^{i(kx_2-\omega t)}]. \tag{3.2}$$

The intensity of the electromagnetic wave for a particular value of k is given (within a multiplying factor) by the square of the electric field:

$$I_R = E_R {E_R}^*. \tag{3.3}$$

Substituting Eq. (3.2) yields

$$\begin{aligned} I_R(x_1, x_2, k) &= {E_0}^2(k)[2 + e^{ik(x_1-x_2)} + e^{-ik(x_1-x_2)}] \\ &= {E_0}^2(k)[2 + e^{ik\delta} + e^{-ik\delta}], \end{aligned} \tag{3.4}$$

where $\delta = x_1 - x_2$. Using the definition $\cos z = \frac{e^{iz}+e^{-iz}}{2}$, Eq. (3.4) can be written

$$I_R(x_1, x_2, k) = 2{E_0}^2(k)[1 + \cos k\delta]. \tag{3.5}$$

The total intensity at any path difference δ is obtained by integrating over k:

$$I_R(\delta) = \int_0^\infty I(\delta, k) dk \tag{3.6}$$

$$I_R(\delta) = 2\int_0^\infty {E_0}^2(k) dk + 2\int_0^\infty {E_0}^2(k) \cos k\delta \, dk. \tag{3.7}$$

This is the interferogram. The first term of Eq. (3.7) is a constant, so we take it as an offset term, and only the second term varies with δ. Then Eq. (3.7) becomes

$$I_R(\delta) = 2\int_0^\infty {E_0}^2(k) \cos k\delta \, dk. \tag{3.8}$$

Ignoring proportionality constant as before, we may replace $2{E_0}^2(k)$ by $I_0(k)$:

$$I_R(\delta) = \int_0^\infty I_0(k) \cos k\delta \, dk, \tag{3.9}$$

which is simply the Fourier transform of the intensity $I_0(k)$. To obtain the spectrum $I_0(k)$, we perform an inverse Fourier transform:

$$I_0(k) = \int_0^\infty I_R(\delta) \cos k\delta \, d\delta. \tag{3.10}$$

Hence, within a multiplicative constant, the spectrum in frequency space can be computed by the Fourier transform of the interferogram. Figure 3.2 shows an example of an interferogram and the corresponding frequency spectrum.

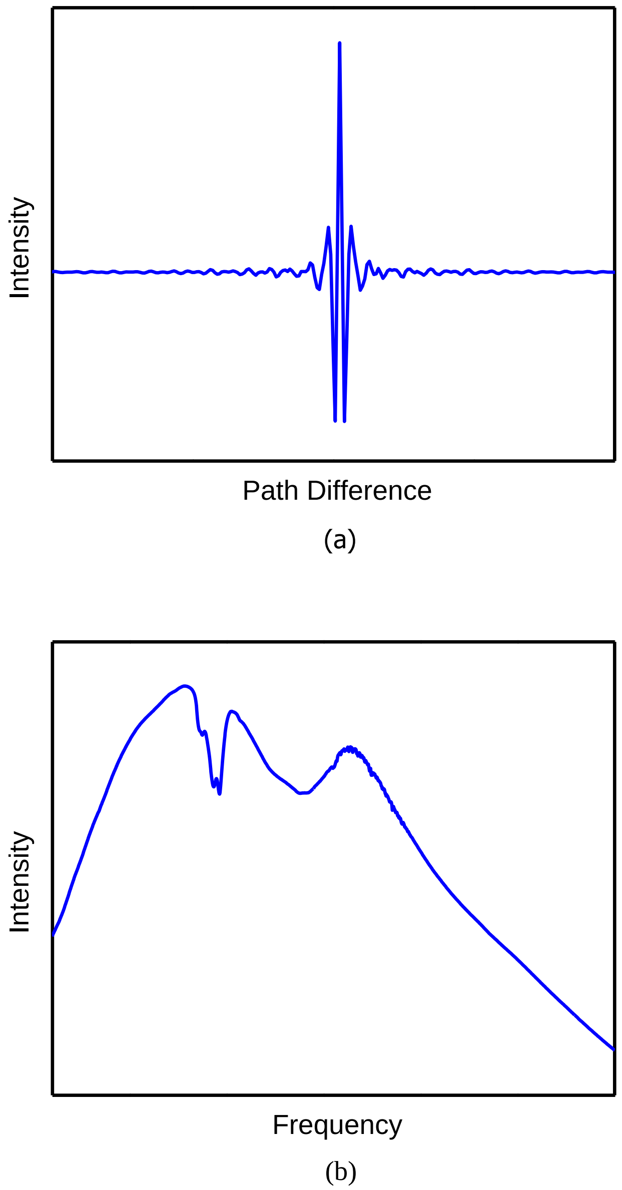

(a)

(b)

Figure 3.2: Plots of an (a) interferogram and its (b) Fourier transform.

3.1.2 Resolution and apodization

As shown in the preceding derivation, the path length difference δ was assumed to vary from 0 to ∞. In an actual instrument, however, the scanning mirror may move only a finite range L (typically a few centimeters). Assume a monochromatic source with an intensity given by

$$I_0(k) = I_0\delta(k - k_0), \tag{3.11}$$

where δ is the Dirac delta function which can describe a perfectly sharp absorption peak. Inserting this into Eq. (3.9) yields

$$I(\delta) = I_0 \cos k_0\delta. \tag{3.12}$$

Now if an absorption peak is described by a delta function, the peak measured by the FTIR spectrometer will be broadened by the finite scanning range L. The Fourier transform of the interferogram, truncated at a distance L, is given by

$$I_0(k) = \int_0^L I(\delta) \cos k\delta \, d\delta. \tag{3.13}$$

Inserting Eq. (3.12) into Eq. (3.13) yields

$$I(k) = \int_0^L \cos k_0\delta \cos k\delta \, d\delta, \tag{3.14}$$

which can be re-written as

$$I(k) = \frac{1}{2}\int_0^L \{\cos[\delta(k - k_0)] + \cos[\delta(k + k_0)]\} \, d\delta \tag{3.15}$$

using the trigonometric identity $2\cos A \cos B = \cos(A - B) + \cos(A + B)$. Solving the integral yields

$$I(k) = \frac{L}{2}\left\{\frac{\sin[L(k-k_0)]}{L(k-k_0)} + \frac{\sin[L(k+k_0)]}{L(k+k_0)}\right\}. \tag{3.16}$$

Typically, $k_0L \gg 1$, so the second term can be disregarded. Therefore, Eq. (3.16) can be written as

$$I(k) \approx L\left\{\frac{\sin[L(k-k_0)]}{L(k-k_0)}\right\} = L \operatorname{sinc}[L(k - k_0)], \tag{3.17}$$

where we used the definition $\operatorname{sinc} x \equiv \frac{\sin x}{x}$. Figure 3.3 shows a plot of the sinc function characterized by a central maximum peak with secondary positive and negative peaks with diminishing amplitude farther from the center. The sinc function is zero at $x = \pm\pi$, or $k = k_0 \pm \frac{\pi}{L}$. Hence, the width of the central peak is

$$\Delta k \approx \frac{1}{L}, \tag{3.18}$$

showing that the resolution of the spectrometer is limited to the inverse of the scanning length L.

The large secondary oscillations on the sides of the central peak arise from the abrupt way in which the interferogram converges to zero at L. By causing the interferogram to converge slowly to zero at L, the secondary oscillations are greatly reduced and the function is highly localized. This numerical process of reducing the size of the secondary oscillations is called *apodization*. There are a number of apodization functions available, each with its own characteristic features. The most common apodization function is a linear function that goes to zero at $\delta = L$. This yields an apodized spectrum given by

$$I(k) \approx \operatorname{sinc}^2[L(k - k_0)]. \tag{3.19}$$

The plot of $\operatorname{sinc}^2 x$ function has considerably smaller secondary oscillations than the $\operatorname{sinc} x$ function, as shown in Fig. 3.3.

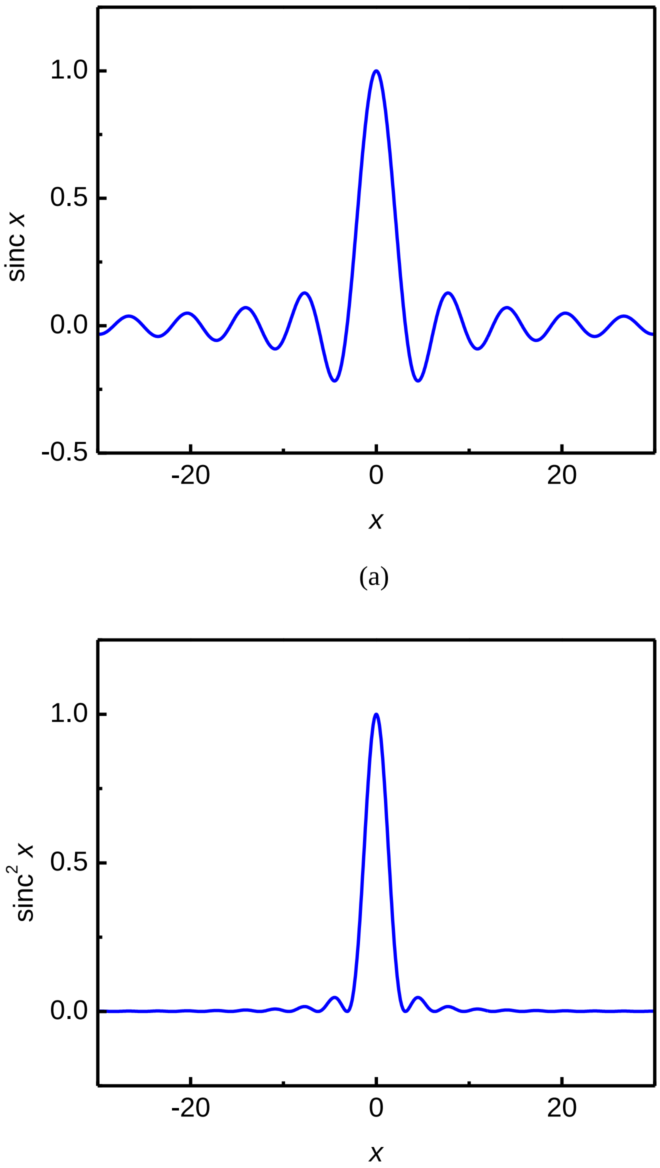

(a)

(b)

Figure 3.3: Plots of (a) sinc(x) and (b) sinc^2x.

3.1.3 Advantages of FTIR spectroscopy

Evidently, FTIR spectroscopy has a number of advantages that make it a more desirable technique over the "older" dispersive method for infrared spectral analysis.

i. A FTIR spectrometer samples all frequencies simultaneously with each mirror cycle, thus measurements are faster. This is referred to as Fellgett's advantage (Fellget, 1958). Consequently, the fast scans enable signal averaging of several scans in order to reduce the random measurement noise.

ii. The optical throughput is much higher, known as Jacquinot's advantage (Jacquinot, 1960), which results in much lower noise levels. This results from the fact that in a dispersive instrument, the entrance and exit slits of the monochromator control the amount of light that passes through it. In a FTIR spectrometer, the interferometer throughput is determined only by the diameter of the collimated beam that comes from the source.

iii. It is mechanically simple since the only continuously moving part is the scanning mirror in the interferometer. Therefore, mechanical breakdowns are relatively rare.

iv. It does not require an external calibration because it uses a He-Ne laser, as will be discussed in the next section, as an internal wavelength calibration standard. This provides better wavelength accuracy and is referred to as the Connes' advantage (Connes and Connes, 1966).

3.1.4 FTIR experimental apparatus

A Bomem DA8 FTIR spectrometer was used to obtain infrared spectra presented in this thesis (Fig. 3.4). It is a versatile spectrometer equipped with several optical ports, detectors modules and an array of interchangeable parts. The configuration consists of a globar IR source, which is a SiC rod heated to 1200°C, a KBr beamsplitter, and an MCT or InSb detector. The MCT (mercury cadmium telluride) detector is sensitive to IR light in the range of 450 to 5000 cm^{-1} while the InSb (indium antimonide) detector is much more sensitive in the range of 1800 to

7000 cm^{-1}. Both detectors must be cooled to liquid nitrogen temperatures. The beamsplitter is made out of potassium bromide (KBr) which is suitable for mid-IR studies in the range of 450 to 5000 cm^{-1}. The water-cooled globar source emits blackbody radiation that extends from ~200 to 4000 cm^{-1}. The spectrometer is also equipped with a Janis closed-cycle helium cryostat system that is used to maintain sample temperatures to as low as 7 K.

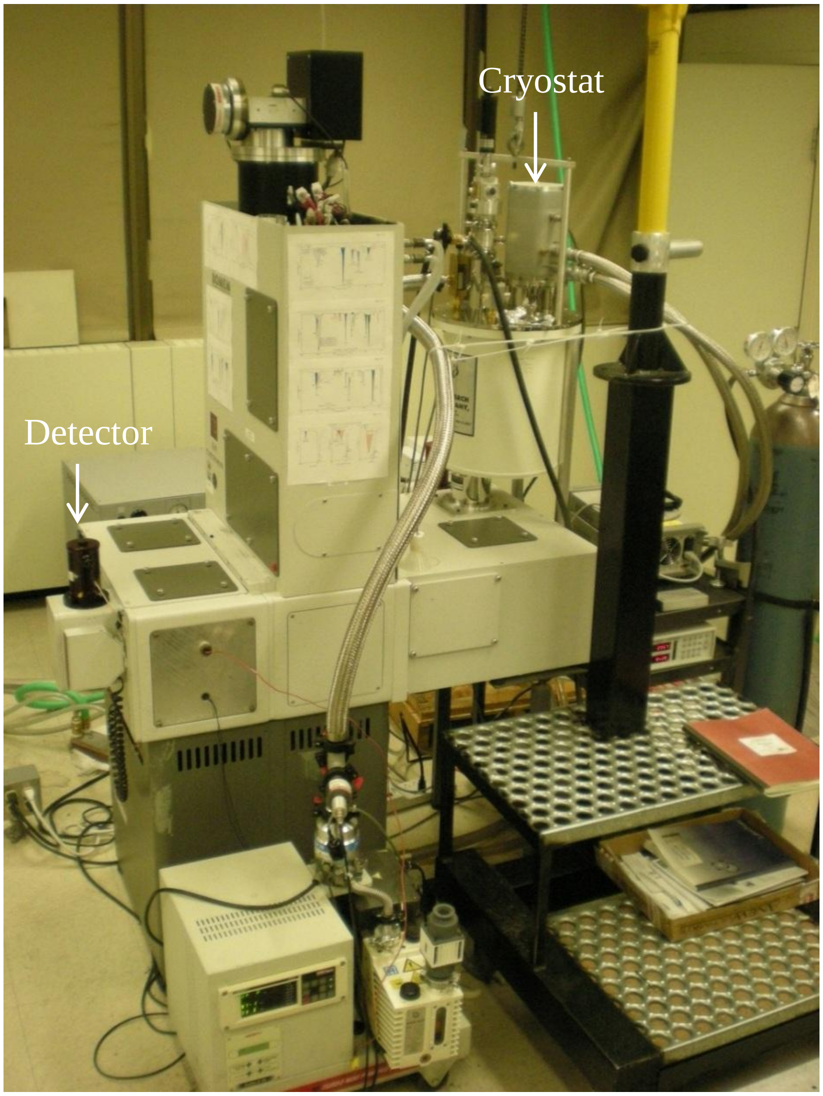

Figure 3.4: The Bomem DA8 FTIR spectrometer with a Janis closed-cycle helium cryostat attached to the backport of the spectrometer. An MCT detector is attached to front compartment for room temperature measurement.

To accurately measure the position of the scanning mirror, the spectrometer uses a single-mode He-Ne laser in which all but 632-nm wavelengths are suppressed (therefore a single-mode laser). The laser beam is sent to the interferometer and the interferogram it produces resembles a pure cosine oscillation. There are approximately 31600 cycles of laser cosine waves per cm of displacement of the scanning mirror. By monitoring the laser interferogram, high-precision tracking of the optical path difference δ is obtained.

In order to co-add successive scans and obtain the spectrum through the Fourier transform algorithm, it is necessary to be able to locate a positional reference that is highly repetitive from scan to scan. A zero path difference (ZPD) can be determined by the use of a white light source. Since the laser source is monochromatic, its interferogram cannot produce an unambiguous pattern at one particular scanning mirror position. The white light, emitted by an intense incandescent lamp, is a broadband source of light and its interferogram has a large maximum at ZPD where all wavelengths of light interfere constructively. The white light passes through the same optical elements as the light from the globar.

3.2 Photoluminescence (PL) spectroscopy

Photoluminescence (PL) provides a non-destructive technique for detection and identification of point defects in semiconductors. Bandgaps can be determined as well as the relative energetic position of sub-bandgap defect states. Sub-bandgap PL emission is related to electron–hole recombination mediated by a defect state. Photoluminescence excitation (PLE) is a technique where the spectrometer is set to detect emission of particular photon energy from the sample. The intensity of this emission is then recorded as a function of the excitation photon energy. It is a useful method to study the correlation between excitation (i.e., absorption) states and photoluminescence emissions. The PLE spectrum is expected to coincide with the absorption spectrum, with the difference that in the latter case several different transitions may contribute to and complicate the spectral analysis. Articles by P.J. Dean (1982) and G.D. Gilliland (1997) provide an excellent review on the basic uses of photoluminescence in semiconductor analysis.

Our PL measurements were performed using JY-Horiba FluoroLog-3 spectrofluorometer system (Fig. 3.5) equipped with double-grating excitation and emission monochromators with 1200 grooves/mm grating. Double-grating monochromators provide a significant increase in sensitivity, resolution and stray-light rejection. The excitation source is a 450-W xenon CW lamp. The sample compartment consists of a module that provides efficient throughput with an option of standard right-angle emission collection or front-face emission collection. The module also comes equipped with a Si diode reference detector to monitor and compensate for variations in the Xe lamp output. The detector is an R928P photomultiplier tube (PMT) which provides sensitive spectral characterization in the UV through the visible range. A system interface (SpectraAcq) transfers information to and from the host computer. An instrumental correction can be performed on all PL spectra, to correct for the wavelength-dependent PMT response, grating efficiencies, and the variation in output intensity from the lamp. Low temperature measurements were performed using a Janis closed-cycle helium cryostat.

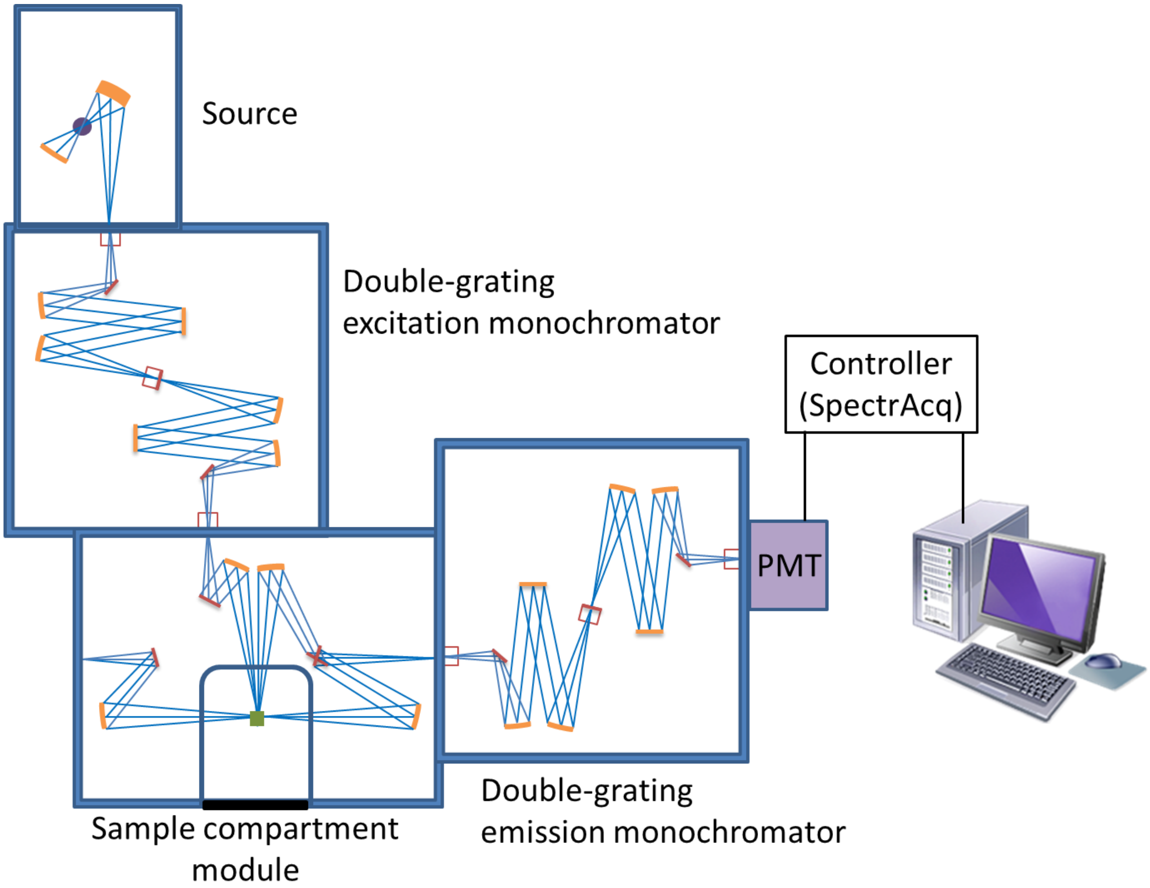

Figure 3.5: Basic components of the JY-Horiba FluoroLog-3 spectrofluorometer system.

3.3 Hall effect

Hall effect is a useful means of measuring the electrical properties of a semiconductor. Hall effect takes place when a potential difference (the Hall voltage) is produced across the sample through which a current is flowing and with applied magnetic field perpendicular to the sample. Carrier type, concentration and mobility are obtained through Hall effect measurements.

3.3.1 Derivation of Hall voltage

Consider an electric current I flowing through the sample in the presence of a magnetic field $\vec{B}$ as shown in Fig. 3.6. The magnetic field exerts a transverse force on the moving charges that causes them to move to one side of the sample. The magnitude of the magnetic force is given by

$$F_B = ev_dB, \tag{3.19}$$

where e is the electron charge, v_d is the drift velocity of the charge, and B is the magnitude of the applied magnetic field. The current in terms of drift velocity is given by $I = neAv_d$, which gives

$$v_d = \frac{I}{neA}, \tag{3.20}$$

where n is the density of the charge carriers and A is the cross-section area of the sample. Inserting this into Eq. (3.19) yields

$$F_B = \frac{IB}{nA}, \qquad (3.21).$$

The buildup of charge on the sides of the sample will balance this effect of magnetic force, producing a measurable voltage V_H between the sides of the sample of width y. Thus, at equilibrium,

$$F_B = F_E = \frac{eV_H}{y}. \tag{3.22}$$

Noting the sample cross-section area $A = yd$ where d is the sample thickness, substituting Eq. (3.21) into Eq. (3.22) yields the Hall voltage:

$$V_H = \frac{IB}{ned}. \tag{3.23}$$

Since the current, the magnetic field, and the Hall voltage are experimentally determined parameters, Eq. (3.23) enables the determination of the charge carrier density of the sample. The equation also applies for positively charged carriers (holes) since electrons and holes have the same magnitude of charge.

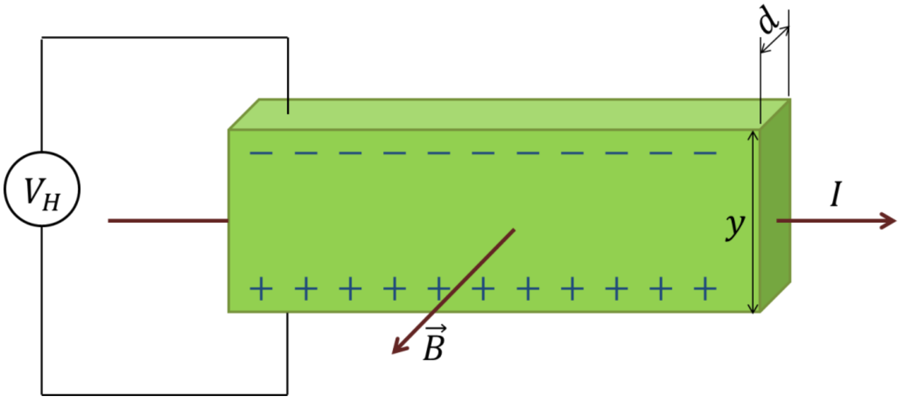

Figure 3.6: Schematic diagram of Hall effect.

3.3.2 Mobility

Mobility is one of the important properties of a semiconductor which characterizes how fast a charge carrier can move through a semiconductor under applied electric field. It is given by the magnitude of the drift velocity of the charge carrier per unit electric field:

$$\mu = \frac{v_d}{E}, \tag{3.24}$$

which is defined to be positive for both electrons and holes, even though their drift velocities are opposite in a given electric field.

A simple relation exists between mobility and electrical conductivity σ. For an *n*-type semiconductor in which the conductivity is due entirely to electrons, the conductivity is given by

$$\sigma = ne\mu_e. \tag{3.25}$$

In a *p*-type semiconductor, the conductivity is due to holes, but the equation is essentially the same. If we let *p* be the hole density and μ_h be the hole mobility, the conductivity is given by

$$\sigma = pe\mu_h. \tag{3.26}$$

The total conductivity of a semiconductor with both electrons and holes will be the sum of the contributions of both charge carriers:

$$\sigma = ne\mu_e + pe\mu_h. \tag{3.27}$$

Note that the electrical resistivity ρ is defined as the reciprocal of the conductivity:

$$\rho = \frac{1}{\sigma}. \tag{3.28}$$

3.3.3 Van der Pauw method

The van der Pauw method is a four-probe technique that is widely used for measuring resistivity of a sample along with carrier density and mobility. The advantage of this technique is its usefulness in measuring arbitrarily shaped samples. In this technique, four ohmic contacts are placed on the periphery of the sample (Fig. 3.7). If a current I_{12} is applied through point 1 and out of point 2 and the potential difference between points 4 and 3 is measured, the sheet resistance is given by

$$R_{12,43} = \frac{V_{43}}{I_{12}}. \tag{3.29}$$

Similarly, if current I_{23} is passed through point 2 and out of point 3 and the potential difference is measured between points 1 and 4, the resistance is

$$R_{23,41} = \frac{V_{41}}{I_{23}}. \tag{3.30}$$

Van der Pauw (1958) showed that the resistivity is determined by

$$e^{-\frac{\pi d}{\rho}R_{12,43}} + e^{-\frac{\pi d}{\rho}R_{23,41}} = 1, \tag{3.31}$$

which can written as

$$\rho = \frac{\pi d}{ln2}\frac{R_{12,43}+R_{23,41}}{2}f, \tag{3.32}$$

where d the thickness of the sample and the form factor is f depends on the ratio $\frac{R_{12,43}}{R_{23,41}}$. For a symmetric sample, the resistivity is given by

$$\rho = \frac{\pi d}{ln2}R. \tag{3.33}$$

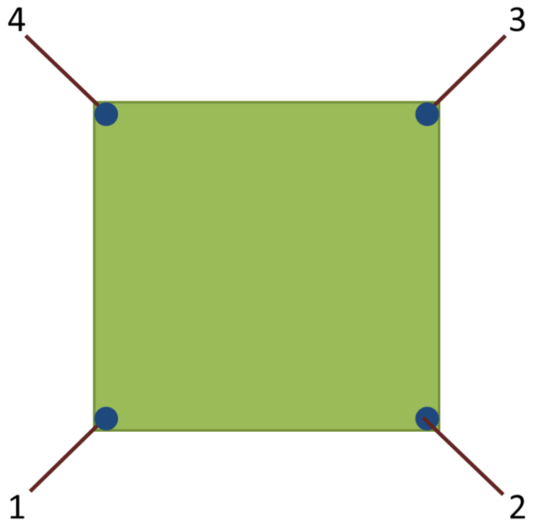

Figure 3.7: Ohmic contacts for van der Pauw method

3.3.4 Hall effect experimental apparatus

Measurements were carried out on a Hall effect system with the van der Pauw technique from MMR Technologies, Inc. (Fig. 3.8) with a temperature operating range from 80 K to 700 K. The system is equipped with a Hall dewar, a K-20 programmable temperature controller, and an H-20 Hall-van der Pauw controller. The Hall dewar is a vacuum tight chamber. The sample is mounted onto a cold stage with a thermocouple and a heating wire attached underneath. Low temperatures are achieved through the Joule-Thomson effect in which high-pressure nitrogen gas is used and allowed to expand adiabatically through capillary channels and undergo successive pressure drops, resulting in overall temperature drop. The desired temperature is maintained by the K-20 controller while the applied current and voltage between probes are controlled by the H-20 interface.

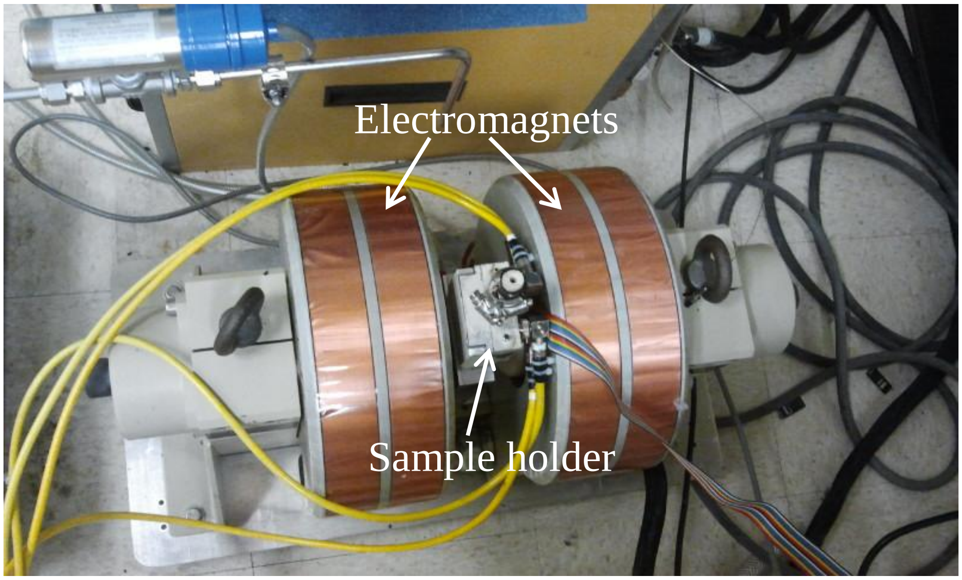

Figure 3.8: The MMR Technologies Hall System.

3.4 Chemical vapor transport method for crystal growth

By growing our ZnO crystals, we are able to study and control defects systematically. Chemical vapor transport (CVT) is a simple and suitable technique for growing bulk ZnO crystals (Look et al., 1998; Ntep et al., 1999; Mycielski et al., 2004; Jokela and McCluskey, 2007). ZnO has low vapor pressure; hence it is difficult to grow from melt. The CVT process is based on chemical transport reactions between the source materials and a transport agent that occur in a closed ampoule held at a temperature gradient. The source materials consist of the elements that compose the final crystal and dopants of interest. For our ZnO crystal growth, we use graphite as transport agent. Graphite has been found to be an effective transport agent in growing quality bulk ZnO crystals (Mycielski et al., 2004; Jokela and McCluskey, 2007). The following equations describe the process (Jokela and McCluskey, 2010):

$$\mathrm{ZnO} + \mathrm{C} \rightarrow \mathrm{Zn} + \mathrm{CO},$$

$$\mathrm{ZnO + CO \leftrightarrow Zn + CO_2}. \tag{3.34}$$

We used ZnO micro-particles and graphite powder obtained from Sigma-Aldrich. Both 4N- and 5N-purity ZnO and graphite powder were used. The ZnO powder was prepared into aggregate masses by mixing it with HPLC grade water to make a paste and then boiling away the water. The use of ZnO aggregate and graphite powder produce crystals of larger size (Jokela and McCluskey, 2007). The ZnO aggregate and graphite powder were loaded into a fused silica ampoule of about 15 cm long and an inner diameter of 1.7 cm. An ampoule cap, where the crystal deposition is to occur, was inserted 10 cm from the source end which contains the ZnO and the graphite. The ampoule was evacuated and backfilled with ½ atm Ar or NH_3 and then was sealed using hydrogen-oxygen torch. Ammonia was used as an ambient in order to introduce nitrogen into the crystal growth. The ampoule was placed in a three-zone horizontal furnace (Fig. 3.9) and was programmed to maintain a temperature of 1000°C at the source end and 880°C at the deposition end.

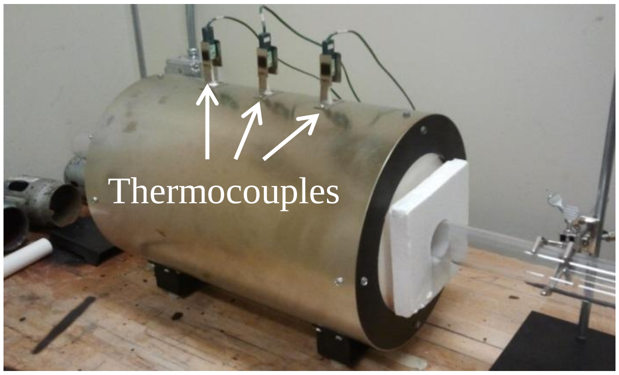

Figure 3.9: The three-zone horizontal tube furnace.

Seeded CVT growth has been performed by placing a seed crystal at the deposition end (Jokela, Tarun, and McCluskey, 2009). The seed single crystals were obtained from Cermet, Inc.

and were cut to 5 x 5 x 0.5 mm. The seed crystal was attached to the end of the ampoule by melting a small piece of copper between the seed and the ampoule wall. A schematic of the seeded CVT growth system is shown in Fig. 3.10. A sample of about 2 mm thickness is obtained after a growth duration of 72 hours.

Figure 3.10: A schematic diagram of the seeded CVT growth system.

3.5 Hydrogen annealing

Annealing in hydrogen at elevated temperature is an excellent method of introducing hydrogen into bulk semiconductors. This method of hydrogenation has been performed in ZnO at 700°C (Jokela and McCluskey, 2005).

For our study of the structure and stability of hydrogen defects in $SrTiO_3$, hydrogen-annealing experiments were performed in the horizontal tube furnace. A fused silica ampoule was used to hold the sample, and was evacuated and backfilled with H_2 gas. The ampoule was then sealed using a hydrogen-oxygen torch. The sealed ampoule was loaded into the furnace for annealing. After the annealing was completed, the ampoule was rapidly quenched to room temperature by dropping it in water.

CHAPTER 4 NITROGEN ACCEPTORS IN ZINC OXIDE

4.1 Introduction

One of the outstanding issues in ZnO is *p*-type doping, a quest that awaits a breakthrough. *P*-type doping is essential because it enables the development of practical devices, including blue/UV light-emitting diodes or lasers, and ultimately the realization of highly efficient and less expensive solid-state lighting devices. However, reports of *p*-type doping in ZnO have been controversial and ambiguous, in particular the feasibility of nitrogen to act as an acceptor (or *p*-type dopant). As discussed in Section 1.3.5, experimental and theoretical investigations suggested that nitrogen substituting on a host oxygen site (N_O) has a shallow acceptor level in ZnO, and thus may lead to *p*-type conductivity. However, recent calculations (Lyons et al., 2009) have shown that N_O forms a deep acceptor energy level in ZnO. In the following discussion, I present experimental evidence that nitrogen is a deep acceptor, contradicting hundreds of prior reports.

4.2 Nitrogen-doped ZnO

Bulk single-crystal samples were grown via a seeded chemical vapor transport technique in an ammonia ambient, which provided the nitrogen, as well as hydrogen, dopants (Sec. 3.4). Samples have reddish appearance and are typically 1.8 – 2.0 mm thick (Figure 4.1). As-grown, they are *n*-type with carrier densities ranging from 2 to 8 x 10^{17} cm^{-3}.

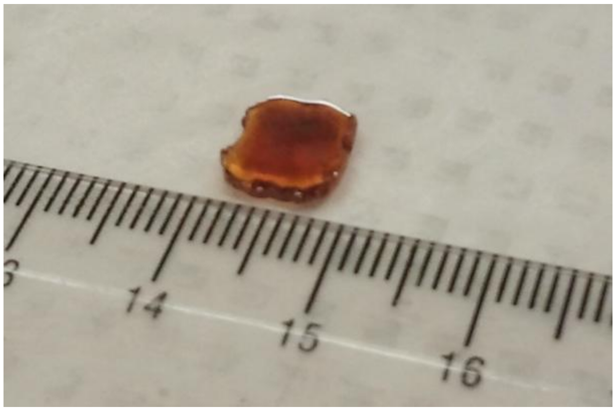

Figure 4.1: N-doped ZnO grown by seeded chemical vapor transport

4.3 Infrared spectroscopy of N-doped ZnO

An IR absorption peak at 3148 cm^{-1} was observed at room temperature (3151 cm^{-1} at 10 K). This peak has been unambiguously assigned to a N-H complex (Jokela and McCluskey, 2010). Thermal anneals were carried out in an evacuated silica ampoule filled with 0.5 atm oxygen before sealing. Annealing at 675^{o}C drives out hydrogen donors (Shi et al., 2004) while the N-H bond remains intact. To activate nitrogen acceptors, the sample was annealed at 775^{o}C, causing the N-H pairs to dissociate, leading to a reduction in the N-H absorption peak intensity (Fig. 4.2). The decrease in free carrier absorption after the 775^{o}C anneal indicates that the nitrogen acceptors compensate a fraction of the donors. This decrease in *n*-type conductivity was previously observed by Hall-effect measurements on similarly grown samples annealed in O_2 (Jokela and McCluskey, 2010).

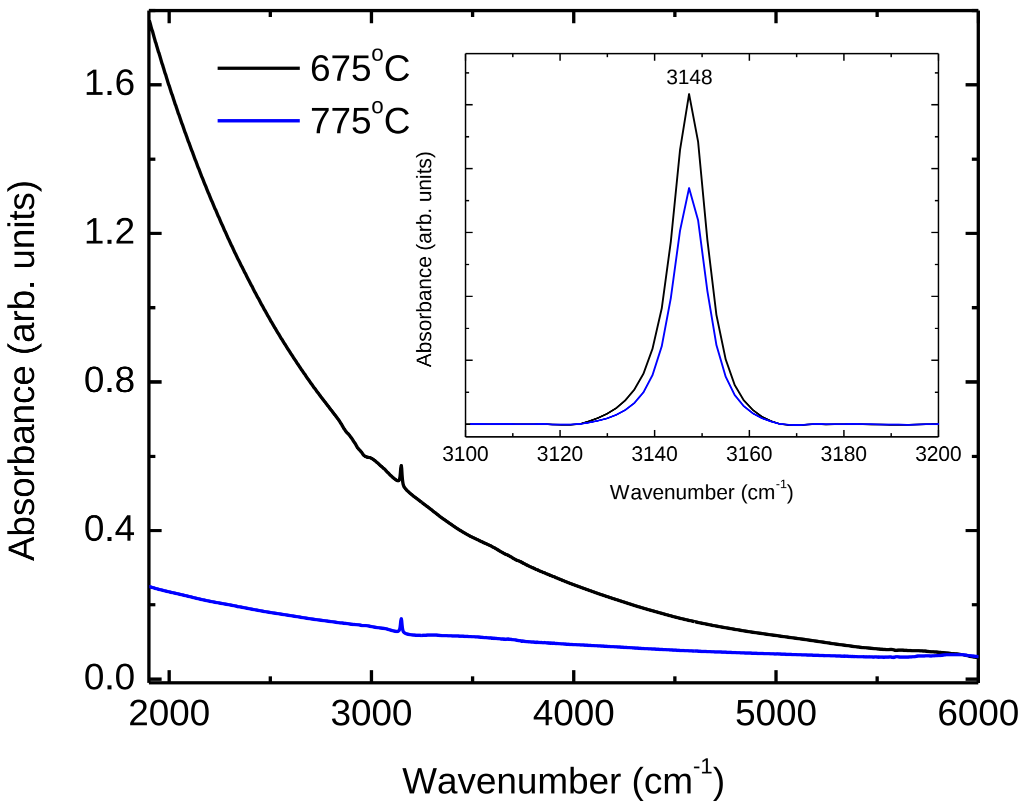

Figure 4.2: Room-temperature IR absorption of N-doped ZnO after annealing in O_2 at 675°C and 775°C. The reduction in background free-carrier absorption corresponds to the dissociation of a fraction of the N-H complexes. Inset: Baseline-corrected spectra of N-H absorption peaks.

4.3 Photoluminescence spectra

To investigate the N-related defect levels in our *n*-type samples doped with nitrogen acceptors (N_O^-), we took photoluminescence (PL) spectra with sub-band gap excitation. Monochromatic light excites the N_O^- electron into the conduction band. When the electron is recaptured by a neutral nitrogen acceptor, a photon is emitted.

Figure 4.3 shows PL emission spectra at an excitation wavelength of 490 nm (2.53 eV) for the sample annealed in O_2 at (a) 675 ^{o}C and subsequently at (b) 775 ^{o}C. A broad "red" emission band is detected at ~730 nm (1.70 eV). To further increase the concentration of N acceptors, the sample was subsequently annealed at 775^{o}C for 8.5 h. The sample shows a decrease in N-H peak intensity and corresponding increase in the red emission band (Fig. 4.3c).

A photoluminescence excitation (PLE) spectrum (Fig. 4.4) was obtained by monitoring the red emission band (at 730 nm) as a function of excitation wavelength. The PLE spectrum gives the absorption profile for the red emission. An excitation onset of ~2.2 eV was observed. The main features of the PLE spectrum – an excitation onset followed by a monotonic increase with photon energy – are similar to PLE spectra observed for deep native acceptors in ZnSe (Iota and Weinstein, 1999). The PLE spectrum concurs with the observed optical transmission spectrum of the sample. Absorption of photon energies > 2.2 eV gives the sample a reddish appearance. A similar absorption profile has been correlated with nitrogen acceptors detected by electron paramagnetic resonance (Garces, et al., 2002; Carlos and Glaser, 2001).

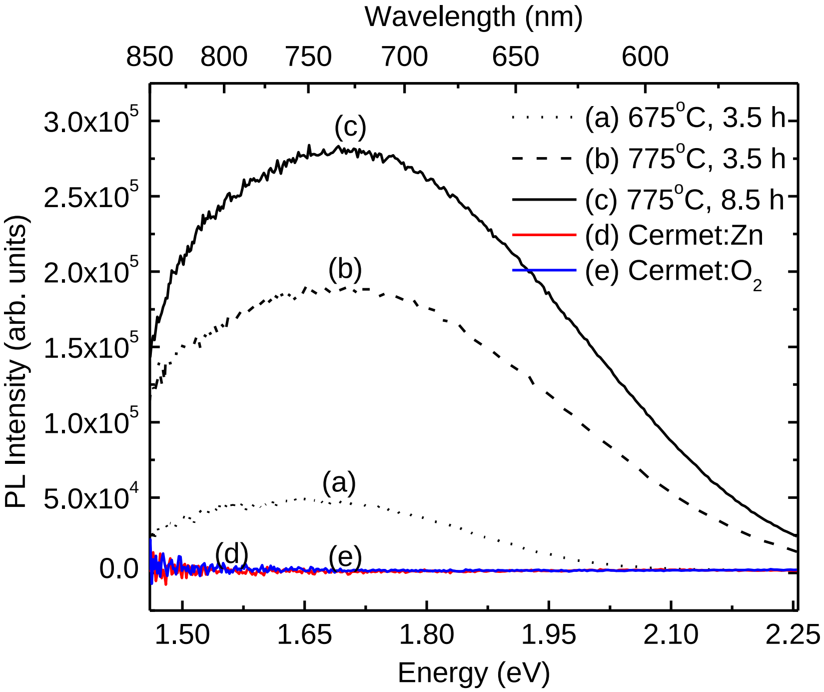

Figure 4.3: Room-temperature PL emission spectra (excitation wavelength: 490 nm) for N-doped ZnO after annealing in O_2 at (a) 675°C for 3.5 h, and subsequently at (b) 775 °C for 3.5 h and (c) 775 °C for 8.5 h. Also shown are the emission spectra of Cermet samples annealed in (d) Zn vapor and in (e) O_2.

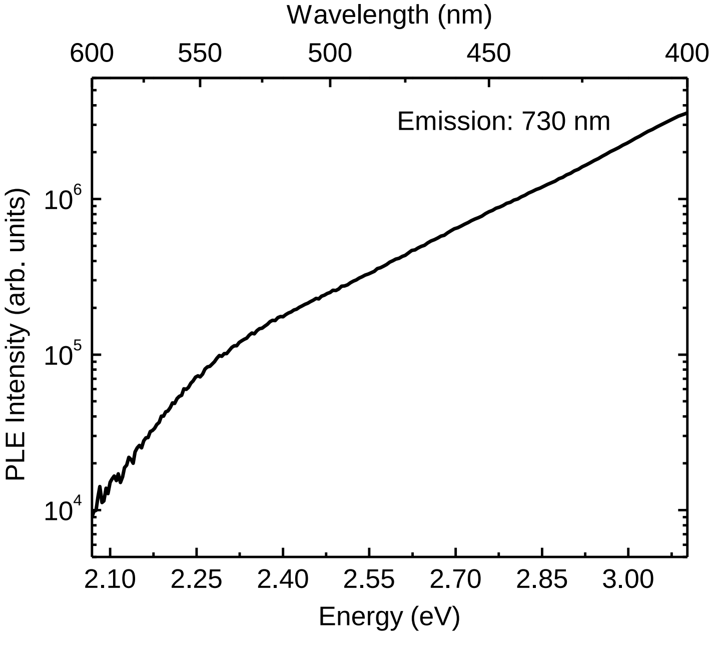

Figure 4.4: Room temperature PLE spectrum for the red emission band at 730 nm wavelength, from the N-doped ZnO sample.

4.4. Configuration coordinate diagram

When an electron absorbs a photon and makes a transition to another state, the positions of the nuclei do not change in the process [Franck-Condon principle (McHale, 1999)]. This process is illustrated in a configuration coordinate diagram (Pankove, 1971) which presents the energy of the ground state and of the first excited state of the impurity atom as a function of position. Optical transitions are "vertical", leaving the lattice configuration unchanged. Once the transition occurs, the system is likely to relax to a new minimum energy lattice configuration, before recombination occurs. The amount of energy loss during relaxation is called the Franck-Condon shift (McCluskey and Haller, 2012).

Recent theoretical work by Lyons, Van de Walle, and Janotti (2009) show that N_O^- is a deep acceptor, with an acceptor level of 1.3 eV above the valence band maximum. The calculated configuration coordinate diagram for the nitrogen acceptor atom (Fig. 4.5) estimated an optical absorption and emission energies of 2.4 eV and 1.7 eV, respectively. The Stokes shift of 2.4 - 1.7 = 0.7 eV is due to large lattice relaxation of the deep acceptor.

We can clearly see that the red PL emission spectra (Fig. 4.3) obtained from our N-doped sample with excitation wavelength 490 nm (2.5 eV) are in agreement with the calculated CC diagram for the deep acceptor model (Fig. 4.5). Furthermore, the excitation onset of ~2.2 eV exhibited in the PLE spectrum of our sample (Fig. 4.4) is also consistent with the nitrogen deep acceptor model. Hence, the PL and PLE spectra of our N-doped sample provide experimental support of the N_O deep acceptor model.

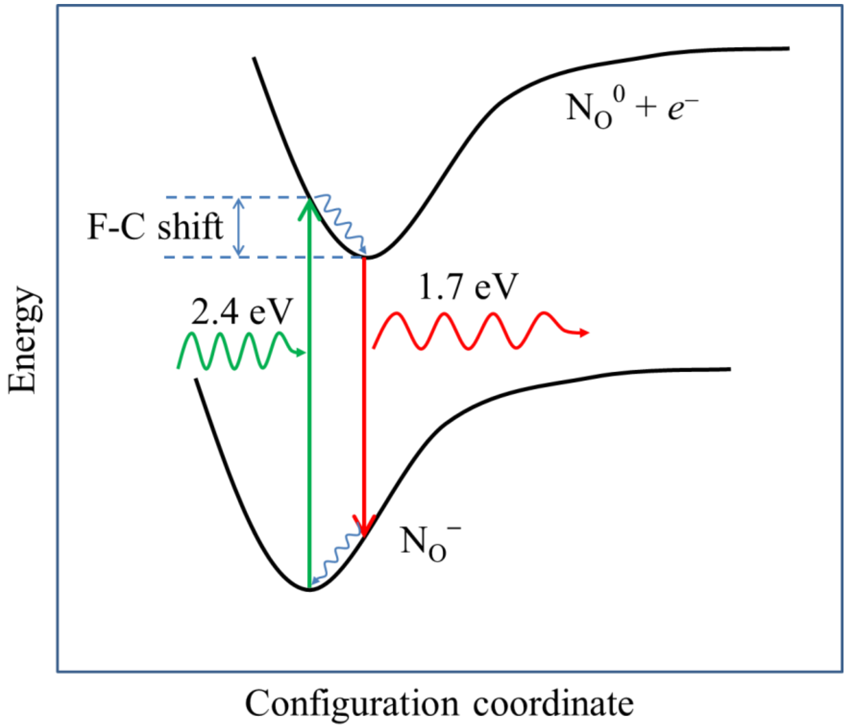

Figure 4.5: Configuration coordinate diagram for the nitrogen deep acceptor model (Lyons, Janotti, and Van de Walle, 2009)

4.5 Low-temperature luminescence

As the temperature is lowered, the red luminescence increases in intensity. As shown in Fig. 4.6, the peak also exhibits a red-shift. The center of the peak shifts from the red (1.7 eV) to the near-IR (1.5 eV) as the temperature decreases from 300 to 10 K. Several factors may contribute to this shift. First, as the temperature is lowered, the transition goes from a band-to-acceptor to a donor-acceptor, the latter having a lower energy. Second, the thermal change in population of vibrational states may affect the PL energies.

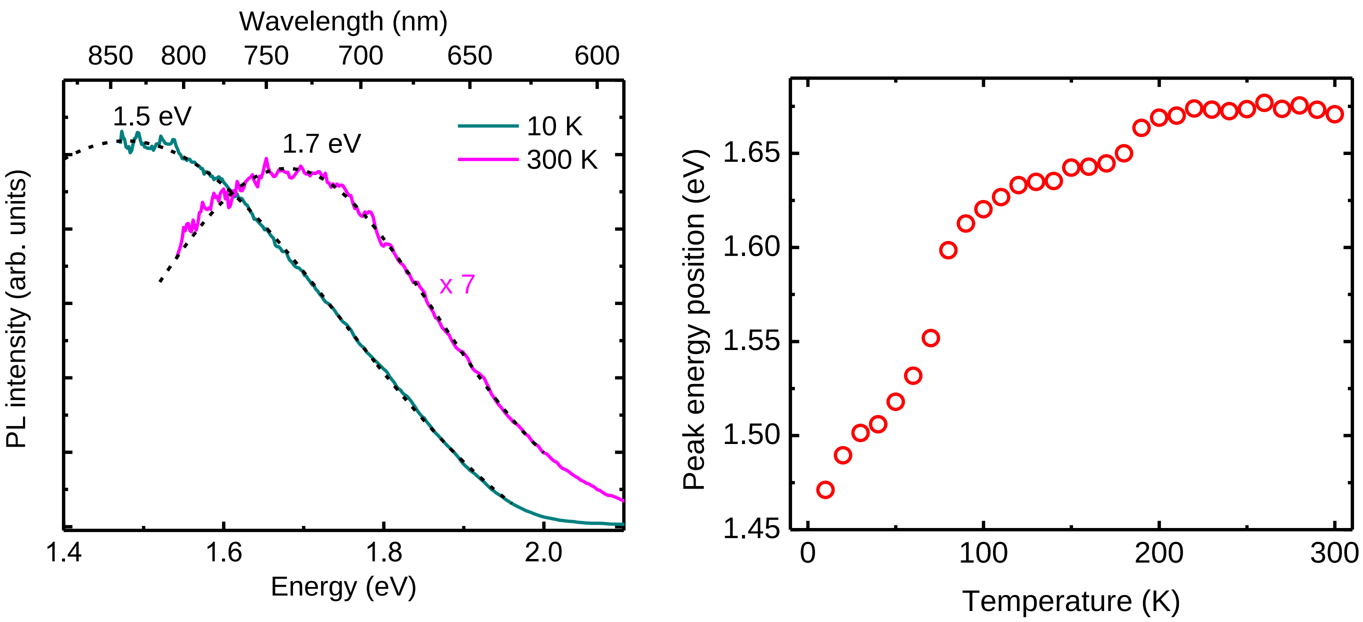

Figure 4.6: (a) PL spectra of N-doped sample at 10 and 300 K. (b) Temperature dependence of the peak energy position of the “red” PL as a function of temperature.

4.6 Persistent photoconductivity

Infrared absorption spectra were obtained at 10 K while the sample was exposed to 475 nm (2.61 eV) laser light provided by a diode pumped solid state laser (peak power < 500 mW). An increase in free-carrier absorption was observed (Figure 4.7). This provides additional evidence of a deep level, since a photon energy of 2.61 eV cannot cause a transition of an electron from a *shallow* acceptor level to the conduction band in ZnO, which has a band gap of 3.4 eV. The photoconductivity persists for several hours when the sample is left in the dark. The observation of free carrier absorption is consistent with the optical excitation of an electron from the N_O^- deep acceptor to the conduction band. The persistence of the free carriers following illumination is also consistent with large lattice relaxation of a deep-level impurity (Lang and Logan, 1977).

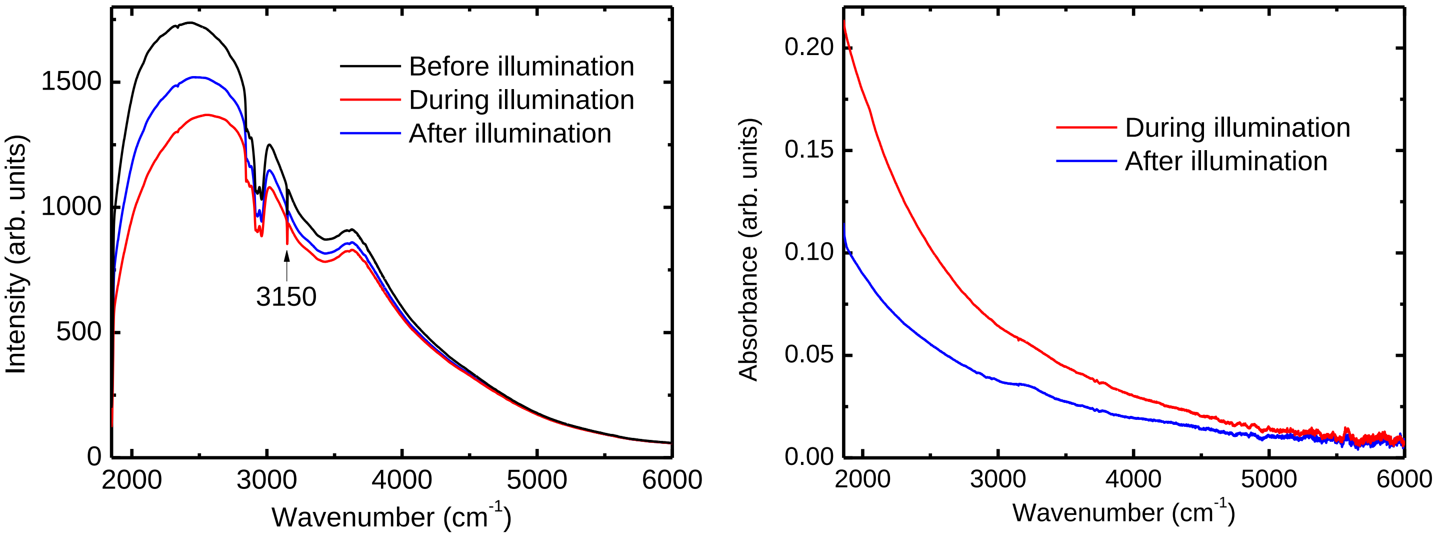

(a) (b)

Figure 4.7: (a) IR raw spectra obtained at 10 K before, during and after 475-nm light exposure. (b) The absorbance spectra during light exposure and in the dark after exposure, using the spectrum before light exposure as a reference. The increase in absorption is attributed to enhanced free-carrier absorption due to illumination.

4.7 Hydrogen passivation of N acceptors

To further test the deep-acceptor model, a N-doped sample was annealed in hydrogen at 700^{o}C. An increase in free carrier density and N-H peak intensity was observed after the hydrogen anneal, indicating passivation of N acceptors by hydrogen. The PL emission shows a dramatic disappearance of the red emission band after the hydrogen anneal (Fig. 4.8), manifestly consistent with hydrogen passivation of deep N acceptors.

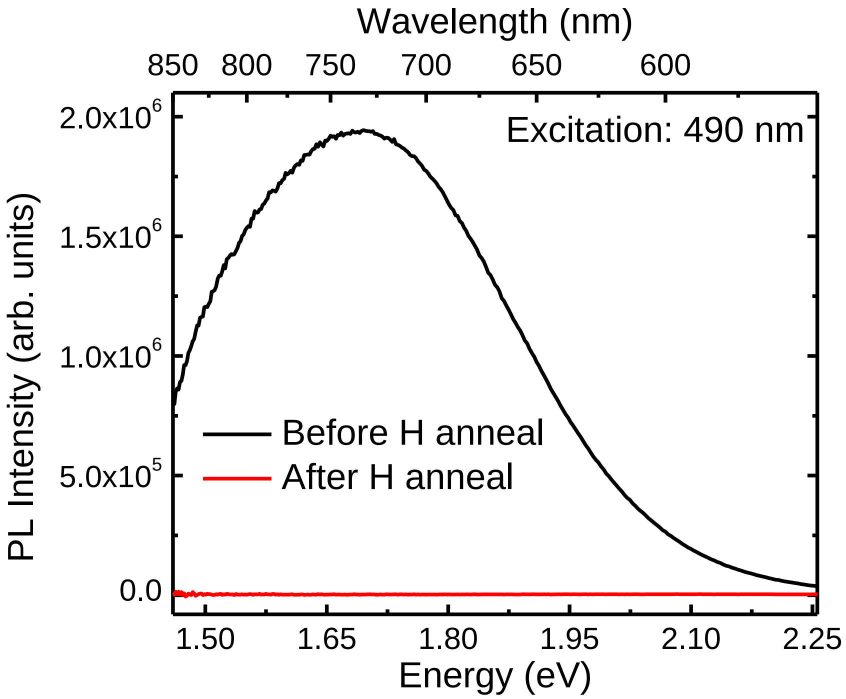

Figure 4.8: PL emission of the sample before and after hydrogen annealing. The disappearance of the “red” PL emission is attributed to hydrogen passivation of deep nitrogen acceptors.

4.8 Annealing in oxygen and in zinc

Native defects are often invoked to account for the observed optical and electrical properties of ZnO (Halliburton et al., 2005). To verify that the red emission that we observe and associate with N acceptors is neither due to oxygen vacancies nor zinc vacancies, nominally undoped single-crystal ZnO samples from Cermet, Inc. were annealed in zinc vapor and oxygen, respectively. The thermal anneals were carried out at 1100°C in Zn vapor for 30 min and at 800°C in O_2 for 15 hrs, respectively. The zinc-annealed sample turned red, in agreement with prior work that attributed the red color to oxygen vacancies (Halliburton et al., 2005; Selim et al., 2007). The oxygen-annealed sample, on the other hand, did not show any color change, parallel to previous observation (Weber et al., 2010). Neither of the samples exhibits the red PL emission band (Figs. 4.3d and 4.3e). When excited by above-band-gap light, the Cermet samples and our N-doped samples all exhibit the well-known “green luminescence” band centered at ~2.5 eV (McCluskey and Jokela, 2009). The green PL emission increased upon annealing in zinc or oxygen vapor. Green luminescence has been attributed to various defects, including zinc vacancy, oxygen vacancy, and copper impurity (McCluskey and Jokela, 2009). The observation that *red* luminescence occurs only in N-doped samples provides additional support for our assignment.

4.9 Nominally undoped ZnO

To further verify that the red luminescence is actually due to nitrogen, we compared spectra from samples grown in ammonia and argon. These are referred to as N-doped and undoped ZnO, respectively. For the N-doped sample, the N-H peak decreases as the sample is annealed in oxygen (Fig. 4.9). This is accompanied by a corresponding increase in the red luminescence. Spectra for the undoped sample were multiplied by 10 for clarity. From Fig. 4.9, we can see that the N-H peak and red luminescence are both an order of magnitude weaker than for the deliberately N-doped sample. (Unintentional N doping probably came from contamination during the growth). This strong effect provides further evidence that the red luminescence is definitely correlated with nitrogen acceptors.

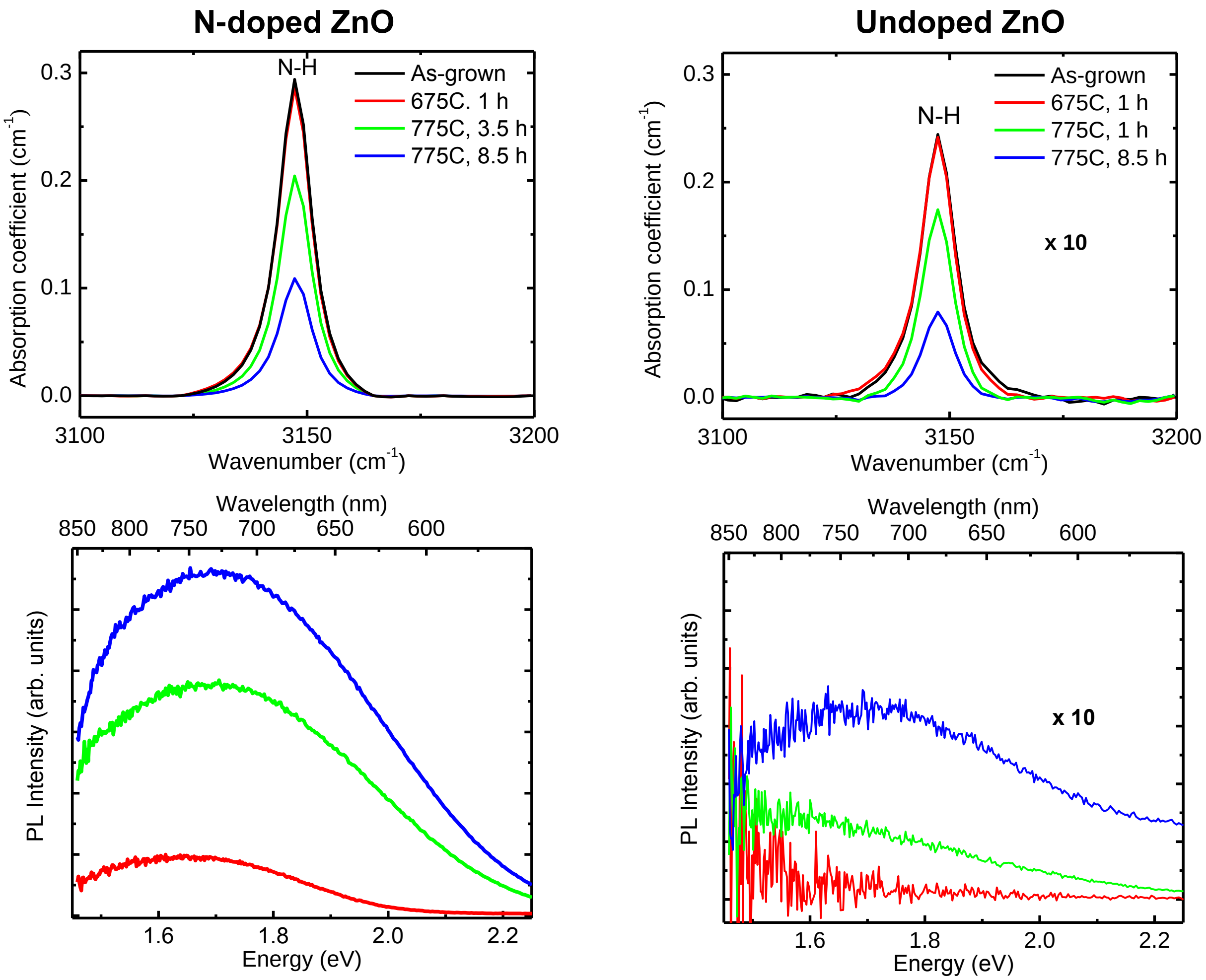

Figure 4.9: Room-temperature spectra for N-doped and nominally undoped ZnO. Top: IR absorption, showing a peak due to N-H pairs. Bottom: Red luminescence, attributed to N acceptors.

4.10 Near-band-edge PL

Near-band-edge PL measurements were performed on our samples at University of Idaho in collaboration with Prof. L. Bergman and Jesse Huso. The spectra were obtained with a He-Cd Kimmon laser (wavelength ~ 325 nm) and a JY-Horiba micro-PL system consisting of a high-resolution triple monochromator and a UV microscope that can focus to a 1-μm diameter spot size. The low temperature measurements, using this setup, were carried out at 80 K in an INSTEC HCS621V UV-compatible microcell.

The near-band-edge PL spectra are shown in Fig. 4.10. For the N-doped sample (annealed at 775°C), peaks corresponding to the free exciton (FX) at 3.378 eV, donor-bound exciton (D,X) at 3.363 eV, and phonon replicas (1LO, 2LO) are clearly resolved. These peaks are also seen in the undoped sample, although they are broader. The spectrum for the N-doped sample contains a peak at 3.267 eV, which is absent in the undoped sample. This peak has phonon replicas near 3.194 and 3.124 eV. We tentatively ascribe this new peak to a nitrogen acceptor-bound exciton (A,X). Given this assignment, the exciton binding energy is 0.1 eV. This value is ~1/10 that of the acceptor ionization energy, which follows Haynes' rule (Hayne, 1960) for exciton binding energies in semiconductors. A PL peak with similar zero-phonon energy at 3.235 eV was previously attributed to nitrogen acceptors (Zeuner et al., 2002). Further work will be required to provide a definitive assignment.

We also note the increase in PL intensity and the decrease in peak linewidths with annealing, indicating improved crystal quality. In particular, the 3.267 eV peak was not observed in the as-grown ZnO:N sample but is observed in the sample annealed at 775°C. This correlation, similar to that found for the red luminescence, is consistent with the dissociation of N-H pairs.

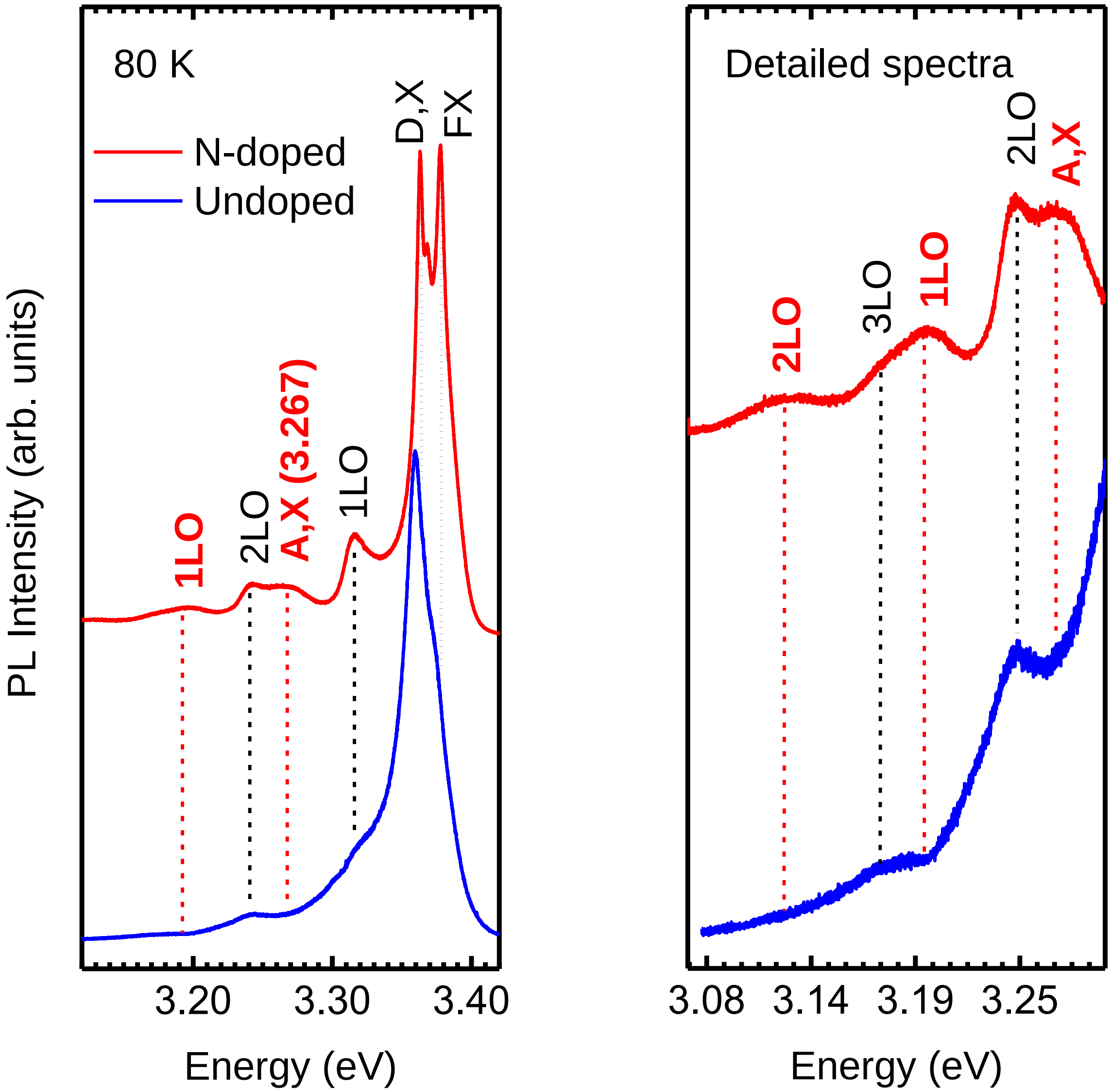

Figure 4.10: PL spectra near the band edge. Spectra taken by J. Huso.

4.11 Electron paramagnetic resonance spectra

To further confirm the presence of nitrogen acceptors in our sample, an electron paramagnetic resonance (EPR) spectroscopy was performed on our N-doped sample by Dr. E. Glaser of Naval Research Laboratory using a Bruker 9.5-GHz spectrometer configured with a liquid-helium flow cryostat for temperature control. Nitrogen acceptors have been observed and unambiguously identified with EPR (Carlos et al., 2001; Garces et al., 2002). Figure 4.11 shows the EPR spectrum of our N-doped sample obtained at 5 K for two orientations of the magnetic field. The spectrum in the dark (Fig. 4.11a) shows a strong signal due to residual shallow donors and indicates that the sample is *n*-type. The five-line (anisotropic) signal also observed in the dark is associated with the negative charge state of a N_2 defect. Because of the large concentration of shallow donors in the sample, the nitrogen acceptors are initially in the nonparamagnetic singly ionized state N^-. Exposure to light temporarily converts a portion of the N^- acceptors to the paramagnetic neutral state N^0. Under photo-excitation (Fig. 4.11b), a strong three-line (anisotropic) signal is observed and is associated with the neutral N (deep) acceptor state (Garces et al., 2003). The nitrogen EPR spectrum is characterized by $g_{\|} = 1.9953$ and $g_{\perp} = 1.9633$. The well-resolved three-line hyperfine pattern is due to an interaction with one nitrogen nucleus (^{14}N, I=1, ~100% abundant).

When the methods of PL and EPR are merged, a technique called optically detected magnetic resonance (ODMR) can be performed to determine the origin of a defect (McCluskey and Haller, 2012; Glaser et al., 2002). This technique is based on the fact that many optical transitions are spin-dependent. ODMR relates the magnetic information to particular luminescence bands and assists their identification. ODMR on our red PL band is currently investigated by Dr. Glaser which may establish another strong support of nitrogen deep acceptor in ZnO.

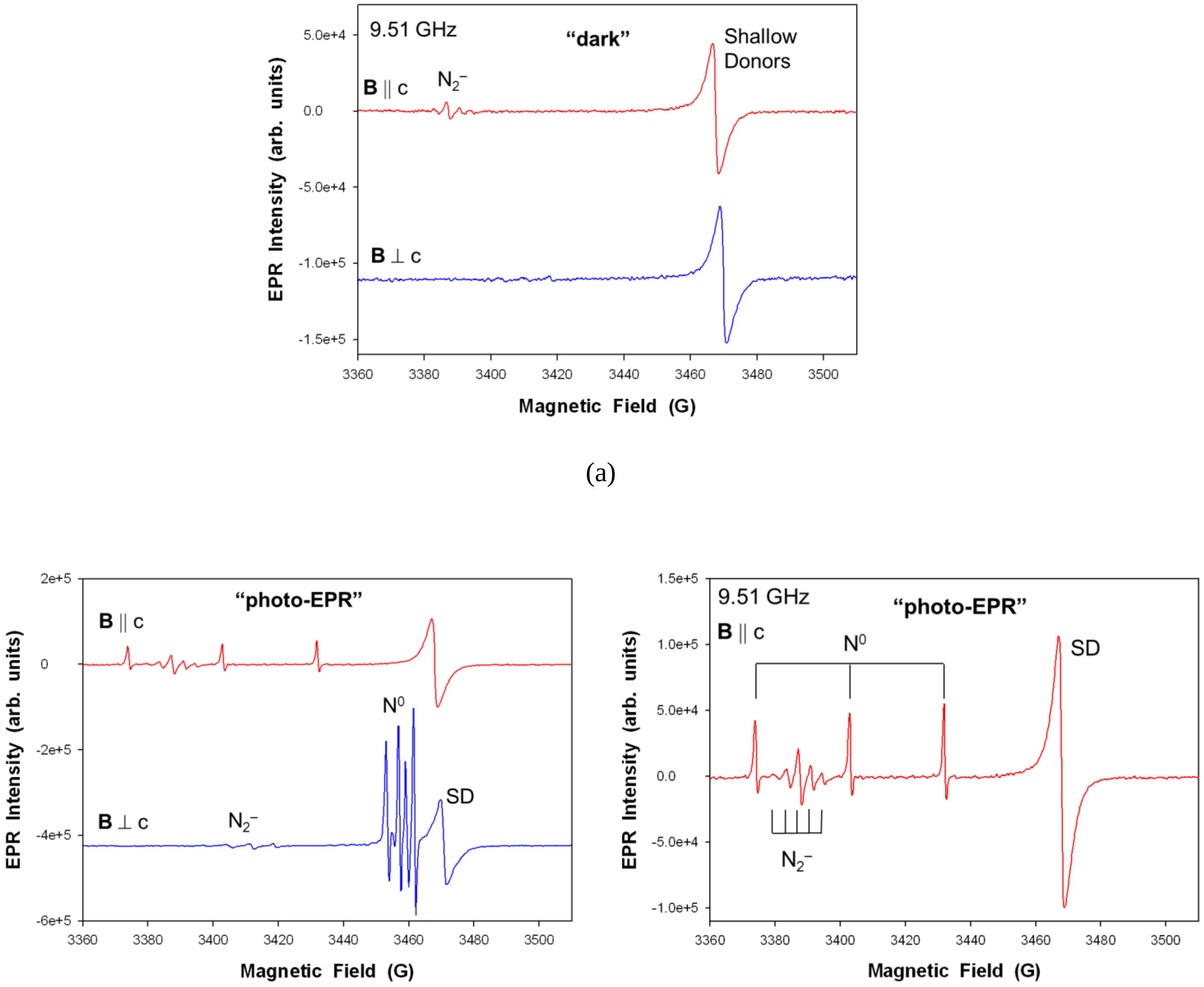

(a)

(b)

Figure 4.11: EPR spectra taken at 5 K from N-doped ZnO (a) in the dark, and (b) under photo-excitation where the characteristic three-line hyperfine spectrum of neutral nitrogen acceptor is observed. Spectra taken by Dr. E. Glaser.

4.12 Conclusions

We have shown experimental evidence that nitrogen is deep acceptor in ZnO. N-doped ZnO samples exhibit a broad red PL emission band, peaking near 1.7 eV, with an excitation onset of ~2.2 eV, in good agreement with the deep-acceptor model (Lyons, Janotti and Van de Walle, 2009). By comparing the PL spectra for the undoped and N-doped samples, we have confirmed the red luminescence is correlated with nitrogen acceptors. The intensity of this red PL band increases with the concentration of activated nitrogen acceptors. Observation of an increase in free-carrier concentration when the sample is exposed to 475 nm (2.6 eV) light provides further support for a nitrogen-related deep-acceptor level. A near-band-edge PL at 3.267 eV obtained at 80 K is tentatively assigned to nitrogen acceptor-bound exciton. Electron paramagnetic resonance provides evidence for the presence of nitrogen acceptors in our sample.

The deep-acceptor behavior of nitrogen can be explained by the low position of the ZnO valence band maximum relative to vacuum. Because of the low valence band, the N_O acceptor level does not lie in the valence band, but rather ~1.3 eV above the valence band maximum. This intrinsic feature of ZnO could prove a daunting challenge to its *p*-type doping.

CHAPTER 5 HYDROGEN-RELATED DEFECTS IN STRONTIUM TITANATE

5.1 Introduction

Hydrogen is a prevalent impurity in most oxide semiconductors. As discussed in Section 1.2, hydrogen strongly affects the electronic properties of oxides and it is a potential source of *n*-type conductivity. In this chapter, I discuss a new hydrogen-related defect in strontium titanate, with local vibrational modes (LVMs) at 3355 and 3384 cm^{-1}. In this work, we aim to determine the structure of this defect and develop insights into the behavior of hydrogen that would span other oxides.

5.2 Bulk single-crystal $SrTiO_3$

Nominally undoped $SrTiO_3$ single crystal samples were obtained from two sources, MaTeck GmbH and MTI Corporation. They were Verneuil-grown with standard dimensions 10 mm x 10 mm x 0.5 mm. Prior to thermal annealing I cut the samples into smaller pieces where one piece was set aside as a reference sample.

5.3 Hydrogen and/or deuterium annealing

For hydrogen and/or deuterium doping, the sample was annealed at $800^{o}C$ in a sealed quartz ampoule that was filled with 1/2 atm H_2 and/or D_2 gas. The annealing was performed in a horizontal tube furnace for 45 minutes and was terminated by quenching the ampoule to room temperature in water.

Figure 5.1 shows the IR absorbance spectra at 10 K for a $SrTiO_3$ sample after annealing in hydrogen and/or deuterium. In the hydrogen-annealed sample (top spectra), the previously reported absorption peaks around 3500 cm^{-1} (Wakim, 1968; Weber et al., 1986; Houde et al., 1987) associated with O-H bond stretching modes, are shown (labeled here as H_I). The set of "new" absorption peaks at 3355 and 3384 cm^{-1} is the focus of our study, labeled here as H_{II}. The ratio of H_I to H_{II} peak areas varied from sample to sample, suggesting that H_{II} involves a defect, the concentration of which is sample-dependent. From the areas of the O-H peaks (Jokela and McCluskey, 2005), we estimate the IR-active H concentration to be in the $10^{16} – 10^{17}$ cm^{-3} range.

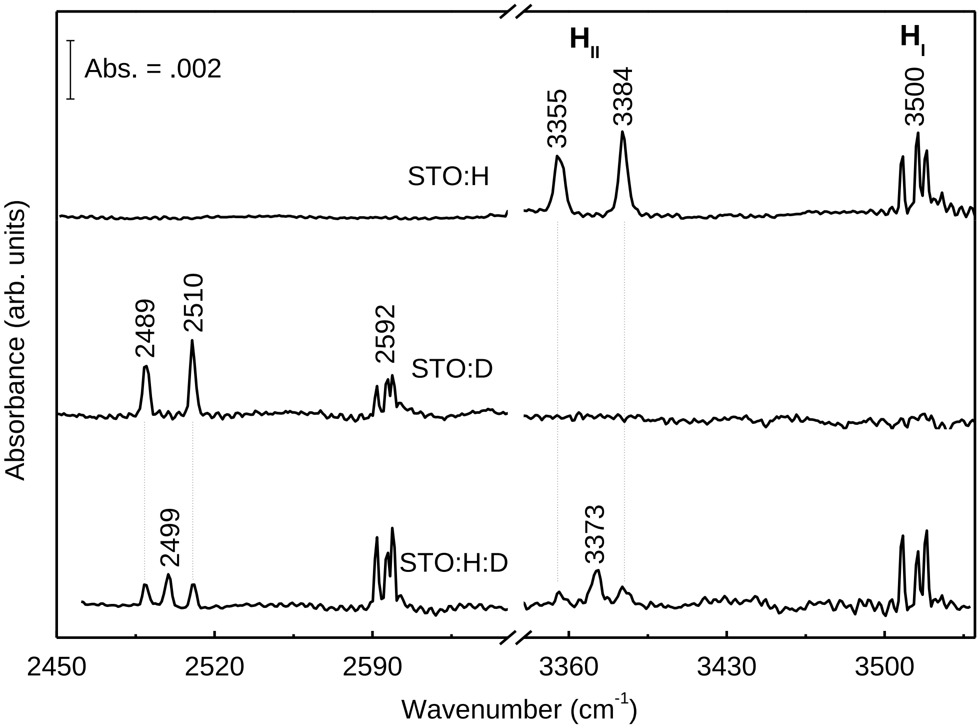

Figure 5.1: IR absorption spectra measured at 10 K after annealing in H_2 (top), D_2 (middle), and a mixture of $H_2 + D_2$ (bottom) at 800°C. Spectral resolution is 1 cm^{-1}.

When hydrogen is substituted by deuterium, the two H_{II} peaks are red-shifted to 2489 and 2510 cm^{-1}, respectively. The frequency ratios of the hydrogen- and deuterium-related peaks are

1.35, which is close to the value expected for a harmonic oscillator consisting of a hydrogen (deuterium) atom bound to an oxygen atom,

$$\sqrt{\mu_{OD}/\mu_{OH}} = 1.37 \tag{5.1}$$

where μ_{OH} and μ_{OD} are the reduced masses of the O-H and O-D units, respectively. When the sample is annealed in a mixture of hydrogen and deuterium, two additional peaks at 3373 and 2499 cm^{-1} are observed. Note that these peaks are in the regions of the O-H and O-D LVMs, respectively, of the H_{II} defect (Fig. 5.1). No extra peaks are observed near the region of the H_I LVMs. These observations indicate that the H_{II} absorption peaks (at 3355 and 3384 cm^{-1}) and the H_I peaks (around 3500 cm^{-1}) originate from two different defects. The H_I LVMs around 3500 cm^{-1} belong to a defect containing one hydrogen atom, whereas the LVMs at 3355 and 3384 cm^{-1} are due to two equivalent hydrogen atoms.

5.4 Coupled oscillator model

A useful and simple model that explains the vibrational modes of our H_{II} defect is the coupled oscillator (Fig. 5.2). Suppose the hydrogen and deuterium atoms have masses m_1 and m_2, respectively, each attached to a host oxygen atom which we assume to be rigid. The atoms are held by springs of force constants k and $k' = \varepsilon k$, where $0 < \varepsilon \ll 1$, as depicted in Fig. 5.2.

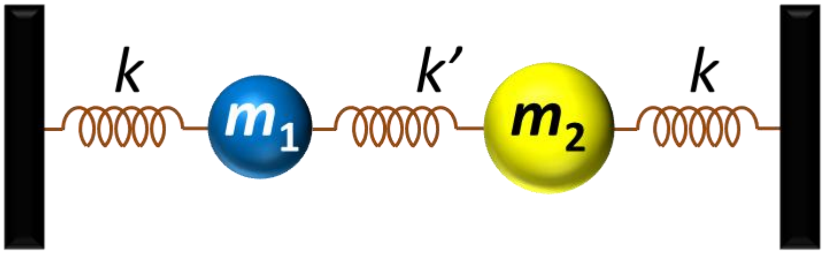

Figure 5.2: Coupled oscillator model for the modes of vibration of H_{II} defect.

In the equilibrium positions, the springs are neither stretched nor compressed. If we let x_1 and x_2 be the displacements of masses m_1 and m_2, respectively, the equations of motion can be written as

$$\begin{aligned} -kx_1 + k'(x_2 - x_1) &= m_1\ddot{x}_1; \\ -kx_2 - k'(x_2 - x_1) &= m_2\ddot{x}_2. \end{aligned} \tag{5.2}$$

The solutions to these equations can take the form

$$\begin{aligned} x_1 &= C_1 \cos(\omega t + \varphi); \\ x_2 &= C_2 \cos(\omega t + \varphi). \end{aligned} \tag{5.3}$$

where ω is the angular frequency and C_1 and C_2 are the amplitudes. Carrying out the derivatives of the above equations and substituting them back to Eqs. (5.2), we get

$$\begin{aligned} -kC_1 + k'(C_2 - C_1) &= -m_1\omega^2 C_1\,; \\ -kC_2 - \ k'(C_2 - C_1) &= -m_2\omega^2 C_2\,; \end{aligned} \tag{5.4}$$

or

$$\begin{aligned} (k + k' - m_1\omega^2)C_1 \ - k'C_2 &= 0; \\ -k'C_1 + (k + k' - m_2\omega^2)C_2 &= 0. \end{aligned} \tag{5.5}$$

Equations (5.5) are a pair of simultaneous, homogeneous equations for the amplitudes C_1 and C_2. Nontrivial solutions for these equations exist if and only if the determinant of the system is zero. Thus,

$$\begin{vmatrix} k + k' - m_1\omega^2 & -k' \\ -k' & k + k' - m_2\omega^2 \end{vmatrix} = 0. \tag{5.6}$$

Multiplying out the determinant, we get

$$(k + k' - m_1\omega^2)(k + k' - m_2\omega^2) - (k')^2 = 0. \tag{5.7}$$

Now consider $m_1 = m$ for the H atom and $m_2 = 2m$ for the D atom. Using Eq. (5.7), we solve the frequencies of the normal modes for a system of coupled oscillators consisting of two H masses, of two D masses, and of an H and D masses. The results are summarized in Table 5.1. In each system there are two normal modes. The one with the lower frequency is the symmetric mode, where the masses are moving in the same direction (in phase). The other mode is the antisymmetric mode, where the masses are moving in opposite directions (out of phase). For the HD complex, the symmetry is broken. The low frequency mode corresponds to a large D amplitude ("D-like") while the high-frequency mode is H-like.

Using the experimental values of the symmetric and antisymmetric LVMs of the H_{II} defect (Fig. 5.1), we obtain $\varepsilon = 0.0043$. We then calculate the frequencies of the normal modes for the different coupled oscillator systems given in Table 5.1. The calculated frequencies, given in terms of $\sqrt{k/m}$, are shown in Fig. 5.2b. The relative positions of the normal modes are consistent with our experimental results (Fig. 5.1). Differences between theory and experiment likely result from anharmonic effects (Sec. 2.4).

Coupled oscillator system	Symmetric	Anti-symmetric
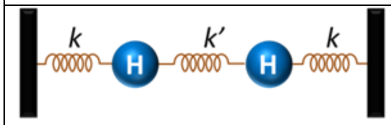	$\omega = \sqrt{\dfrac{k}{m}}$	$\omega = \sqrt{1+2\varepsilon}\sqrt{\dfrac{k}{m}}$
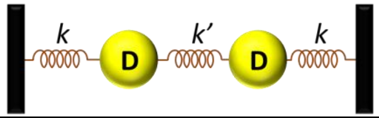	$\omega = \sqrt{\dfrac{k}{2m}}$	$\omega = \sqrt{1+2\varepsilon}\sqrt{\dfrac{k}{2m}}$
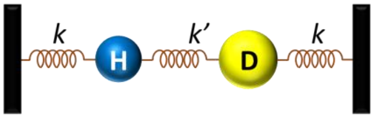	“D-like”	“H-like”
	$\omega = \dfrac{1}{2}\sqrt{3(1+\varepsilon) - \sqrt{1+2\varepsilon+9\varepsilon^2}}\sqrt{\dfrac{k}{m}}$	$\omega = \dfrac{1}{2}\sqrt{3(1+\varepsilon) + \sqrt{1+2\varepsilon+9\varepsilon^2}}\sqrt{\dfrac{k}{m}}$

Table 5.1: Normal mode frequencies of coupled oscillator systems

.

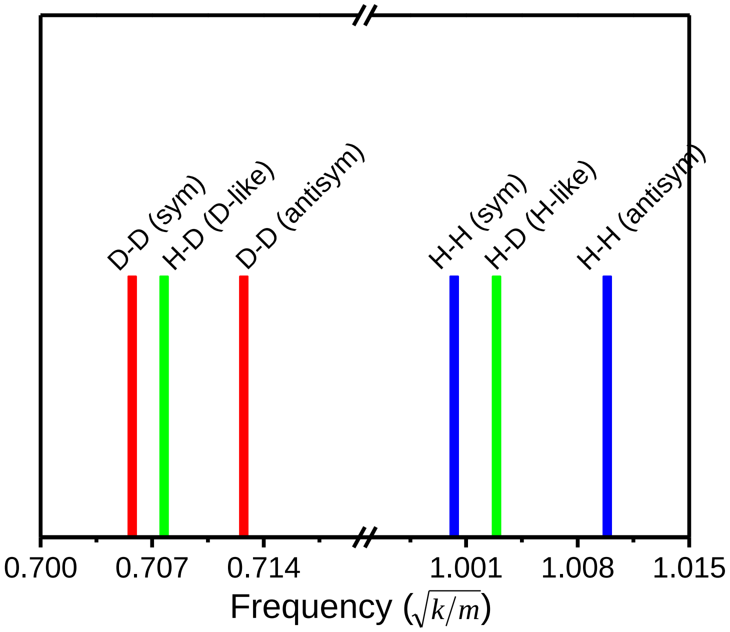

Figure 5.3: Calculated normal mode frequencies in units of $\sqrt{k/m}$.

5.5 Temperature dependence of LVMs

The LVMs of a deuterated $SrTiO_3$ samples are displayed as a function of temperature in Fig 5.4. At low temperatures, the absorption peaks split, due to the reduction in symmetry as the crystal transforms from the cubic to the tetragonal phase. In Figure 5.4a, the H_I defect absorption peak splits into three components below the transition temperature (~105 K) (Weber et al., 1986; Houde et al., 1987). The H_{II} defect also shows a splitting of the O-H peaks, but the magnitude is much less (Fig. 5.4b). A Lorentzian fit to one of the H_{II} bands (Fig. 5.4c) reveals that it splits into three components. Figure 5.4a also shows that the LVMs of the H_I defect shift upwards in frequency as the temperature decreases. In contrast, the LVMs of the H_{II} defect (Fig. 5.4b) show a negligible shift in frequency, suggesting a weaker perturbation by the surrounding host atoms. This indicates the involvement of a vacancy (Mackie et al., 2009), where the open volume reduces the effect of the lattice on the O-H LVMs. A strontium vacancy is likely candidate because it is a double acceptor, making it energetically favorable for two H atoms to give their electrons to the oxygen atoms and form O-H bonds. Therefore, we propose that the H_{II} defect is a strontium vacancy passivated by two hydrogen atoms.

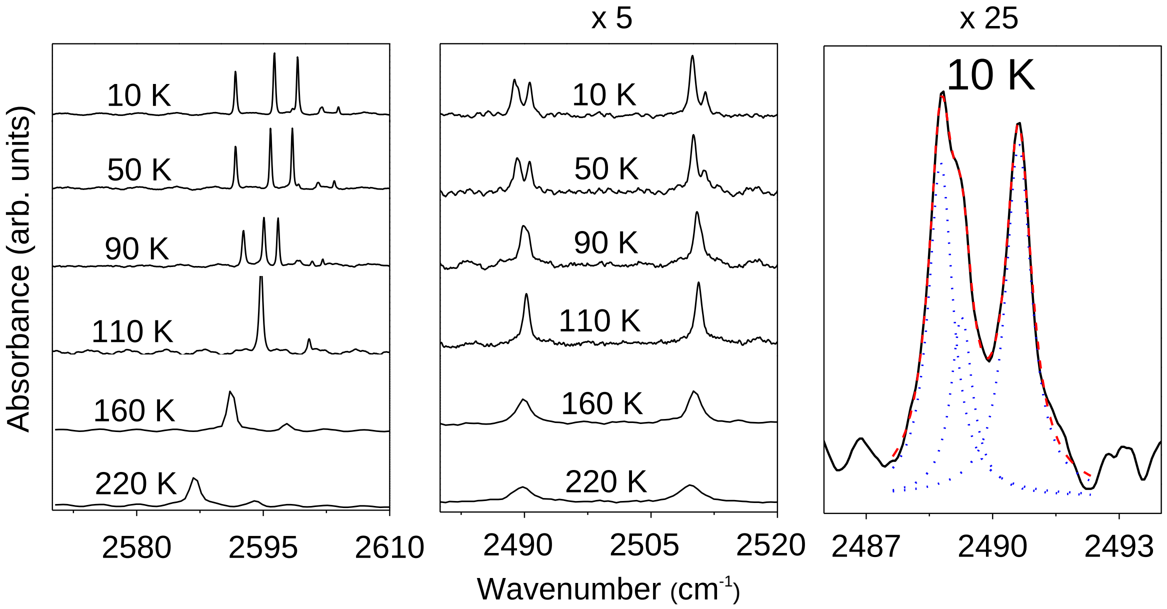

(a) (b) (c)

Figure 5.4: Temperature dependence of the LVM frequencies of (a) H_I and (b) H_{II} defects of deuterated $SrTiO_3$. (c) Lorentzian fitting of one of the H_{II} absorption bands at 10 K showing three overlapping peaks. Spectral resolution is 0.2 cm^{-1} at lower temperatures (<110 K).

5.6 Hydrogen defect model

To account for the splitting of the O-H LVMs (Fig. 5.4), we introduce a model where each hydrogen atom is bound to a nearest-neighbor oxygen atom and directed towards the strontium vacancy (Fig. 5.5). As we can see in Fig. 5.5, there are three possible configurations for the two H atoms. At high temperatures, these configurations are equivalent due to the cubic symmetry of the crystal structure, resulting in two absorption peaks corresponding to the symmetric (3355 cm^{-1}) and antisymmetric (3384 cm^{-1}) normal modes. At low temperatures, there is a lowering of the symmetry of the structure due to the rotation of the oxygen octahedra about the *c* axis, and the three configurations are no longer equivalent. This accounts for the triplet splitting of the H_{II} peaks. As the tetragonal phase is actually polycrystalline, the relative intensities of the split peaks varied somewhat from run to run, due to the random distribution of domains.

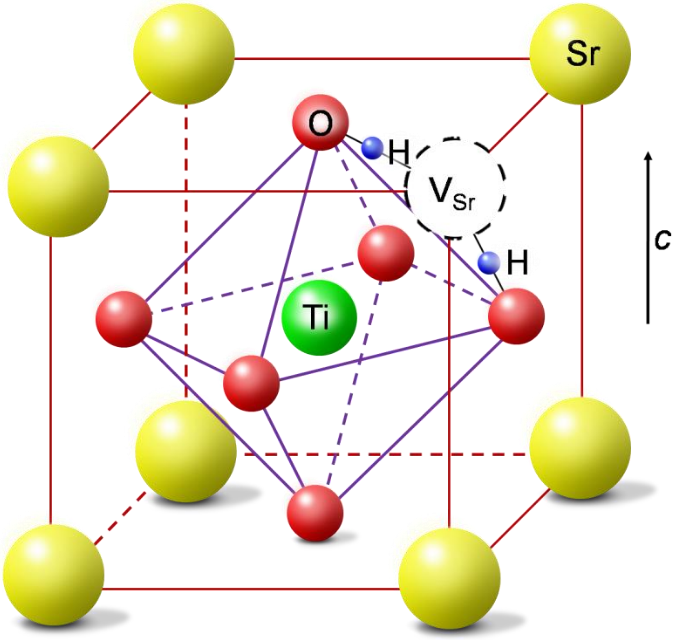

Figure 5.5: Proposed model of the H_{II} defect: a strontium vacancy passivated by two hydrogen atoms.

5.7 Isochronal annealing

In order to study the stability of the O-H complexes, I performed a series of isochronal anneals at temperatures from 300 to 1100°C. Each anneal had a duration of 30 min. and was carried out in the open air. The IR absorbance spectra were recorded after each annealing temperature step.

In Figure 5.6 the results of isochronal annealing experiments on hydrogenated $SrTiO_3$ samples are shown. At each step, the IR absorbance spectra were recorded at 220 K and the integrated absorbance was calculated for each related peak. The figure provides evidence that H_I and H_{II} defects do not have the same origin, as they exhibit different thermal kinetics. The results also confirm that the H_{II} LVMs (the 3355 and 3384 cm^{-1} peaks) belong to the same defect, as they retain the same relative intensity regardless of the annealing temperature. The increase in H_I population near 400^oC suggests that there is a reservoir of “hidden hydrogen” that is IR-inactive. At temperatures greater than 400^oC, these hydrogen atoms are released from the reservoir, forming O-H bonds that are observable in the IR.

To probe this phenomenon further, I performed isochronal annealing on a hydrogen-annealed sample that was subsequently deuterated. Figure 5.7 shows the absorption spectra obtained at 200 K for each annealing step. Before annealing the sample in air, an absorption spectrum of the sample was obtained (bottom), which shows deuterium-related peaks. The lack of hydrogen peaks implies that, upon deuteration, the deuterium atoms displaced the hydrogen atoms from their sites. However, when the sample was annealed at 400^oC, a weak H-related peak appeared. At 500^oC, the H-related peak became strong and HD peaks emerged. At higher temperatures, the D-related peaks disappeared, leaving only H-related peaks. These observations are consistent with our model of hidden hydrogen in the crystal that becomes mobile at 400^oC. These hydrogen atoms overwhelm the deuterium atoms, completely displacing them at 600^oC.

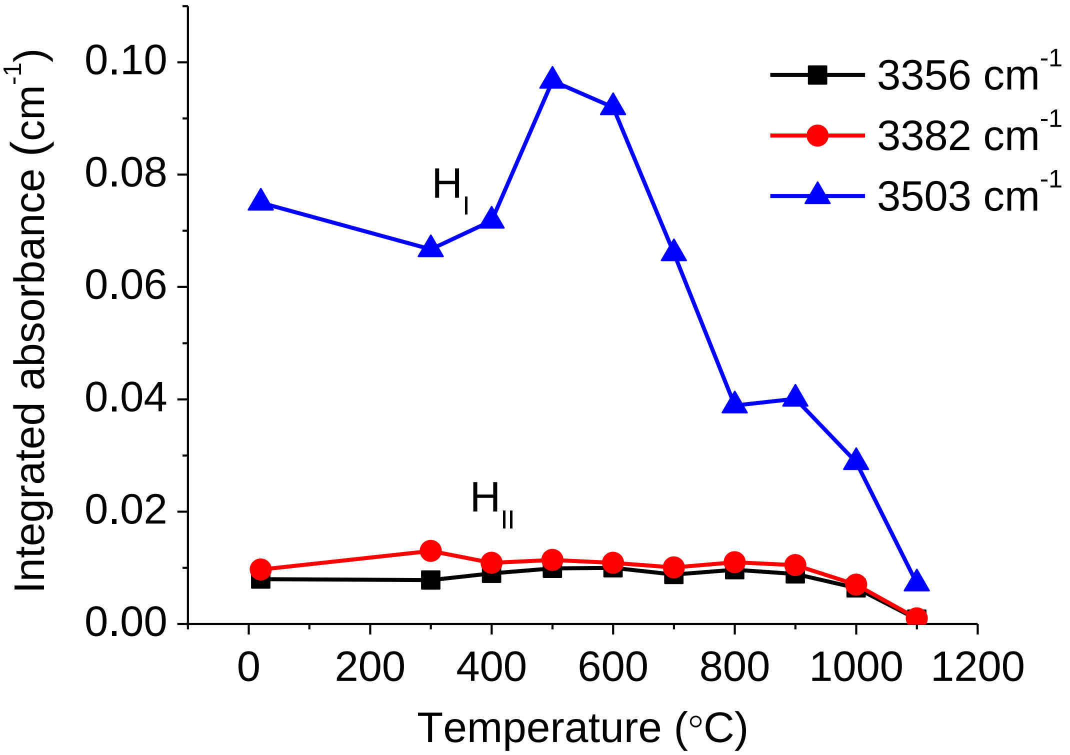

Figure 5.6: The intensity (integrated absorbance) of the H_I (▲) and H_{II} (●, ■) peaks for a hydrogenated $SrTiO_3$ sample annealed in open air at the indicated temperature. Each absorbance measurement was recorded at 220 K.

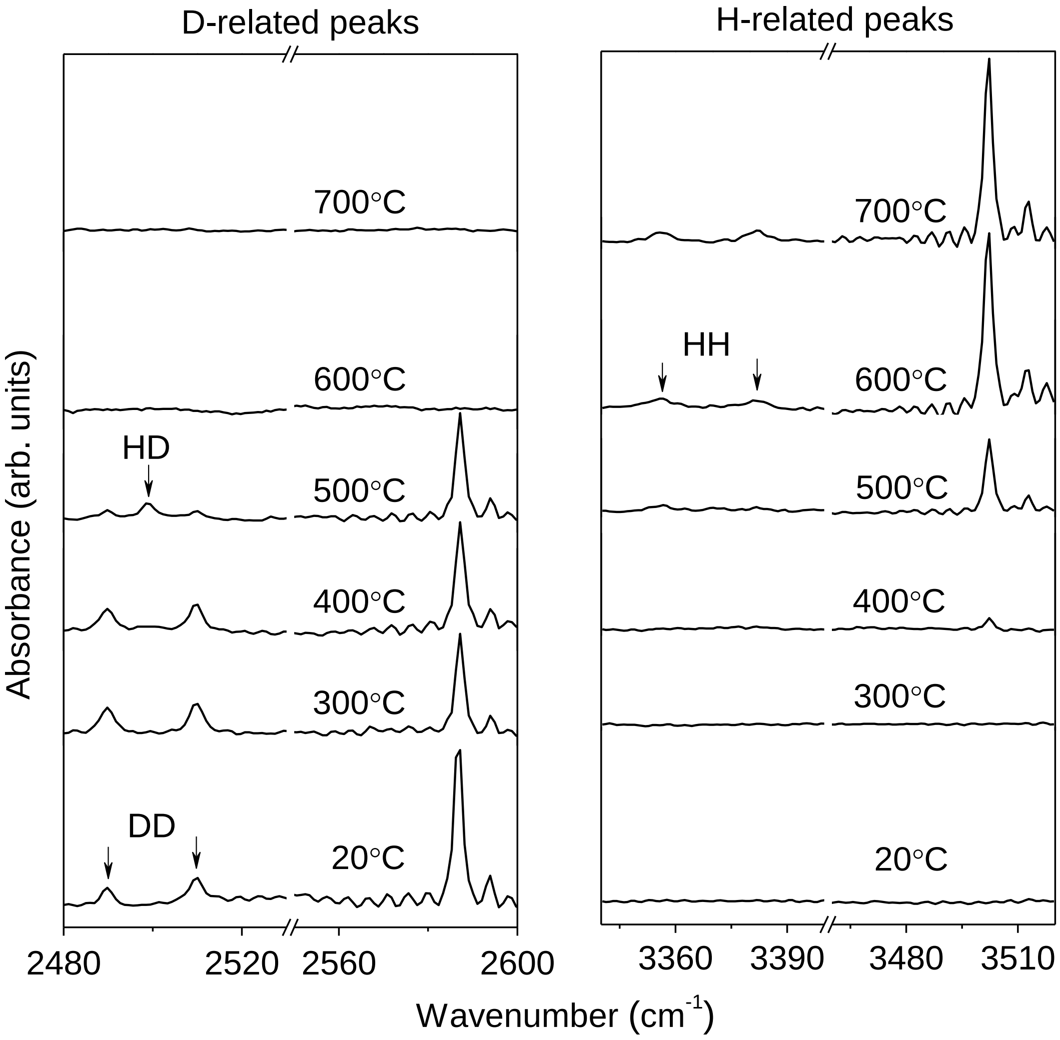

Figure 5.7: IR absorption spectra measured for the hydrogenated and subsequently deuterated $SrTiO_3$ sample after annealing in air at temperatures as shown. IR spectra were recorded at 200 K. Spectra are vertically offset for clarity.

An obvious question is: what is the identity of the hidden hydrogen? It has been found that, in ZnO, hidden hydrogen exists in the form of hydrogen molecules H_2. The H_2 vibrations has a weak dipole moment such that it has not been detected by IR absorption (Shi et. al., 2004), but has been observed by Raman scattering (Lavrov et. al., 2009). Assuming that the same is true for $SrTiO_3$, annealing the sample at temperatures from 400 to 700°C dissociates the H_2, and the liberated H are trapped before they can diffuse out of the sample. The trapped hydrogen atoms form IR active O-H defects and enhance the H_I peaks. The dissociation temperature of 400ºC is similar to that for H_2 molecules in ZnO (Shi et. al., 2004). Further annealing at higher temperatures causes these H-related peaks to decay as hydrogen diffuses out of the sample (Fig. 5.6).

5.8 Positron annihilation spectroscopy

A useful and effective technique to probe vacancy-type defects in a solid is positron annihilation spectroscopy (PAS), due to the high sensitivity of positron to open volume defects (Schultz and Lynn, 1988; Saarinen et al., 1998). After trapping at a defect, the positron will annihilate with an electron from the immediate surroundings of the defect, producing two 511 keV gamma ray photons. The information related to the defect is obtained from properties such as the Doppler broadening of the photo-peak and the lifetime of the positrons (Clement et al., 1996). PAS has been used to characterize vacancy defects in $SrTiO_3$ (Mackie et al., 2009; Gentils et al., 2010) as well as in other oxide materials such as ZnO (Tuomisto et al., 2003; Selim et al., 2007).

Through Prof. K. Lynn and Dr. M. Weber, positron annihilation measurements using the Doppler broadening technique were performed on our samples to probe for the presence of vacancy-type defects. The two samples that were probed, namely samples 1 and 2, exhibit characteristic IR absorption spectra. Sample 1 shows both H_I and H_{II} defects whereas sample 2 exhibits only the H_I defect (Fig. 5.8). The sidebands on the high energy side of H_I in sample 1 have been attributed to Fe (Gröne at al., 1990), a common impurity in $SrTiO_3$ (Mochizuki et al., 2007).

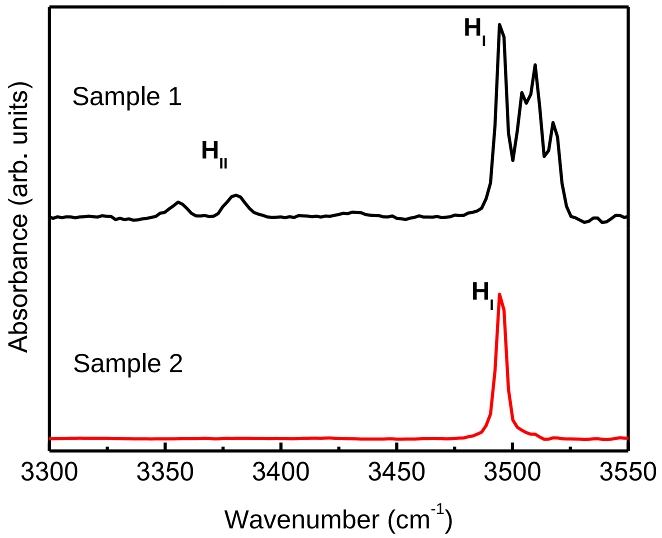

Figure 5.8: IR absorption spectra at room temperature.

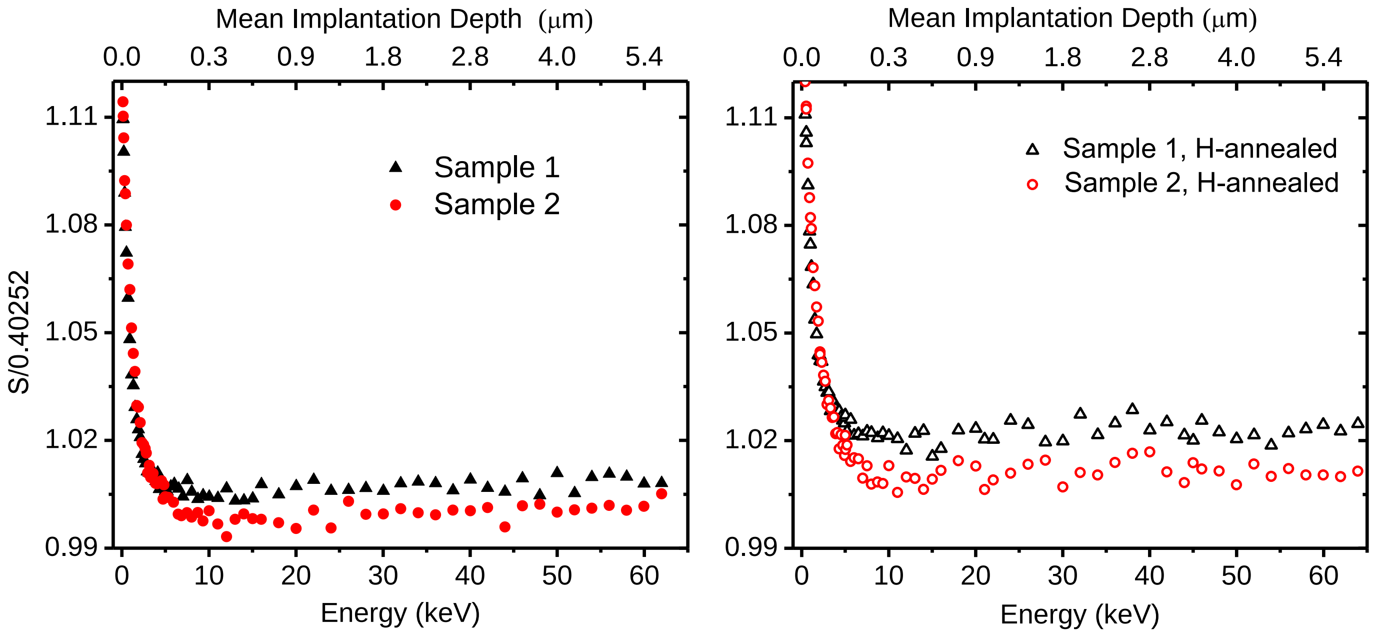

(a)

(b)

Figure 5.9: Open volume defect parameter *S* as a function of implantation energy of (a) as-received samples and (b) H_2-annealed samples. Spectra taken by M. Weber and N. Parmar.

Positron annihilation measurements were carried out with a positron beam energy range of 0.1 to 70 keV. When positrons are trapped at vacancy defects, their annihilation characteristics change. The Doppler broadening spectra of the annihilation radiation were recorded by a high-purity Ge detector. The annihilation peak is characterized by a line-shape parameter *S* (Clement et al., 1996) which reflects the change due to annihilation with low momentum valence electrons. Hence, open volume type defects such as vacancies tend to increase the *S* parameter.

Figure 5.9 displays the *S* parameter as a function of the positron implantation energy of the samples. At low energies (E < 5 keV) the high values of *S* is due to positronium formation at the surface. In the bulk region (E > 15 keV) sample 1 exhibits higher *S* values than sample 2, indicating stronger trapping of positrons by the defects in sample 1. We note that sample 1 contains H_{II} defect which we attributed to strontium vacancy. With its negative charge state, the Sr vacancy is an effective trapping center for positrons (McGuire et al., 2006). This seems to be consistent with our proposed model of H_{II} defect. However, a Ti vacancy, with its negative charge state, is also an effective positron trap. Thus, the higher concentration of defects in sample 1 can be attributed to either Sr or Ti vacancies.

The samples displayed a corresponding increase in *S* parameter after hydrogen annealing (Fig. 5.9b). This may imply a change in charge state and/or size of the defects. Positron lifetime measurements, through Dr. F. Selim and Chris Varney, were performed on these H-annealed samples. They obtained defect lifetime values of 315 ps for the H-annealed sample 1 and 250 ps for the H-annealed sample 2. Calculated lifetimes reported for $SrTiO_3$ have been summarized in the literature (Mackie et al., 2009; Keeble et al, 2010). For the Ti vacancy, the calculated lifetime values span the range 156 – 195 ps and for Sr the vacancy, 238 – 279 ps. The calculated bulk lifetime values range from 121 – 151 ps. Experimental positron lifetime values obtained by

Mackie et al. (2009) for samples from different vendors range from 198 to 276 ps. The huge lifetime value (315 ps) obtained for sample 1 suggests that it may have multivacancies or vacancy complexes. The value is close to the calculated value for Ti-3O-Sr vacancy complex (Keeble et al. 2010). If the measurement was reliable, then it suggests that the H annealing may have created vacancy nearest-neighbor complexes. Sample 2 has a lower defect lifetime value (250 ps), which may be a Ti-O-Ti vacancy complex. Unfortunately, the lifetime values of the reference samples were lacking so we are not able to draw insights from how the lifetime values changed after annealing. Prior to the lifetime measurements, the samples were already annealed for other experimental purposes.

We had a couple of available samples which I managed systematically for positron lifetime measurements. Our goal was to suppress the Sr vacancies in the samples and investigate the resulting defect lifetimes and correlate with IR absorption. I annealed the samples in strontium oxide (Sr metal is extremely reactive chemically so I used SrO; freshly exposed Sr metal turned rapidly into yellowish color with the formation of the oxide). I placed the samples in an ampoule along with 0.5 g of SrO. The ampoule was evacuated before sealing. The sealed ampoule was kept in the furnace for 2 h at 1120°C. At the end of the annealing, it was taken out of the furnace as quickly as possible and allowed to cool to room temperature. The infrared absorption of the sample before and after SrO anneal is shown in Fig. 5.10a, with the corresponding measured defect lifetime values. We can see the magnitude of the decrease in H_{II} peaks is greater than that in H_I peak after anneal. As-received, the sample has a lifetime value of 284 ps, a characteristic result experimentally attributed to Sr-vacancy related defects (Mackie et al., 2009). After SrO anneal, the lifetime was reduced to 223 ps. The reduction in lifetime implies the suppression of Sr vacancies. If we correlate the decrease in H_{II} population with the reduction in Sr vacancies, we seem to have provided an evidence for our H_{II} defect model. We also note an interesting time-dependent behavior of the IR absorption peaks, as shown in Fig. 5.10b, where a spectrum was taken just after annealing (July 26, 2011) and about a month later when the positron lifetime measurements were to be taken. Perhaps after the annealing, it may have taken some time for the sample to relax to equilibrium, and hydrogen may leave H_{II} sites (i.e., Sr vacancies) and go to H_I and V_O sites.

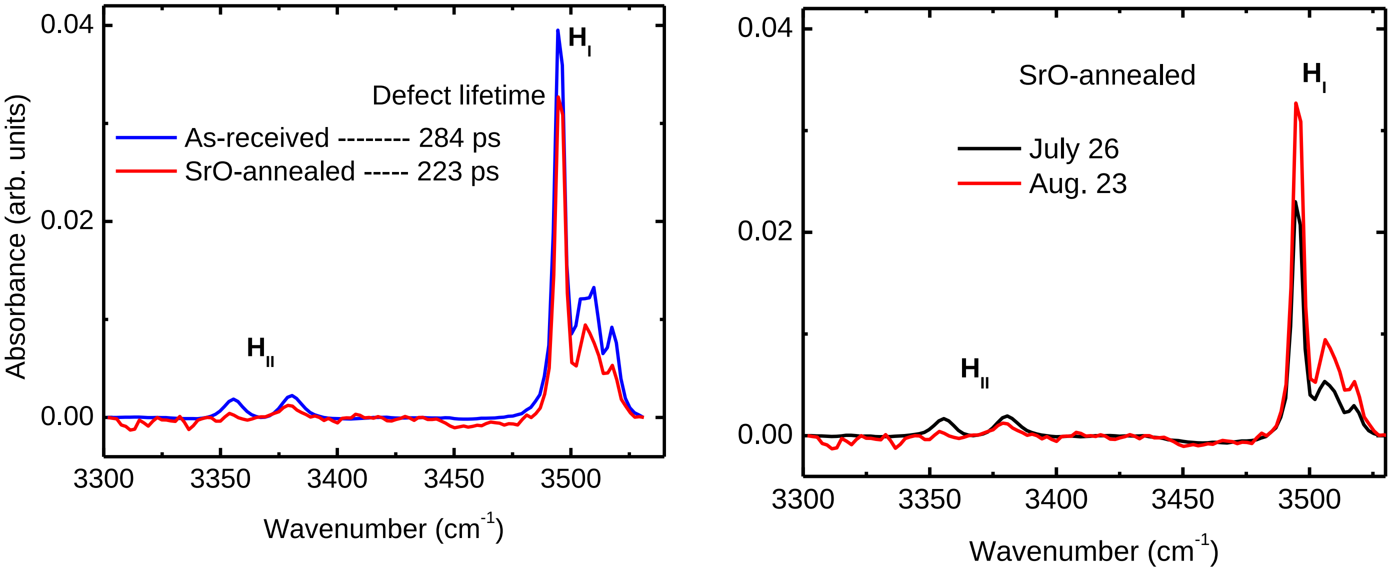

Figure 5.10: (a) IR absorption and lifetime values before and after annealing in SrO. (b) Time dependence of IR absorption of SrO-annealed sample.

I obtained a set of samples *nominally* identical (i.e., from the same supplier) to those used in SrO anneal. This time we looked at the effect of annealing in TiO_2. Unexpectedly these new set of samples has a lifetime value of 222 ps, much lower than that of the first batch. This may suggest Ti vacancies with a low concentration of Sr vacancy defects, or an unresolved weighted average of Ti vacancy and Ti-O vacancy defect populations. After annealing in TiO_2, the lifetime value decreased to 202 ps. The reduction in lifetime value may be due to the filling up of the Ti vacancies. The IR spectrum after the anneal shows a huge free carrier absorption. The oxygen vacancies may have captured H atoms and form H_O. Due to the huge noise in the IR absorption after the anneal, H_I and H_{II} peaks were not detected in the spectrum.

5.9 Free-carrier absorption of H-annealed $SrTiO_3$

Figure 5.11a shows the temperature-dependent IR absorption spectra of H-annealed sample. The monotonic increase of the absorption with increasing wavelength (decreasing frequency) is characteristic of free-carrier absorption. We can also see a turning point in the absorption at higher temperatures.

From Drude model of free-carrier absorption (McCluskey and Haller, 2012), the absorption coefficient as a function of frequency ω is given by

$$\alpha = \frac{n}{c}\frac{{\omega_p}^2\gamma}{\omega^2} \qquad 5.8$$

where n is the index of refraction, c is the speed of light, γ is a damping constant, and ω_p is the *plasma* frequency defined as

$$\omega_p = \sqrt{\frac{Ne^2}{\varepsilon_0\varepsilon_\infty m^*}}. \qquad 5.9$$

where N is the free carrier density, e is the carrier charge, ε_∞ is the dielectric constant at high frequencies, and m^* is the effective mass of the electron. Since $= \frac{2\pi c}{\lambda}$, the free-carrier absorption in the classical Drude model is proportional to λ^2. Treatments of electron scattering from acoustical phonons, optical phonons, and ionized impurities give free-carrier absorption varying as $\lambda^{1.5-2}$, $\lambda^{2.5}$, and λ^3, respectively (Pankove, 1971).

To model our free-carrier data, we use Lorentz-Drude model which takes account the contribution of lattice vibration (McCluskey and Haller, 2012). The dielectric function is given by

$$\varepsilon(\omega) = \varepsilon_\infty \left(1 + \frac{{\omega_{LO}}^2 - {\omega_{TO}}^2}{{\omega_{TO}}^2 - \omega^2 - i\Gamma\omega} - \frac{{\omega_p}^2}{\omega^2 + i\gamma\omega}\right) \tag{5.10}$$

where ω_{LO} and ω_{TO} are the longitudinal optical (LO) and transverse optical (TO) phonon frequencies ($\omega_{LO} > \omega_{TO}$); Γ is the phonon damping factor. The first two terms in Eq. (5.10) comprise the phonon contribution while the third term reflects the free-carrier contribution to the dielectric function.

To calculate absorption, we use the complex dielectric function

$$\varepsilon = \varepsilon_R + i\varepsilon_I \,. \tag{5.11}$$

The index of refraction (Kittel, 2005) is given by

$$n + i\kappa = \sqrt{\varepsilon} \tag{5.12}$$

where n and κ are the real and imaginary parts of the index, respectively. To calculate absorption, we need the imaginary component of ε:

$$\varepsilon_I = 2n\kappa. \tag{5.13}$$

The absorption coefficient α is given by

$$\alpha = \frac{2\omega\kappa}{c} \tag{5.14}$$

Substituting Eq. (5.13):

$$\alpha = \frac{2\omega\kappa}{c} = \frac{1}{nc}\varepsilon_I\omega \qquad 5.15$$

Using the imaginary part of Eq. 5.10:

$$\varepsilon_I = \varepsilon_\infty\left[\frac{\gamma{\omega_p}^2}{\omega^2+\gamma^2} + \frac{\Gamma\omega^2({\omega_{LO}}^2 - {\omega_{TO}}^2)}{\Gamma^2\omega^2 + (-\omega^2 + {\omega_{TO}}^2)^2}\right], \qquad 5.16$$

the absorption coefficient can be written:

$$\alpha = \frac{\varepsilon_\infty}{n\,c}\left[\frac{\gamma{\omega_p}^2}{\omega^2+\gamma^2} + \frac{\Gamma\omega^2({\omega_{LO}}^2 - {\omega_{TO}}^2)}{\Gamma^2\omega^2 + (-\omega^2 + {\omega_{TO}}^2)^2}\right]. \qquad 5.17$$

Figure 5.11b shows the fitting results using Eq. (5.17) for the IR absorption data in Fig. 11a. The plasma frequency ω_p is set as adjustable parameter. The calculations were performed on a set of absorption data obtained at temperatures above ~105 K (phase transition temperature). The parameter values may not apply for low-temperature tetragonal phase.

A plot of the calculated plasma frequency as function of temperature is shown in Fig. 5.12. The plasma frequency of *n*-type $SrTiO_3$ has been reported to increase with decreasing temperature (Gervais et al., 1993; Bi et al., 2006). Assuming the carrier density is independent of temperature (as presented in Sec. 5.10), Eq. (5.9) suggests that the effective mass of the charge carriers decreases upon cooling.

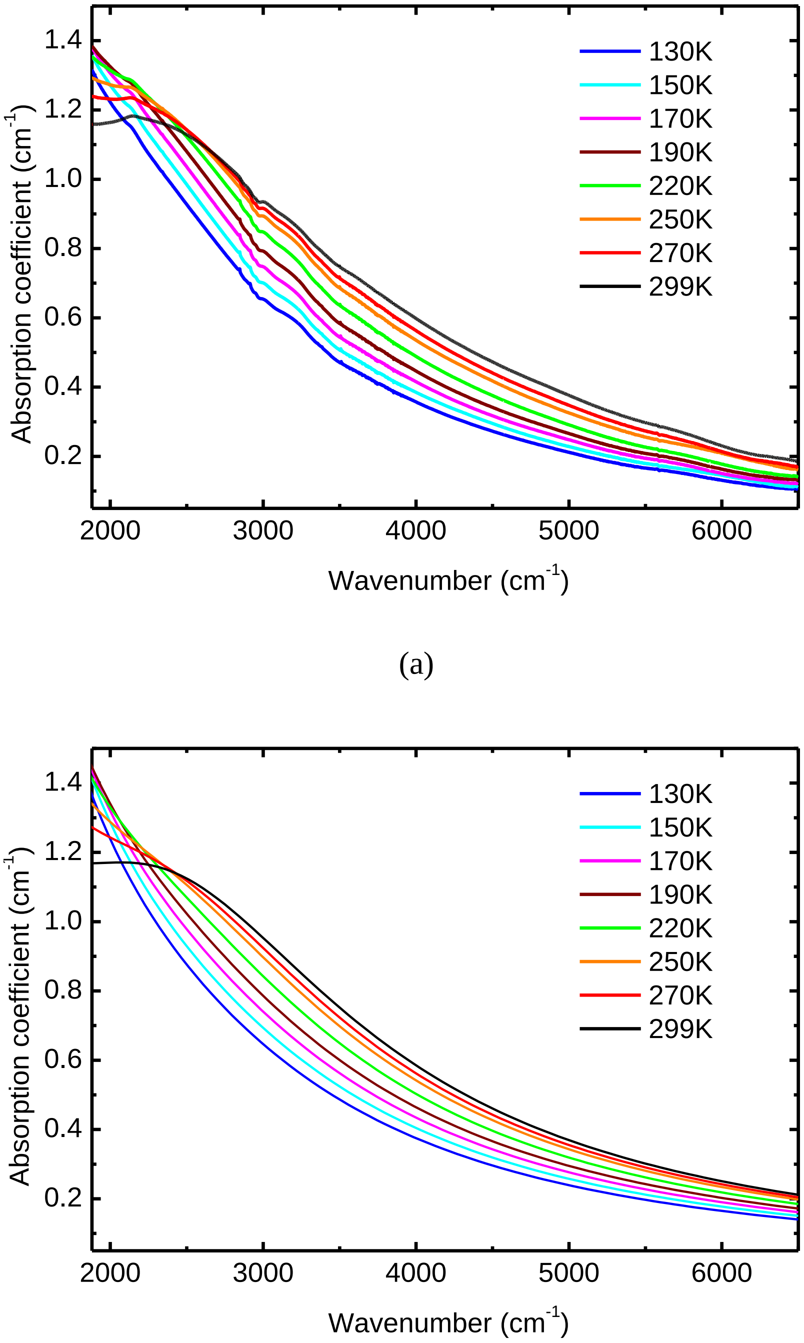

(a)

(b)

Figure 5.11: (a) IR absorption for H-annealed SrTiO$_3$ at different temperatures. (b) Calculated absorption using Eq. (5.17). Parameters are $\omega_{LO} = 6750\ \mathrm{cm}^{-1}$, $\omega_{TO} = 2490\ \mathrm{cm}^{-1}$, $\omega_p = 3331\ \mathrm{cm}^{-1}$, $\gamma = 300\ \mathrm{cm}^{-1}$, and $\Gamma = 500\ \mathrm{cm}^{-1}$.

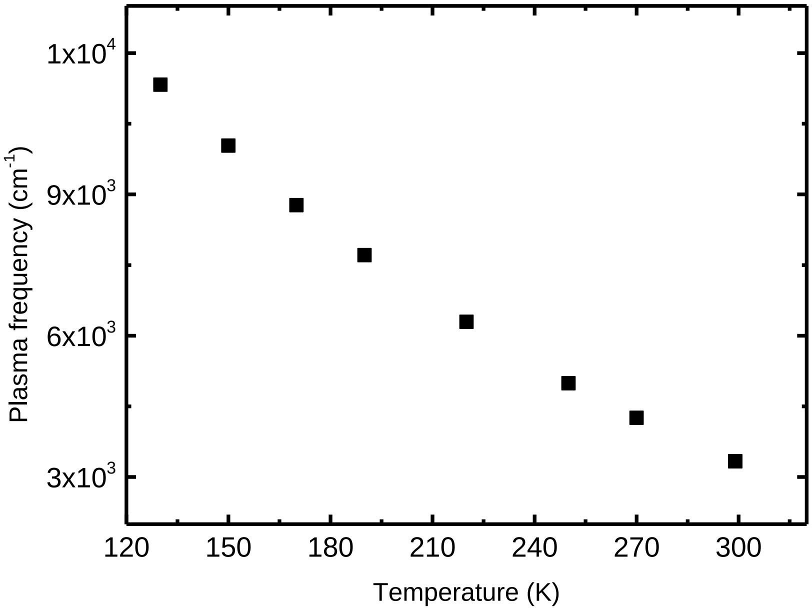

Figure 5.12: Temperature dependence of the plasma frequency in H-annealed $SrTiO_3$.

5.10 Hall effect measurements of H-annealed $SrTiO_3$

The Hall effect measurement of a hydrogen-annealed sample at room temperature shows an electron density of 1.86×10^{17} cm^{-3}, consistent with the increase in free-carrier absorption exhibited by its IR absorption. The carrier density as a function of temperature of the H-annealed sample is shown in Fig. 5.12a, which shows an almost absence of carrier freeze-out. This may be attributed to the large dielectric constant of $SrTiO_3$, ensuring that carriers ionized from hydrogenic donors will remain in the conduction band down to lower temperatures. Hall mobility is strongly temperature dependent, as shown in Fig 5.12b. It exhibits a power-law dependence of the form μ = 8.8 x 10^7 $T^{-2.9}$ cm^2/Vs, similar to prior works (Frederikse et al., 1964; Tufte and Chapman, 1967; Gentils et al., 2010), suggesting scattering of free carriers from optical phonons.

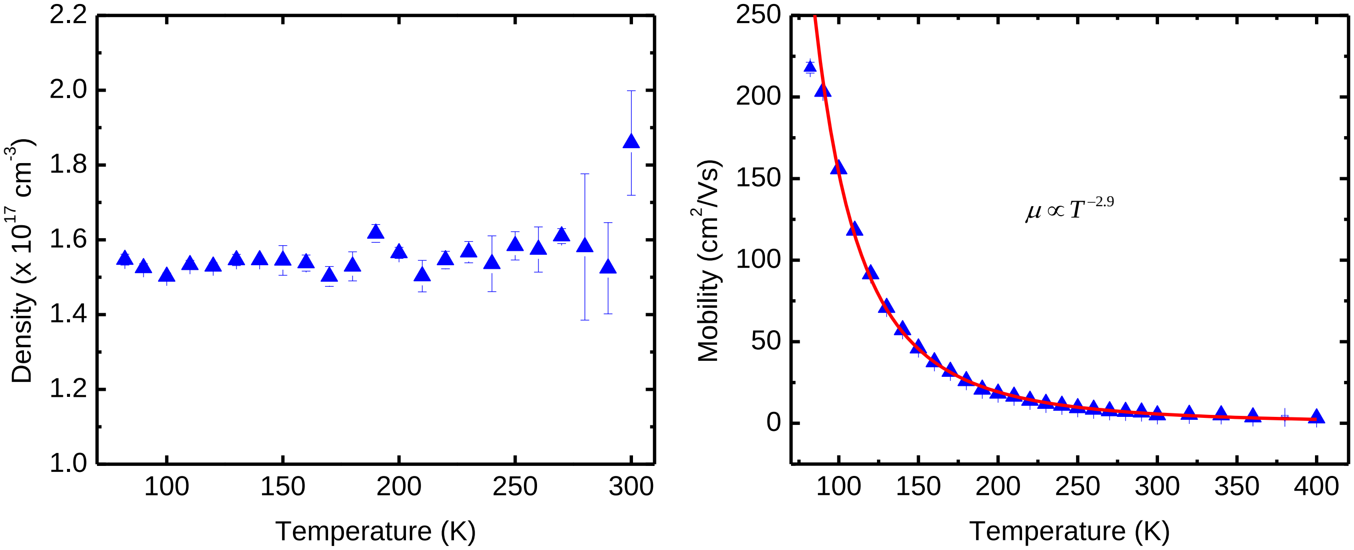

(a)

(b)

Figure 5.13: (a) Electron density n and (b) mobility μ as a function of temperature T of H-annealed $SrTiO_3$ sample.

5.11 Conclusions

We have observed a hydrogen-related defect in $SrTiO_3$, which we tentatively attribute to a Sr vacancy passivated by two hydrogen atoms. The results of isochronal annealing experiments suggest the presence of a hidden hydrogen species, possibly H_2 molecules. It is noteworthy that in ZnO, a much less ionic crystal, hydrogen passivates Zn vacancies (Lavrov et al., 2002) and forms H_2 molecules (Jokela and McCluskey, 2005; Shi et. al., 2004). Based on our observations, we therefore suggest “universal behavior” of hydrogen in a diverse range of oxides.

In our effort to experimentally verify our H_{II} model through positron annihilation measurements, preliminary results suggest a correlation between vacancies and the H_{II} peaks. But further work may be performed if we could obtain identical samples and perform the annealing experiments systematically. Differences were observed between samples from the same supplier, thus we were not able to compare between the SrO and TiO_2 annealing results.

A further challenge to positron annihilation spectroscopy would be the identification of Sr- and Ti-vacancy and their complexes with hydrogen. Theoretical work by other groups, motivated by our experiments, is investigating the formation energies of native vacancies and their complexes with hydrogen.

CHAPTER 6 REVISITING HYDROGEN IN ZNO

6.1 Introduction

As I have discussed in Chapter 1 (Section 1.2), hydrogen was shown to be a shallow donor in ZnO, based on the theoretical work of Van de Walle (2000). This has stimulated further studies into the electrical and structural properties of hydrogen in ZnO. The low energy of the conduction-band minimum (CBM) relative to the vacuum results in the H level being above the CBM (Van de Walle and Neugebauer, 2003; Kılıç and Zunger, 2002). Experimental evidence that H is a shallow donor in ZnO include results from muonium-implanted ZnO (Cox et al., 2001; Gil et al., 2001) and electron-nuclear resonance measurements on lightly doped, *n*-type ZnO (Hoffman et al., 2002).

In order to determine the microscopic structure of H donors, IR absorption spectroscopy was used as a tool to identify and investigate hydrogen-related defects in ZnO (McCluskey et al., 2002; Lavrov et al., 2002). Previous studies suggested two of these defects as candidates for possible shallow donors. The first was tentatively identified as *bond-centered* hydrogen with the O–H bond aligned with the *c* axis of the crystal (Lavrov et al., 2002). This defect has a stretch LVM with a frequency of $3611.3\ cm^{-1}$ at 10 K. In this Chapter I will refer to this defect as the *Lavrov* defect. The second defect was identified as hydrogen located at the *antibonding* site with the O–H bond oriented 112° from the *c* axis (McCluskey et al., 2002). The LVM frequency of the defect at 10 K was found to be $3326.3\ cm^{-1}$(~3336 cm^{-1} at room temperature) and will be referred to as the *McCluskey* defect. Both defects have been found to be unstable for thermal annealing at considerably low temperatures (Lavrov et al., 2002; Jokela and McCluskey, 2005; Shi et al., 2004). Shi et al. (2005) also showed that the intensity of the peaks related to these defects depended on the method of crystal growth. Cermet Inc. samples which are grown by melt exhibit a strong McCluskey peak, whereas Eagle Picher samples which are grown via chemical vapor transport show a strong Lavrov peak (Shi et al., 2005).

A recent study (Lavrov et al., 2009) based on Raman scattering, IR absorption, PL, and photoconductivity suggests that the Lavrov defect is a shallow donor. As for the McCluskey defect, the microscopic structure is still debatable. Studies proposed a Ca-H complex (McCluskey and Jokela, 2007; Li et al., 2008) and a Zn vacancy passivated by a hydrogen atom in the negative charge state, $V_{Zn}H^-$, as alternative models (Lavrov et al., 2007). Based on the IR absorption study of this defect under sub band gap illumination (Herklotz et al., 2010), it is suggested that the McCluskey defect has a deep level in the band gap of ZnO.

First-principles calculations by Janotti and Van de Walle (2007a) showed that H can substitute on an oxygen site and has a low formation energy and act as a shallow donor. Substitutional hydrogen (H_O) can be thought of as an O vacancy with a single H atom near the center. The calculated vibrational frequency is 800 cm^{-1}. Possibly due to the strong free-carrier absorption in this region of IR spectrum, this mode has not been observed. Unlike interstitial H (H_i), H_O is stable, with calculated migration energy of 1.7 eV (Bang and Chang, 2008). This makes it a strong candidate for H-related donors in as-grown ZnO (Hoffman et al., 2002). A PL line at 3.362 eV, labeled I_4 in literature and attributed to an exciton bound to a hydrogen donor (Meyer et al., 2004), was tentatively identified with H_O (Lavrov et al., 2009).

6.2 CVT growth of polycrystalline ZnO with impurities

To investigate the possibility that hydrogen-related defects are associated with an impurity or impurities, I incorporated small amounts of various impurities into the crystal growth of bulk ZnO by chemical vapor transport. The impurities include CaO, Ca, SrO, MgO, and Mg. I carried out post-growth annealing in hydrogen at 700°C. Following hydrogenation, I obtained the IR spectrum at 10 K. All samples, including a reference (no additional impurity), showed the Lavrov peak at 3611 cm^{-1} (Fig. 6.1). The McCluskey peak was not observed. Since we do not have evidence of the incorporation of these impurities into the crystal, we cannot make a conclusive statement of their behavior.

It has been shown theoretically that hydrogen at the bond center site (Lavrov defect) has lower formation energy than the other sites (Lavrov et al., 2002; Limpijumnong and Zhang, 2005). This may explain the observation of the Lavrov peak in the grown samples, along with the attribution to the growth technique. We note that Eagle-Picher samples, which are grown by CVT, exhibit a strong Lavrov peak.

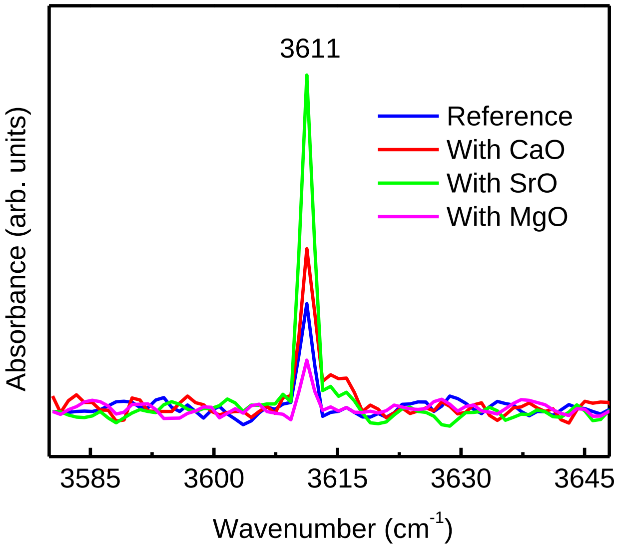

Figure 6.1: Hydrogen-related absorption peak at 3611 cm^{-1} (Lavrov peak) in various CVT-grown ZnO samples. The difference in intensities can be attributed to variations in thickness of the polycrystalline growth.

An absorption peak at 3147 cm^{-1} at room temperature (~3151 cm^{-1} at 10 K), which is the IR signature of N-H complex, was also observed initially when Mg was incorporated. Apparently there was no clear indication that the addition of Mg facilitated the doping of N into the crystal. This N contamination seemed to occur randomly in various growths. We also observe it in our reference samples grown in Ar. The origin or mechanism of this unintentional N doping remains to be determined.

6.3 Zinc-annealed Cermet sample

A sample from Cermet Inc. was annealed in zinc vapor to produce oxygen vacancies. The sample was placed in a fused silica ampoule (10 cm long and 1.7 cm inner diameter) along with 1.6 g Zn metal. The ampoule was evacuated and a torch was passed around it to remove water and other contaminants. The torch was then used to seal the ampoule while maintaining the vacuum inside. The sealed ampoule was placed in the furnace and annealed at 1100°C for 30 min. Zinc metal vaporizes at approximately 1179 K (906°C). At the end of the annealing it was quickly removed from the furnace and allowed to cool to room temperature. The surface damage produced during the anneal was eliminated by polishing with aluminum oxide polishing film.

Figure 6.2 displays the image of the sample before and after Zn annealing. The reddish color of the Zn-annealed sample was attributed to the formation of oxygen vacancies (Halliburton et al., 2005; Selim et al., 2007). Before performing Zn annealing, Hall effect and IR absorption measurements were obtained at room temperature. The as-received sample had an electron concentration of 1.2 x 10^{17} cm^{-3}. After Zn annealing, the carrier concentration increased significantly (Fig. 6.3), consistent with the IR spectrum showing stronger free carrier absorption (Fig. 6.4). Either Zn interstitials or oxygen vacancies are responsible for the increase in free carriers. Positron annihilation study of Zn-annealed ZnO crystal (Selim et al., 2007) challenges the possibility of Zn interstitials causing *n*-type conductivity.

The Zn-annealed sample was subsequently annealed in hydrogen at 700°C. A further increase in free carrier density and absorption was observed (Figs. 6.3 and 6.4a), suggesting a correlation between hydrogen and increase in free carriers. It is posited that the hydrogen may have occupied the oxygen vacancies, consistent with the suggested substitutional hydrogen being a donor (Janotti and Van de Walle, 2007). Because of the strong free carrier absorption, no absorption peaks were detectable in the lower energy region of the IR spectra where the calculated vibrational frequency of H_O is located.

Whereas the McCluskey peak has a strong intensity in the hydrogenated Cermet sample (Fig. 6.4b), it was not observed in the hydrogenated Zn-annealed sample. Whether this could provide support for the V_{Zn} – H model for the McCluskey defect requires a further investigation.

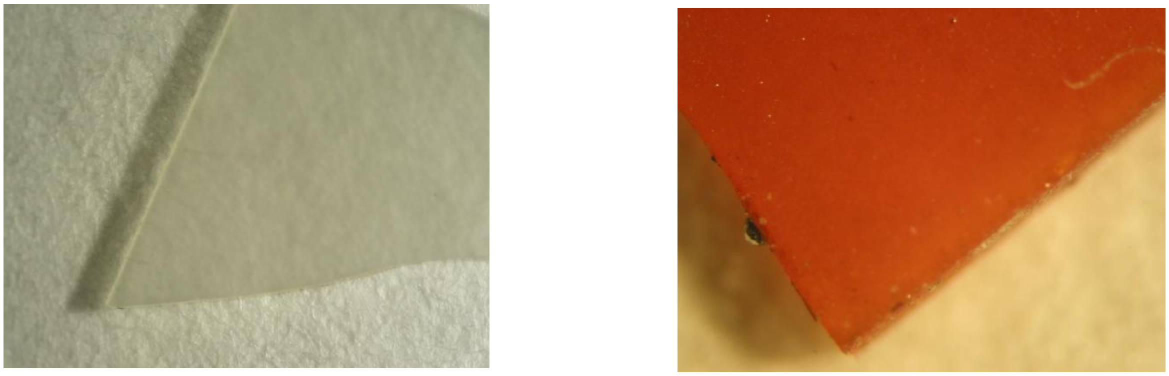

As-received

Zn annealed

Figure 6.2: Cermet sample before and after Zn annealing.

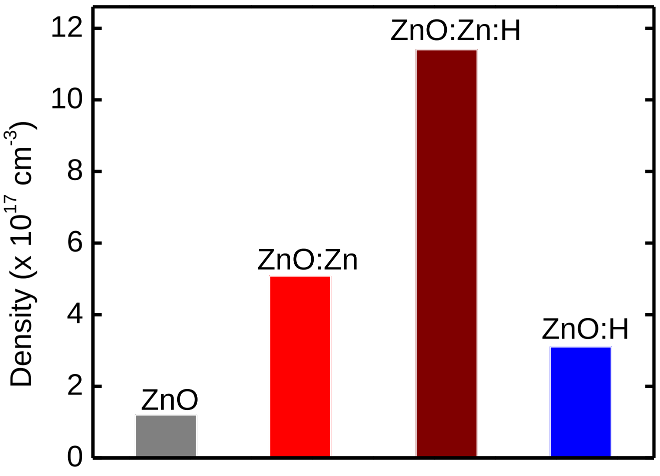

Figure 6.3: Electron density of the Cermet sample before and after annealing in various conditions.

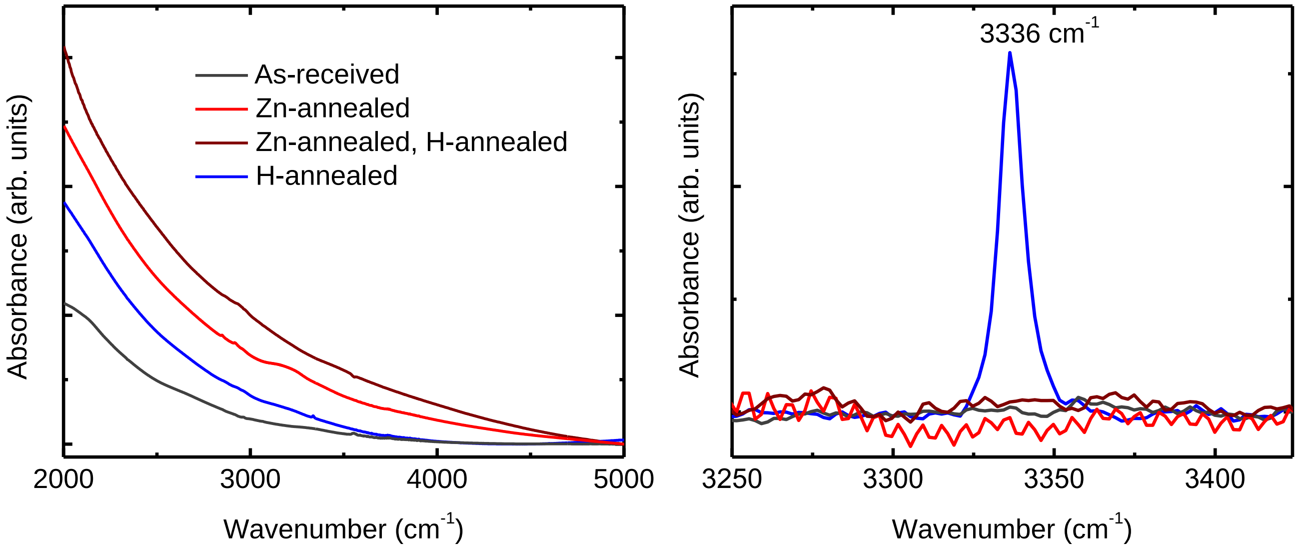

(a) (b)

Figure 6.4: (a) IR absorption spectra of the as-received and annealed Cermet samples. (b) Baseline of the IR spectra in the region of the McCluskey peak.

CHAPTER 7 SUMMARY AND CONCLUSIONS

I have dealt with two important issues related to dopants and defects in oxides: the nitrogen acceptor in ZnO, which has been a subject of hundreds of studies focused on *p*-type doping; and the hydrogen-related defects in $SrTiO_3$.

In ZnO, we have shown experimental evidence that nitrogen is a deep acceptor. Broad red photoluminescence exhibited by N-doped samples is correlated with N_O acceptors. PL and PLE studies associated with N_O acceptors show optical absorption and emission energies of 2.2 and 1.7 eV, respectively. These results are in agreement with the nitrogen deep acceptor model by Lyons, Janotti and Van de Walle (2009) that suggests an acceptor level of 1.3 eV above the valence band maximum. A near band-edge PL associated with N_O acceptors is tentatively assigned to an exciton bound to nitrogen deep acceptor with a binding energy of 0.11 eV. The deep-acceptor behavior of nitrogen may be attributed to the intrinsic feature of ZnO in which the position of its valence band relative to the vacuum level is rather low, thus making nitrogen a deep acceptor. Our findings will preclude the role of nitrogen as a *p*-type dopant in ZnO and may stimulate the redirection of research efforts in investigating alternative sources of *p*-type conduction in ZnO.

In $SrTiO_3$, we have identified and characterized a new hydrogen-related defect. A proposed model of the defect consists of a strontium vacancy passivated by two hydrogen atoms. Furthermore, we suggest the presence of hidden hydrogen species in $SrTiO_3$ in the form of H_2 molecules. When linked with prior work on hydrogen in ZnO, our work suggests a universal behavior of hydrogen across a range of oxide materials. These findings are important not only for fundamental scientific interest but are also crucial for understanding processes in device technology involving oxide materials.

CHAPTER 8 FUTURE WORK RECOMMENDATIONS

Clearly, there is a need to investigate an alternative approach to achieve *p*-type conductivity in ZnO. A possible route involves tuning the valence band to attain a reduced nitrogen binding energy, possibly through alloying. Another promising avenue of research is to explore an alternative wide-band gap material. Recent theoretical work (Singh et al. 2008) shows excellent prospects for *p*-type doping in SnO_2, indicating that it may be a better choice for light emitters and other optoelectronic applications.

In $SrTiO_3$, a systematic experimental study of various samples may be performed to establish strong correlation between IR absorption study of H-related defects and positron annihilation measurements.

CHAPTER 9 APPENDIX

9.1 CVT crystal growth runs

In a chemical vapor transport (CVT) process, a temperature gradient is used to achieve mass transport which occurs through chemical reaction between the source material and a transport agent. Initial CVT growths of ZnO were carried out in an old horizontal tube furnace with a natural temperature gradient. The current through the heating elements is controlled by an Adjust-a-Volt variable transformer. A polycrystalline growth of ZnO crystal was obtained with a source temperature of 950°C. The natural temperature gradient of the furnace left the growth end of the ampoule at a temperature of ~870°C. A 1.5-g ZnO aggregate, 2.0-g high-purity graphite, and ½ atm of Ar as ambient gas were used. The crystal had a light orange color. When a crystal was grown with a small amount of Zn metal added (.01 to .02 g), it took a deep orange color. The first attempt at growing polycrystalline ZnO with Ca (using $CaCO_3$) was also performed in this old furnace. The crystal had what looked like metallic droplets (possibly Zn metal) on the surface.

In early 2008, we started to perform our CVT growth experiments in a new programmable three-zone horizontal tube furnace (Mellen TV12.5-4X12-3Z with maximum operating temperature of 1300°C). Several runs were carried out to determine the desirable temperature settings for crystal growth with this new furnace. In all these trial runs we kept the same amount of ZnO aggregate (1.5 g) and high-purity graphite (2.0 g). We note that during the growth, there is an increase in gas pressure inside the ampoule. While the ampoule is able to handle the large pressure, it has a tendency to explode during the cool down phase of the growth process due to the thermal mismatch between the crystal and the ampoule wall. The explosion could be avoided by controlling the cooling rate in the initial phase of the cooling process. The ZnO crystal samples used in this work were obtained with growth runs where the two adjacent zones (1 and 2) of the furnace were held at the same temperature 1000°C, corresponding to the source temperature. Zone 3, corresponding to the deposition end, was set to 880 - 900°C. The source end approximately lined up with zone 2. Adjacent zones are 4 inches (10.16 cm) apart. Thus, the sealed ampoule is normally prepared to an effective length 4 inches. The rest of the polycrystalline growth of ZnO with various impurities (Sec. 6.2) and the seeded growth of N-doped ZnO samples (Sec. 4.2) were carried out in this furnace. Samples are typically 1.5 to 2 mm thick for growth duration of three days.

Attempts were also made to grow ZnO using different chemical as transport agent. Growth using H_2 as a carrier gas resulted in a very thin colorless layer. With CO_2, a crystal growth hardly occurred even with prolonged soaking. With NH_3, a noticeable crystal was produced with lighter color than the one grown with graphite. A very weak IR absorption peak at 3147 cm^{-1}, which is an N-H peak, at room temperature was observed.

CHAPTER 10 PUBLICATIONS RESULTING FROM THIS WORK

1. M.D. McCluskey, S.J. Jokela, and M.C. Tarun, "Hydrogen-related defects in bulk ZnO," in Compound Semiconductors for Energy Applications and Environmental Sustainability, ed. F. Shahedipour-Sandvik, E.F. Schubert, L.D. Bell, V. Tilak, A.W. Bett. *Mater. Res. Soc. Symp. Proc.* **1167**, 1167-O07-07 (2009).

2. S.J. Jokela, M.C. Tarun, and M.D. McCluskey, "Nitrogen and hydrogen in bulk single-crystal ZnO," *Physica B* **404**, 4810-2 (2009).

3. M.C. Tarun and M.D. McCluskey, "Infrared absorption of hydrogen-related defects in strontium titanate," *J. Appl. Phys.* **109**, 063706:1-4 (2011).

4. M.C. Tarun, M. Zafar Iqbal, and M.D. McCluskey, "Nitrogen is a deep acceptor in ZnO," *AIP Advances* **1**, 022105:1-7 (2011).

5. M.C. Tarun, M. Zafar Iqbal, M.D. McCluskey, J. Huso, and L. Bergman, "Experimental evidence for nitrogen as a deep acceptor in ZnO," *MRS Proceedings* **1394**, mrsf11-1394-m01-06 (2012).

BIBLIOGRAPHY

Ahn, C. H., J.-M. Triscone, and J. Mannhart. 2003. Electric field effect in correlated oxide systems. *Nature* 424: 1015 – 1018.

Ashtiani, S.J., and A. Nathan. 2009. A driving scheme for active-matrix organic light-emitting diode displays based on current feedback. *J. Display Technol.* 5: 257-264.

Bang, J., and K. J. Chang. 2008. Diffusion and thermal stability of hydrogen in ZnO. *Appl. Phys. Lett.* 92: 132109 (3 pages).

Baer, W.S. 1966. Free-carrier absorption in reduced $SrTiO_3$. *Phys. Rev.* 144: 734 – 738.

Bardeen, J., and W.H. Brattain. 1948. The transistor, a semiconductor triode. *Phys. Rev.* 74: 230–231.

Barker, A.S. Jr., and A.J. Sievers. 1975. Optical studies of the vibrational properties of disordered solids. *Rev. Mod. Phys.* 47: S1-179.

Barnes, T. M., K. Olsen, and C. A. Wolden. 2005. On the formation and stability of *p*-type conductivity in nitrogen-doped zinc oxide. *Appl. Phys. Lett.* 86: 112112 (3 pages).

Barrett, J. H. 1952. Dielectric constant in perovskite type crystals. *Phys. Rev.* 86: 118 – 120.

Bednorz, J.G., and Müller, K.A. 1986. Possible high T_c superconductivity in the Ba-La-Cu-O system. *Z. Phys. B: Condens. Matter* 64: 189 – 193.

Bell, R.J. 1972. *Introductory Fourier Transform Spectroscopy*. New York: Academic Press.

Bi, C. Z., J. Y. Ma, J. Yan, X. Fang, B. R. Zhao, D. Z. Yao, and X. G. Qiu. 2006. Electron–phonon coupling in Nb-doped $SrTiO_3$ single crystal. *J. Phys.: Condens. Matter* 18: 2553 – 2561.

Bierwagen, O., T. Ive, C. G. Van de Walle, and J. S. Speck. 2008. Causes of incorrect carrier-type identification in van der Pauw–Hall measurements. *Appl. Phys. Lett.* 93: 242108 (3 pages).

Cabrera, J.M., J. Olivares, M. Carrascosa, J. Rams, R. Müller, and E. Dieguez. 1996. Hydrogen in lithium niobate. *Advances in Physics* 45: 349-392.

Carlos, W.E., E.R. Glaser, and D.C. Look. 2001. Magnetic resonance studies of ZnO. *Physica B* 308–10: 976–979.

Cermet Inc., http://www.cermetinc.com

Chai, J., R. J. Mendelsberg, R. J. Reeves, J. Kennedy, H. von Wenckstern, M. Schmidt, M. Grundmann, K. Doyle, T. H. Myers and S. M. Durbin. 2010. Identification of a deep acceptor level in ZnO due to silver doping. *Journal of Electronic Materials* 39: 577 – 583.

Chen, Y., D.M. Bagnall, H.-J. Koh, K.-T. Park, K. Hiraga, Z.-Q. Zhu, and T. Yao. 1998. Plasma assisted molecular beam epitaxy of ZnO on *c* -plane sapphire: Growth and characterization. *J. Appl. Phys.* 84: 3912 – 3918.

Christen, H.-M., J. Mannhart, E. J. Williams, and Ch. Gerber. 1994. Dielectric properties of sputtered $SrTiO_3$ films. *Phys. Rev. B* 49: 12095 – 12104.

Clarke, D. R. 1999. Varistor ceramics. *J. Am. Ceram. Soc.* 82: 485 – 502.

Clement, M., J. M. M. de Nijs, P. Balk, H. Schut, and A. van Veen. 1996. Analysis of positron beam data by the combined use of the shape- and wing-parameters. *J. Appl. Phys.* 79: 9029 – 9036.

Connes, J., and P. Connes. 1966. Near-infrared planetary spectra by Fourier spectroscopy. I. Instruments and results. *J. Opt. Soc. Am.* 56: 896–910.

Cox, S. F. J., E. A. Davis, S. P. Cottrell, P. J. C. King, J. S. Lord, J. M. Gil, H. V. Alberto, R. C. Vilao, J. P. Duarte, N. A. de Campos, A. Weidinger, R. L. Lichti, and S. J. C. Irvine. 2001. Experimental confirmation of the predicted shallow donor hydrogen state in zinc oxide. *Phys. Rev. Lett.* 86: 2601–2604.

Dean, P.J. 1982. Photoluminescence as a diagnostic of semiconductors. *Progress in Crystal Growth and Characterization* 5: 89–174.

Duan, X. M., C. Stampfl, M. M. M. Bilek, D. R. McKenzie, and S.-H. Wei. 2010. Design of shallow acceptors in ZnO through early transition metals codoped with N acceptors. *Phys. Rev. B* 83: 085202 (8 pages).

Eaglesham, D. J., F. C. Unterwald, H. Luftman, D. P. Adams, and S. M. Yalisove. 1993. Effect of H on Si molecular-beam epitaxy. *J. Appl. Phys.* 74: 6615 – 6618.

Eblen-Zayas, M., A. Bhattacharya, N. E. Staley, A. L. Kobrinskii, and A. M. Goldman. 2005. Ambipolar gate effect and low temperature magnetoresistance of ultrathin $La_{0.8}Ca_{0.2}MnO_3$ films. *Phys. Rev. Lett.* 94: 037204 (4 pages).

Eckstein, J. N. and I. Bozovic. 1995. High-temperature superconducting multilayers and heterostructures grown by atomic layer-by-layer molecular beam epitaxy. *Annu. Rev. Mater. Sci*. 25: 679 – 709.

Elliot, R. J., W. Hayes, G. D. Jones, H. F. MacDonald, and C. T. Sennet. 1965. Localized vibrations of H^- and D^- ions in the alkaline earth fluorides. *Proc. R. Soc. Lond. A* 289:1–33.

Eror, N. G., and U. Balachandran. 1982. High-temperature defect structure of acceptor-doped strontium titanate. *J. Am. Ceram. Soc.* 65: 426 – 431.

Fagg, D., V. Kharton, A. Kovalevsky, A. Viskup, E. Naumovich, and J. Frade. 2001. The stability and mixed conductivity in La and Fe doped $SrTiO_3$ in the search for potential SOFC anode materials. *J. Eur. Ceram. Soc.* 21: 1831 – 1835.

Fellgett, P. 1958. A contribution to the theory of the multiplex interferometric spectrometer. *J. Phys. Radium* 19: 187 – 191.

Ferreira, A., J. Abrantes, J. Jurado, and J. Frade. 2000. Oxygen stoichiometry of $Sr_{0.97}(Ti,Fe)_{O3-\delta}$ materials. *Solid State Ionics* 135: 761 – 764.

Fix, T., R. Bali, N. Stelmashenko, and M. Blamire. 2008. Influence of the dopant concentration in In-doped $SrTiO_3$ on the structural and transport properties. *Solid State Commun.* 146: 428 – 430.

Fons, P., H. Tampo, A.V. Kolobov, M. Ohkubo, S. Niki, J. Tominaga, R. Carboni, F. Boscherini, and S. Friedrich. 2006. Direct observation of nitrogen location in molecular beam epitaxy grown nitrogen-doped ZnO. *Phys. Rev. Lett.* 96: 045504 (4 pages).

Fons, P., K. Iwata, S. Niki, A. Yamada, and K. Matsubara. 1999. Growth of high-quality epitaxial ZnO films on alpha-Al_2O_3. *J. Crystal Growth* 201/202: 627-632.

Frederikse, H. P. R, W. R. Thurber, and W. R. Holser. 1964. Electronic transport in strontium titanate. *Phys. Rev*. 134: A442-A445.

Fuchs, D. C., W. Schneider, R. Schneider, and H. Rietschel. 1999. High dielectric constant and tunability of epitaxial $SrTiO_3$ thin film capacitors. *J. Appl. Phys.* 85: 7362 (8 pages).

Garces, N. Y., L. Wang, N. C. Giles, L. E. Halliburton, G. Cantwell, and D. B. Eason. 2003. Molecular nitrogen (N_2^-) acceptors and isolated nitrogen (N^-) acceptors in ZnO crystals. *J. Appl. Phys.* 94: 519 – 524.

Garces, N. Y., N. C. Giles, L. E. Halliburton, G. Cantwell, D. B. Eason, D. C. Reynolds, and D. C. Look. 2002. Production of nitrogen acceptors in ZnO by thermal annealing. *Appl. Phys. Lett.* 80: 1334 (3 pages).

Gasiorowicz, S. 1996. *Quantum Physics*, 2nd ed. New York: John Wiley & Sons.

Gentils, A., O. Copie, G. Herranz, F. Fortuna, M. Bibes, K. Bouzehouane, É. Jacquet, C. Carrétéro, M. Basletić, E. Tafra, A. Hamzić, and A. Barthélémy. 2010. Point defect distribution in high-mobility conductive $SrTiO_3$ crystals. *Phys. Rev. B* 81: 144109 (9 pages).

Gervais, F., J. L. Servoin, A. Baratoff, J. G. Bednorz, and G. Binnig. 1993. Temperature dependence of plasmons in Nb-doped $SrTiO_3$. *Phys. Rev. B* 47: 8187 – 8194.

Gil, J. M., H. V. Alberto, R. C. Vilao, J. P. Duarte, N. A. de Campos, A. Weidinger, J. Krauser, E. A. Davis, and S. F. J. Cox. 2001. Shallow donor muonium states in II-VI semiconductor compounds. *Phys. Rev. B* 64: 075205 (8 pages).

Gilliland, G.D. 1997. Photoluminescence spectroscopy of crystalline semiconductors. *Materials Science and Engineering: R: Reports* 18: 99 – 400.

Glaser, E. R., W. E. Carlos, G. C. B. Braga, J. A. Freitas, Jr., W. J. Moore, B. V. Shanabrook, R. L. Henry, A. E. Wickenden, D. D. Koleske, H. Obloh, P. Kozodoy, S. P. DenBaars, and U. K. Mishra. 2002. Magnetic resonance studies of Mg-doped GaN epitaxial layers grown by organometallic chemical vapor deposition. *Phys. Rev. B* 65: 085312 (10 pages).

Gopalan, S., C.-H. Wong, V. Balu, J.-H. Lee, J. H. Han, R. Mohammedali, and J. C. Lee. 1999. Effect of niobium doping on the microstructure and electrical properties of strontium titanate thin films for semiconductor memory application. *Appl. Phys. Lett.* 75: 2123 (3 pages).

Gordon, R. G. 2000. Criteria for choosing transparent conductors. *MRS Bull.* 25: 52 – 57.

Gröne, A., M. Wöhlecke, S. Kapphan, and R. Waser. 1990. High resolution IR absorption spectroscopy of the OH stretch modes in $SrTiO_3$:Fe. *Ferroelectrics* 107: 97 – 102.

Haller, E.E. 1995. Local vibrational mode (LVM) spectroscopy of semiconductors. *Mater. Res. Soc. Symp. Proc.* 378:547–565.

Halliburton, L. E., N. C. Giles, N.Y. Garces, Ming Luo. Chunchuan Xu, Lihai Bai, and L.A. Boatner. 2005. Production of native donors in ZnO by annealing at high temperature in Zn vapor. *Appl. Phys. Lett.* 87:172108 (3 pages).

Hamby, D. W., D. A. Lucca, M. J. Klopfstein, and G. Cantwell. 2003. Temperature dependent exciton photoluminescence of bulk ZnO. *J. Appl. Phys.* 93: 3214 – 3217.

Haynes, J.R. 1960. Experimental proof of the existence of a new electronic complex in silicon. *Phys. Rev. Lett.* 4: 361 – 363.

Hemberger, J., P. Lunkenheimer, R. Viana, R. Böhmer and A. Loidl. 1995. Electric-field-dependent dielectric constant and nonlinear susceptibility in $SrTiO_3$. *Phys. Rev. B* 52: 13159-13162.

Hofmann, D. M., A. Hofstaetter, F. Leiter, H. J. Zhou, F. Henecker, B. K. Meyer, S. B. Orlinskii, J. Schmidt, and P. G. Baranov. 2002. Hydrogen: A relevant shallow donor in zinc oxide. *Phys. Rev. Lett.* 88: 045504 (4 pages).

Houde, D., Y. Lépine, C. Pépin, S. Jandl and J. L. Brebner. 1987. High-resolution infrared spectroscopy of hydrogen impurities in strontium titanate. *Phys. Rev. B* 35: 4948 – 4953.

Hwang, C. S., S. O. Park, C. S. Kang, H.-J. Cho, H.-K. Kang, S.T. Ahn, and M. Y. Lee. Deposition and electrical characterization of very thin $SrTiO_3$ films for ultra large scale integrated dynamic random access memory application. 1995. *Jpn. J. Appl. Phys.* 34, 5178 – 5183.

Iwata, K., P. Fons, A. Yamada, K. Matsubara, and S. Niki. 2000. Nitrogen-induced defects in ZnO:N grown on sapphire substrate by gas source MBE. *J. Cryst. Growth* 209: 526 – 531.

Jacquinot, P. 1960. New developments in interference spectroscopy. *Rep. Prog. Phys.* 23: 267-312.

Jalan, B., R. Engel-Herbert, T. Mates, and S. Stemmer. 2008. Effects of hydrogen anneals on oxygen deficient $SrTiO_{3-x}$ single crystals. *Appl. Phys. Lett.* 93: 052907 (3 pages).

Jalan, B., R. Engel-Herbert, N. J. Wright, and S. Stemmer. 2009. Growth of high-quality $SrTiO_3$ films using a hybrid molecular beam epitaxy approach. *J. Vac. Sci. Technol. A* 27: 461 – 464.

Janotti, A., and C. G. Van de Walle. 2007a. Hydrogen multicentre bonds. *Nature Mater.* 6: 44 – 47.

Janotti, A., and C. G. Van de Walle. 2007b. Native point defects in ZnO. *Phys. Rev. B* 76: 165202 (22 pages).

Janotti, A., and C. G. Van de Walle. 2011. LDA+*U* and hybrid functional calculations for defects in ZnO, SnO_2, and TiO_2. *Phys. Status Solidi B* 248: 799–804.

Jarzębski, Z. M. 1973. *Oxide Semiconductors*. New York:Pergamon Press. 14 – 17.

Jeong, J. K. 2011. The status and perspectives of metal oxide thin-film transistors for active matrix flexible displays. *Semicond. Sci. Technol.* 26: 034008 (10 pages).

Jin, S., T. H. Tiefel, M. McCormack, R. A. Fastnacht, R. Ramesh, and L. H. Chen. 1994. Thousandfold change in resistivity in magnetoresistive La-Ca-Mn-O films. *Science* 264: 413 – 415.

Jokela, S. J. and M. D. McCluskey. 2010. Structure and stability of N–H complexes in single-crystal ZnO. *J. Appl. Phys.* 107: 113536 (5 pages).

Jokela, S. J. and M.D. McCluskey. 2007. Hydrogen complexes in ZnO grown by chemical vapor transport. *Physica B: Condensed Matter* 401-402: 395 – 398.

Jokela, S. J., and M.D. McCluskey. 2005. Structure and stability of O-H donors in ZnO from high-pressure and infrared spectroscopy. *Phys. Rev. B* 72: 113201 (4 pages).

Jokela, S. J., M. C. Tarun and M. D. McCluskey. 2009. Nitrogen and hydrogen in bulk single-crystal ZnO. *Physica B* 404: 4810-4812.

Kan, D, Takahito Terashima, Ryoko Kanda, Atsunobu Masuno, Kazunori Tanaka, Shucheng Chu, H Kan, et al. 2005. Blue-light emission at room temperature from Ar+-irradiated $SrTiO_3$. *Nature Mater.* 4: 816 – 819.

Kanai, Y., 1991a. Admittance spectroscopy of copper-doped zinc oxide crystals. *Jpn. J. Appl. Phys. Part 1, Regul. Pap. Short Notes* 30: 703 – 707.

Kanai, Y., 1991b. Admittance spectroscopy of zinc oxide crystals containing silver. *Jpn. J. Appl. Phys. Part 1, Regul. Pap. Short Notes* 30: 2021 -2022.

Kasuga, M., and S. Ogawa. 1983. Electronic properties of vapor-grown heteroepitaxial ZnO film on sapphire. *Jpn. J. Appl. Phys.* 22: 794 – 798.

Kawasaki, M., K. Takahashi, T. Maeda, R. Tsuchiya, M. Shinohara, O. Ishiyama, T. Yonezawa, M. Yoshimoto, and H. Koinuma. 1994. Atomic control of the $SrTiO_3$ crystal surface. *Science* 266: 1540 – 1542.

Keeble, D. J., R. A. Mackie, W. Egger, B. Löwe, P. Pikart, C. Hugenschmidt, and T. J. Jackson. 2010. Identification of vacancy defects in a thin film perovskite oxide. *Phys. Rev. B* 81: 064102 (5 pages).

Kılıç, Ç., and A. Zunger. 2002. *n*-type doping of oxides by hydrogen. *Appl. Phys. Lett.* 81: 73 – 75.

Kim, K.-K., J.-H. Song, H.-J. Jung, W.-K. Choi, S.-J. Park, and J.-H. Song. 2000. The grain size effects on the photoluminescence of ZnO/α-Al_2O_3 grown by radio-frequency magnetron sputtering. *J. Appl. Phys.* 87: 3573 - 3575.

Kittel, C. 2005. *Introduction to Solid State Physics*, 8th ed. Hoboken, N.J.: John Wiley & Sons.

Klauer, S. and M. Wöhlecke. 1992. Local symmetry of hydrogen in cubic and tetragonal $SrTiO_3$ and $KTaO_3$:Li determined by polarized Raman scattering. *Phys. Rev. Lett.* 68: 3212–3215.

Klingshirn, C. 2007. ZnO: From basics towards applications. *Phys. Stat. Sol. (b)* 244: 3027–3073.

Kobayashi, A., O.F. Sankey, and J.D. Dow. 1983. Deep energy levels of defects in the wurtzite semiconductors AIN, CdS, CdSe, ZnS, and ZnO. *Phys. Rev. B* 28: 946 – 956.

Koster, G., B. L. Kropman, G. J. H. M. Rijnders, D. H. A. Blank, and H. Rogalla. 1998. Quasi-ideal strontium titanate crystal surfaces through formation of strontium hydroxide. *Appl. Phys. Lett.* 73: 2920 (3 pages).

Krtschil, A., D. C. Look, Z.-Q. Fang, A. Dadgar, A. Diez, and A. Krost. 2006. Local *p*-type conductivity in n-GaN and n-ZnO layers due to inhomogeneous dopant incorporation. *Physica B* 376: 703 – 706.

Lang, D.V., and R.A. Logan. 1977. Large-lattice-relaxation model for persistent photoconductivity in compound semiconductors. *Phys. Rev. Lett.* 39: 635–639.

Lany, S., and A. Zunger. 2010. Generalized Koopmans density functional calculations reveal the deep acceptor state of N_O in ZnO. *Phys. Rev. B* 81: 205209 (5 pages)

Lavrov, E. V., F. Börrnert, and J. Weber. 2005. Photoconductivity and infrared absorption study of hydrogen-related shallow donors in ZnO. *Phys. Rev. B* 72, 085212 (8 pages).

Lavrov, E. V., F. Börrnert, and J. Weber. 2007. Hydrogen motion in ZnO. *Physica B* 401–402: 366–369.

Lavrov, E.V., F. Herklotz, and J. Weber. 2009. Identification of hydrogen molecules in ZnO. *Phys. Rev. Lett.* 102: 185502 (4 pages).

Lavrov, E.V., J. Weber, F. Börrnert, C.G. Van de Walle, and R. Helbig. 2002. Hydrogen-related defects in ZnO studied by infrared absorption spectroscopy. *Phys. Rev. B* 66: 165205 (7 pages).

Lee, E.-C., and K. J. Chang. 2004. Possible p-type doping with group-I elements in ZnO. *Phys. Rev. B* 70: 115210 (4 pages).

Lee, E.-C., Y.-S. Kim, Y.-G. Jin, and K. J. Chang. 2001. Compensation mechanism for N acceptors in ZnO. *Phys. Rev. B* 64: 085120 (5 pages).

Lee, W. J., J. Kang, and K. J. Chang. 2006. Defect properties and *p*-type doping efficiency in phosphorus-doped ZnO. *Phys. Rev. B* 73: 024117 (6 pages).

Lewis, B.G. and D.C. Paine. 2000. Applications and processing of transparent conducting oxides. *MRS Bull.* 25: 22 – 27.

Li, L., C. X. Shan, B. H. Li, B. Yao, J. Y. Zhang, D. X. Zhao, Z. Z. Zhang, D. Z. Shen, X. W. Fan, and Y. M. Lu. 2008. The compensation source in nitrogen doped ZnO. *J. Phys. D* 41: 245402 (4 pages).

Li, X., S. Limpijumnong, W.Q. Tian, H.B. Sun, S.B. Zhang. 2008. Hydrogen in ZnO revisited: Bond center versus antibonding site. *Phys. Rev. B* 78: 113203 (4 pages).

Liang, H. W., Y. M. Lu, D. Z. Shen, Y. C. Liu, J. F. Yan, C. X. Shan, B. H. Li, Z. Z. Zhang, J. Y. Zhang, and X. W. Fan. 2005. P-type ZnO thin films prepared by plasma molecular beam epitaxy using radical NO. *Phys. Status Solidi A* 202: 1060 – 1065.

Limpijumnong, S., and S. B. Zhang. 2005. Resolving hydrogen binding sites by pressure—A first-principles prediction for ZnO. *Appl. Phys. Lett.* 86: 151910 (3 pages).

Limpijumnong, S., X. Li, S.-H. Wei, and S. B. Zhang. 2005. Substitutional diatomic molecules NO, NC, CO, N_2, and O_2: Their vibrational frequencies and effects on *p*-doping of ZnO. *Appl. Phys. Lett.* 86: 211910 (3 pages).

Lin, C.-C., S. Y. Chen, S. Y. Cheng, and H. Y. Lee. 2004. Properties of nitrogen-implanted *p*-type ZnO films grown on Si_3N_4/Si by radio-frequency magnetron sputtering. *Appl. Phys. Lett.* 84: 5040 (3 pages).

Linsebigler, A. L., G. Lu, and J. T. Yates, Jr. 1995. Photocatalysis on TiO_2 surfaces: Principles, mechanisms, and selected results. *Chem. Rev.* 95: 735 – 758.

Liu, Y., C. R. Gorla, S. Liang, N. Emanetoglu, Y. Lu, H. Shen, and M. Wraback. 2000. Ultraviolet detectors based on epitaxial ZnO films grown by MOCVD. *J. Electron. Mater.* 29: 69 – 74.

Look, D. C. 2001. Recent advances in ZnO materials and devices. *Mater. Sci. Eng. B* 80: 383 – 387.

Look, D. C., B. Claflin, Ya. I. Alivov, and S. J. Park. 2004. The future of ZnO light emitters. *Phys. Status Solidi A* 201: 2203-2212

Look, D.C., D.C. Reynolds, C.W. Litton, R.L. Jones, D.B. Eason, and G. Cantwell. 2002. Characterization of homoepitaxial *p*-type ZnO grown by molecular beam epitaxy. *Appl. Phys. Lett.* 81: 1830 – 1832.

Look, D.C., D.C. Reynolds, J. R. Sizelove, R. L. Jones, C. W. Litton, G. Cantwell, and W. C. Harsch. 1998. Electrical properties of bulk ZnO. *Solid State Communications* 105: 399-401.

Lyons, J.L., A. Janotti, and C.G. Van de Walle. 2009. Why nitrogen cannot lead to *p*-type conductivity in ZnO. *Appl. Phys. Lett.* 95: 252105 (3 pages).

Mackie, R., S. Singh, J. Laverock, S. Dugdale and D. Keeble. 2009. Vacancy defect positron lifetimes in strontium titanate. *Phys. Rev. B* 79: 014102 (8 pages).

Maeda, K., M. Sato, I. Niikura, and T. Fukuda. 2005. Growth of 2-inch ZnO bulk single crystal by the hydrothermal method. *Semicond. Sci. Technol.* 20: S49 – S54.

MaTecK GmbH, http://www.mateck.de

Matsui, H., H. Saeki, T. Kawai, H. Tabata, and B. Mizobuchi. 2004. N doping using N_2O and NO sources: From the viewpoint of ZnO. *J. Appl. Phys.* 95: 5882

Matsumoto, K., and K. Noda. 1990. Crystal growth of ZnO by chemical transport using $HgCl_2$ as a transport agent. *J. Cryst. Growth* 102: 137 – 140.

McCluskey, M. D., and S. J. Jokela. 2007. Sources of n-type conductivity in ZnO. *Physica B* 401–402: 355–357.

McCluskey, M. D., S. J. Jokela, K. K. Zhuravlev, P. J. Simpson, and K. G. Lynn. 2002. Infrared spectroscopy of hydrogen in ZnO. *Appl. Phys. Lett.* 81: 3807 (3 pages).

McCluskey, M. D. 2000. Local vibrational modes of impurities in semiconductors. *J. Appl. Phys.* 87: 3593–3617.

McCluskey, M.D., and E. E. Haller. 1999. Hydrogen in III-V and II-V semiconductors. In *Semiconductors and Semimetals* Vol. 61, ed. N.H. Nickel, 373–340. San Diego: Academic Press.

McCluskey, M. D., and E. E. Haller. 2012. *Dopants and Defects in Semiconductors*. Boca Raton, FL: CRC Press (Taylor & Francis Group).

McCluskey, M. D., and S. J. Jokela. 2009. Defects in ZnO. *J. Appl. Phys.* 106: 071101:1–13.

McCluskey, M. D., E. E. Haller, J. Walker, and N. M. Johnson. 1995. Vibrational spectroscopy of group-II-acceptor−hydrogen complexes in GaP. *Phys. Rev. B* 52:11859−11864.

McGuire, S., D. J. Keeble, R. E. Mason, P. G. Coleman, Y. Koutsonas, and T. J. Jackson. 2006. Variable energy positron beam analysis of vacancy defects in laser ablated $SrTiO_3$ thin films on $SrTiO_3$. *J. Appl. Phys.* 100: 044109 (6 pages).

McHale, J.L. 1999. *Molecular Spectroscopy*, 1st ed. Upper Saddle River, N.J.: Prentice-Hall, Inc.

Mensz, P. M., S. Herko, K. W. Haberern, J. Gaines, and C. Ponzoni. 1993. Electrical characterization of *p*-type ZnSe:N and $Zn_{1-x}Mg_xS_ySe_{1-y}$:N thin films. *Appl. Phys. Lett.* 63: 2800 – 2802.

Meyer, B. K., H. Alves, D. M. Hoffman, W. Kriegseis, D. Forster, F. Bertram, J. Christen, A. Hoffman, M. Strassburg, M. Dworzak, U. Haboeck, and A. V. Rodina. 2004. Bound exciton and donor–acceptor pair recombinations in ZnO. *Phys. Status Solidi* B 241: 231 – 260.

Meyer, B. K., H. Alves, D. M. Hofmann, W. Kriegseis, D. Forster, F. Bertram, J. Christen, A. Hoffmann, M. Straßburg, M. Dworzak, U. Haboeck, and A. V. Rodina. 2004. Bound exciton and donor–acceptor pair recombinations in ZnO. *Phys. Status Solidi B* 241: 231 – 260.

Meyer, B. K., J. Sann, D. M. Hoffman, C. Neumann, and A. Zeuner. 2005. Shallow donors and acceptors in ZnO. *Semicond. Sci. Technol.* 20: S62 – S66.

Minami, T. 2000. New *n*-type transparent conducting oxides. *MRS Bulletin* 25*: 38 – 44.*

Minami, T. 2005. Transparent conducting oxide semiconductors for transparent electrodes. *Semicond. Sci. Technol.* 20: S35–S44.

Minegishi, K., Y. Koiwai, Y. Kikuchi, K. Yano, M. Kasuga, and A. Shimizu. 1997. Growth of *p*-type zinc oxide films by chemical vapor deposition. *Jpn. J. Appl. Phys.* 36: L1453 – L1455.

Mochizuki, S., F. Fujishiro, K. Shibata, A. Ogi, T. Konya, and K. Inaba. 2007. Optical, electrical, and X-ray-structural studies on Verneuil-grown $SrTiO_3$ single crystal: Annealing study. *Physica B* 401 - 402: 433 – 436.

Mollwo, E. 1954. The effect of hydrogen on the conductivity and luminescence of zinc oxide crystals. *Z. Phys.* 138: 478 – 488.

Morito, K., T. Suzuki, S. Sekiguchi, H. Okushu, and M. Fujimoto. 2000. Electrical characterization of $SrTiO_3$ thin films grown on Nb-doped $SrTiO_3$ single crystals. *Jpn. J. Appl. Phys.* 39: 166 – 171.

Morse, P.M. 1929. Diatomic molecules according to wave mechanics. II. Vibrational levels. *Phys. Rev.* 34: 57–64.

Mosbacker, H. L., Y. M. Strzhemechny, B. D. White, P. E. Smith, D. C. Look, D. C. Reynolds, C. W. Litton, and L. J. Brillson. 2005. Role of near-surface states in ohmic-Schottky conversion of Au contacts to ZnO. *Appl. Phys. Lett.* 87: 012102 (3 pages).

MTI Corporation, http://www.mtixtl.com/

Mukunoki, Y., N. Nakagawa, T. Susaki, and H. Y. Hwang. 2005. Atomically flat (110) $SrTiO_3$ and heteroepitaxy. *Appl. Phys. Lett.* 86: 171908 (3 pages).

Müller, K.A., and H. Burkard. 1979. $SrTiO_3$: An intrinsic quantum paraelectric below 4 K. *Phys. Rev. B* 19: 3593-3602.

Mycielski, A., L. Kowalczyk, A. Szadkowski, B. Chwalisz, A.Wysmołek, R. Stępniewski, J.M. Baranowski, M. Potemskic, A.Witowski, R. Jakieła, A. Barcz, B. Witkowska, W. Kaliszek, A.Jędrzejczak, A. Suchocki, E. Łusakowska, and E. Kamińska. 2004. The chemical vapour transport growth of ZnO single crystals. *Journal of Alloys and Compounds* 371: 150-152.

Nan, C-W., M. I. Bichurin, Shuxiang Dong, D. Viehland, and G. Srinivasan. 2008. Multiferroic magnetoelectric composites: Historical perspective, status, and future directions. *J. Appl. Phys.* 103: 031101 (35 pages).

Nause, J. 1999. ZnO broadens the spectrum. *III–Vs Rev.* 12: 28 – 31.

Newman, R.C. 1990. Anharmonic vibrations of hydrogen paired with shallow impurities in semiconductors. *Semicond. Sci. Technol.* 5:911–913.

Norby, T. 2009. *Perovskite Oxides for Solid Oxide Fuel Cells*, ed. T. Ishihara, pp. 217-241. New York: Springer.

Norby, T., M. Widerøe, R. Glöckner and Y. Larring. 2004. Hydrogen in oxides. *Dalton Trans.* 19: 3012 – 3018.

Ntep, J.M., S. Said Hassani, A. Lusson, A. Tromson-Carli, D. Ballutaud, G. Didier and R. Triboulet. 1999. ZnO growth by chemical vapour transport. *Journal of crystal growth* 207: 30–34.

Nuruddin, A., and J. R. Abelson. 2001. Improved transparent conductive oxide/p^+/i junction in amorphous silicon solar cells by tailored hydrogen flux during growth. *Thin Solid Films* 394: 48 – 62.

Ohshima, E., H. Ogino, I. Niikura, K. Maeda, M. Sato, M. Ito, and T. Fukuda. 2004. Growth of the 2-in-size bulk ZnO single crystals by the hydrothermal method. *J. Cryst. Growth* 260: 166 – 170.

Ohta, S., T. Nomura, H. Ohta, and K. Koumoto. High-temperature carrier transport and thermoelectric properties of heavily La- or Nb-doped $SrTiO_3$ single crystals. 2005. *J. Appl. Phys.* 97: 034106 (4 pages)

Ohtomo, A., and H. Y. Hwang. 2004. A high-mobility electron gas at the $LaAlO_3/SrTiO_3$ heterointerface. *Nature* 427: 423–426.

Özgür, Ü., Y.I. Alivov, C. Liu, A. Teke, M.A. Reshchikov, S. Doğan, V. Avrutin, S.-J. Cho and H. Morkoç. 2005. A comprehensive review of ZnO materials and devices. *J. Appl. Phys.* 98: 041301 (103 pages).

Pankove, J.I. 1971. *Optical Processes in Semiconductors*. New York: Dover.

Park, C.H., S.B. Zhang, and S.-H. Wei. 2002. Origin of *p*-type doping difficulty in ZnO: The impurity perspective. *Phys. Rev. B* 66: 073202 (3 pages).

Park, R. M., M. B. Troffer, C. M. Rouleau, J. M. DePuydt, and M. A. Haase. *p*-type ZnSe by nitrogen atom beam doping during molecular beam epitaxial growth. 1990. *Appl. Phys. Lett.* 57: 2127 – 2129.

Pearton, S.J., J.W. Corbett, and M. Stavola. 1992. *Hydrogen in Crystalline Semiconductors*. Berlin: Springer-Verlag.

Perkins, C. L., S. H. Lee, X. N. Lie, S. E. Asher, and T. J. Coutts. 2005. Identification of nitrogen chemical states in N-doped ZnO via x-ray photoelectron spectroscopy. *J. Appl. Phys.* 97: 034907 (7 pages).

Ramesh, R., and D. G. Schlom. 2008. Whither oxide electronics?. *MRS Bulletin* 33: 1006-1014.

Ramesh, R., and N. A. Spaldin. 2007. Multiferroics: progress and prospects in thin films. *Nature Mater.* 6: 21–29.

Saarinen, K., P. Hautojarvi, and C. Corbel. 1998. Positron annihilation spectroscopy of defects in semiconductors. In *Semiconductors and Semimetals* Vol. 51A, ed. M. Stavola, pp. 209‑285. San Diego, CA: Academic Press.

Sakuma, T., S. Yamamichi, S. Matsubara, H. Yamaguchi, and Y. Miyasaka. 1990. Barrier layers for realization of high capacitance density in $SrTiO_3$ thin-film capacitor on silicon. *Appl. Phys. Lett.* 57: 2431 (3 pages).

Schirmer, O. F. 1968. The structure of the paramagnetic lithium center in zinc oxide and beryllium oxide. *J. Phys. Chem. Solids* 29: 1407 – 1429.

Schooley, J F, W R Hosler, and Marvin L Cohen. 1964. Superconductivity in semiconducting $SrTiO_3$. *Phys. Rev. Lett.* 12: 474-475.

Schultz, P. J. and K. G. Lynn. 1988. Interaction of positron beams with surfaces, thin films, and interfaces. *Rev. Mod. Phys.* 60: 70 – 781.

Selim, F. A., M. H. Weber, D. Solodovnikov, and K. G. Lynn. 2007. Nature of native defects in ZnO. *Phys. Rev. Lett.* 99: 085502 (4 pages).

Sharma, P., A. Gupta, K. V. Rao, F. J. Owens, R. Sharma, R. Ahuja, J. M. Osorio Guillen, B. Johansson, and G. A. Gehring. 2003. Ferromagnetism above room temperature in bulk and transparent thin films of Mn-doped ZnO. *Nature Mater.* 2: 673 – 677.

Shi, G. A., M. Saboktakin, M. Stavola, and S. J. Pearton. 2004. “Hidden hydrogen” in as-grown ZnO. *Appl. Phys. Lett.* 85: 5601 (3 pages).

Shin, C., H. Yoo, and C. Lee. 2007. Al-doped $SrTiO_3$: Part I, anomalous oxygen nonstoichiometry. *Solid State Ionics* 178: 1081 – 1087.

Shockley, W., and G.L. Pearson. 1948. Modulation of conductance of thin films of semi-conductors by surface charges. *Phys. Rev.* 74: 232 – 233.

Siemons, W., G. Koster, H. Yamamoto, W. A. Harrison, G. Lucovsky, T. H. Geballe, D. H. A. Blank, and M. R. Beasley. 2007. Origin of charge density at $LaAlO_3$ on $SrTiO_3$ heterointerfaces: Possibility of intrinsic doping. *Phys. Rev. Lett.* 98: 196802 (4 pages).

Singh, A. K., A. Janotti, M. Scheffler, and C. G. Van de Walle. 2008. Sources of Electrical Conductivity in SnO_2. *Phys. Rev. Lett.* 101: 055502 (4 pages).

Son, J., P. Moetakef, B. Jalan, O. Bierwagen, N. J. Wright, R. Engel-Herbert, and S. Stemmer. 2010. Epitaxial $SrTiO_3$ films with electron mobilities exceeding 30,000 $cm^2 V^{-1} s^{-1}$. *Nature Mater.* 9: 482-484.

Spaldin, N. A., and M. Fiebig. 2005. The renaissance of magnetoelectric multiferroics. *Science* 309: 391 – 392.

Spinelli, A., M. A. Torija, C. Liu, C. Jan, and C. Leighton. 2010. Electronic transport in doped $SrTiO_3$: Conduction mechanisms and potential applications. *Phys. Rev. B* 81: 155110 (14 pages).

Solymar, L., and D. Walsh. 2004. *Electrical Properties of Materials*, 7th ed. New York: Oxford University Press Inc.

Takahashi, N., K. Kaiya, T. Nakamura, Y. Momose, and H. Yamamoto. 1999. Growth of ZnO on sapphire (0001) by vapor phase epitaxy using a chloride source. *Jpn. J. Appl. Phys.* 38: L454 – L456.

Teke, A., Ü. Özgür, S. Doğan, X. Gu, H. Morkoç, B. Nemeth, J. Nause, and H. O. Everitt. 2004. Excitonic fine structure and recombination dynamics in single-crystalline ZnO. *Phys. Rev. B* 70: 195207 (10 pages).

Thomas, D. G. 1957. Interstitial zinc in zinc oxide. J. *Phys. Chem. Solids* 3: 229-237.

Thomas, D.G., and J.J. Lander. 1956. Hydrogen as a donor in zinc oxide. *J. Chem. Phys.* 25: 1136 – 1142.

Thonke, K., M. Schirra, R. Schneider, A. Reiser, G. M. Prinz, M. Feneberg, J. Biskupek, U. Kaiser, and R. Sauer. 2009. The role of stacking faults and their associated 0.13 eV acceptor state in doped and undoped ZnO layers and nanostructures. *Microelectron. J.* 40: 210 – 214.

Thonke, K., T. Gruber, N. Teofilov, R. Schnfelder, A. Waag, and R. Sauer. 2001. Donor-acceptor pair transitions in ZnO substrate material. *Physica B* 308–310: 945 – 948.

Tufte, O.N., and P.W. Chapman. 1967. Electron mobility in semiconducting strontium titanate. *Phys. Rev*. 155: 796-802.

Valentini, A., F. Quaranta, M. Rossi, and G. Battaglin. 1991. Preparation and characterization of Li-doped ZnO films. *J. Vac. Sci. Technol. A* 9: 286 (4 pages).

van Benthem, K., C. Elsässer, and R. H. French. 2001. Bulk electronic structure of $SrTiO_3$: Experiment and theory. *J. Appl. Phys.* 90: 6156 – 6164.

Van de Walle, C. G. 2000. Hydrogen as a cause of doping in zinc oxide. *Phys. Rev. Lett.* 85: 1012 – 1015.

Van de Walle, C. G., and J. Neugebauer. 2003. Universal alignment of hydrogen levels in semiconductors, insulators and solutions. *Nature* 423: 626 – 628.

Van de Walle, C. G., D. B. Laks, G. F. Neumark, and S. T. Pantelides. 1993. First-principles calculations of solubilities and doping limits: Li, Na, and N in ZnSe. *Phys. Rev. B* 47: 9425 – 9434.

Van de Walle, C. G. 2001. Defect analysis and engineering in ZnO. *Physica B* 308–310: 899–903.

van der Pauw, L.J. 1958. A method of measuring the resistivity and Hall coefficient on lamellae of arbitrary shape. *Philips Tech. Rev.* 20: 220 – 224.

Vetterhöffer, J., and J. Weber. 1996. Hydrogen passivation of shallow donors S, Se, and Te in GaAs. *Phys. Rev. B* 53:12835–12844.

Villamagua, L., R. Barreto, L. Prócel and A. Stashans. 2007. Hydrogen impurity in $SrTiO_3$: Structure, electronic properties and migration. *Physica Scripta* 75: 374-378.

Vispute, R. D., V. Talyansky, S. Choopun, R. P. Sharma, T. Venkatesan, M. He, X. Tang, J. B. Halpern, M. G. Spencer, Y. X. Li, L. G. Salamanca-Riba, A. A. Iliadis, and K. A. Jones

1998. Heteroepitaxy of ZnO on GaN and its implications for fabrication of hybrid optoelectronic devices. *Appl. Phys. Lett.* 73: 348 – 350.

Wakim, F. 1968. Hydrogen and deuterium in $SrTiO_3$ single crystals. *J. Chem. Phys.* 49: 3738 – 3739.

Wang, C., Z. G. Ji, K. Liu, Y. Xiang, and Z. Z. Ye. 2003. *p*-Type ZnO thin films prepared by oxidation of Zn_3N_2 thin films deposited by DC magnetron sputtering. *J. Cryst. Growth* 259: 279 – 281.

Wang, J. Z., G. T. Du, B. J. Zhao, X. T. Yang, Y. T. Zhang, Y. Ma, D. L. Liu, Y. C. Chang, H. S. Wang, H. J. Yang, and S. R. Yang. 2003. Epitaxial growth of NH_3-doped ZnO thin films on $< 02\bar{2}4 >$ oriented sapphire substrates. *J. Cryst. Growth* 255: 293- 297.

Wang, K. F., J.-M. Liu, and Z. F. Ren. 2009. Multiferroicity: the coupling between magnetic and polarization orders. *Adv. Phys.* 58: 321 – 448.

Wang, L., and N.C. Giles. 2004. Determination of the ionization energy of nitrogen acceptors in zinc oxide using photoluminescence spectroscopy. *Appl. Phys. Lett.* 84: 3049 – 3051.

Wardle, M. G., J. P. Goss, and P. R. Briddon. 2005. Theory of Fe, Co, Ni, Cu, and their complexes with hydrogen in ZnO. *Phys. Rev. B* 72: 155108 (13 pages).

Wardle, M. G., J. P. Goss, and P. R. Briddon. 2005. Theory of Li in ZnO: A limitation for Li-based *p*-type doping. *Phys. Rev. B* 71: 155205 (10 pages).

Weber, G., S. Kapphan, and M. Wöhlecke. 1986. Spectroscopy of the O-H and O-D stretching vibrations in $SrTiO_3$ under applied electric field and uniaxial stress. *Phys. Rev. B* 34: 8406-8417.

Weber, M., N. Parmar, K. Jones, and K. Lynn. 2010. Oxygen deficiency and hydrogen turn ZnO red. *J. Electron. Mater.* 39: 573–576.

Wöhlecke, M., and L. Kovács. OH^- ions in oxide crystals. 2001. *Crit. Rev. Solid State Mater. Sci.* 26: 1 – 86.

Wu, X. D., D. Dijkkamp, S. B. Ogale, A. Inam, E. W. Chase, C. C. Chang, J. M. Tarascon, and T. Venkatesan. 1987. Epitaxial ordering of oxide superconductor thin films on (100) $SrTiO_3$ prepared by pulsed laser evaporation. *Appl. Phys. Lett.* 51: 861 – 863.

Yan, Y. F., S. B. Zhang, and S. T. Pantelides. 2001. Control of doping by impurity chemical potentials: Predictions for *p*-type ZnO. *Phys. Rev. Lett.* 86: 5723 – 5726.

Yao, B., D. Z. Shen, Z. Z. Zhang, X. H. Wang, Z. P. Wei, B. H. Li, Y. M. Lv, X. W. Fan, L. X. Guan, G. Z. Xing, C. X. Cong, and Y. P. Xie. 2006. Effects of nitrogen doping and illumination on lattice constants and conductivity behavior of zinc oxide grown by magnetron sputtering. *J. Appl. Phys.* 99: 123510 (5 pages).

Yu, T., Y. Chen, Z. Liu, N. Ming, and X. Wu. Epitaxial growth of dielectric $SrTiO_3$ thin films by pulsed laser deposition. 1999. *Appl. Surf. Sci.* 138–139: 605 – 608.

Zeuner, A., H. Alves, D.M. Hoffman, B.K. Meyer, A. Hoffmann, U. Haboeck, M. Strassburg and M. Dworzak. 2002. Optical properties of the nitrogen acceptor in epitaxial ZnO. *Phys. Stat. Sol. (b)* 234: R7 – R9.

Zhao, K., K. J. Jin, Y. H. Huang, S. Q. Zhao, H. B. Hui, M. He, Z. H. Chen, Y. L. Zhou, and G. Z. Yang. 2006. Ultraviolet fast-response photoelectric effect in tilted orientation $SrTiO_3$ single crystals. *Appl. Phys. Lett.* 89: 173507 (3 pages).

Zwingel, D., and F. Gärtner. 1974. Paramagnetic and optical properties of Na-doped ZnO single crystals. *Solid State Commun.* 14: 45 – 49.